

Carlos Eduardo Silva de Souza

**MODELING AND ANALYSIS OF TWO
ALTERNATIVES FOR UNDERWAY SHIP-TO-
SHIP TRANSFER OF OIL IN OPEN SEA**

São Paulo – 2012

Carlos Eduardo Silva de Souza

**MODELING AND ANALYSIS OF TWO
ALTERNATIVES FOR UNDERWAY SHIP-TO-
SHIP TRANSFER OF OIL IN OPEN SEA**

Dissertation presented to Escola
Politécnica da Universidade de São Paulo
for achievement of the degree of Master of
Science in Engineering.

Area of concentration: Naval Architecture
and Ocean Engineering

Supervisor: Prof. Dr. Helio Mitio
Morishita

São Paulo – 2012

**This work is dedicated *in memoriam*
to my grandfather, vô Zé.**

ACKNOWLEDGEMENTS

I am sincerely grateful to my supervisor, Prof. Dr. Helio Mitio Morishita, for the long discussions throughout my Master's and the opportunity of working in his research group since the 3rd year of my Bachelor's course.

Also fundamental for the development of this work were the support of Prof. Dr. Alexandre Nicolaos Simos and Prof. Dr. Eduardo Aoun Tannuri, who provided me valuable light in specific topics of my research.

Other specialists outside USP are acknowledged for have kindly shared their experience on different topics of this work. They are Prof. Dr. Alexandros Glykas (NTUA, Greece), Prof. Dr. Hiroyuki Oda (TUMSAT, Japan), Prof. Dr. Thor Fossen and Dr. Xu Xiang (NTNU, Norway) and Prof. Dr. Tristan Perez (Univ. of Newcastle, Australia).

My routine in the university allowed me to grow friendships that by no means could be disregarded in this space. Thank you Anderson, João, Kevin, Massa, Montanha, Sophie and Yuba for the fellowship and moments of amusement.

Besides, I could never fail to express how privileged I have been along this journey to have people like Caio, 16, Eduardo, Itajubá, Larissa, Lázaro, Lu, Luís, Natália, Pará, Rafael and Rubens as friends. Thank you, guys, for the stimulus, the companionship, the comfort, the discussions, the jazz, the chess, the tapiocas, the soccer and the beers.

Two people deserve my highest considerations, for they certainly are the most responsible for the accomplishment of this work. I fondly thank my parents, Elisa and Gilson, for so many years of patience, support and renunciations in behalf of my education and growing. I also thank to my sister, Lívia, for teaching me that life is not to be taken seriously. And to the rest of my (big) family, specially my grandparents, for the indispensable incentives along all of my life.

And thank you, God, for having blessed me with this family and for giving me strength to face my daily challenges.

Finally, I would like to manifest genuine gratitude to Transpetro, for supporting this research. And to CAPES, for the granted scholarship.

ABSTRACT

Shuttle tankers with dynamic positioning (DP) systems are expensive ships. Therefore, it is desirable to optimize their usage by, e.g., eliminating the travels between offshore platforms and the terminals in the coast. When the oil is intended to exportation, an attractive idea is to transfer it between the shuttle tanker and the exporter ship (usually a VLCC) in open sea, close to the oil fields. However, since a VLCC is rarely provided with a DP system, it is necessary to develop alternative ways of attaining controllability of both vessels while the transfer operation is performed. In this sense, two configurations for the so-called ship-to-ship operations are proposed. One of them consists in performing the transfer with underway ships, arranged side-by-side. The vessels are moored together and the VLCC develops power ahead, towing the idle shuttle tanker. Another alternative is to transfer the oil while the ships maintain a convoy formation, with the VLCC trailing a given trajectory and being followed by the shuttle tanker, which keeps a constant relative position by means of an appropriate autopilot strategy. Dynamic models are developed for both operations and implemented in numerical simulators. The simulations results are discussed and used to outline the operational viability under different combinations of environment and loading conditions.

TABLE OF CONTENTS

LIST OF FIGURES

LIST OF TABLES

LIST OF SYMBOLS

1. INTRODUCTION	22
1.1 OPERATIONS DESCRIPTION.....	25
1.1.1 Side-by-side.....	25
1.1.2 Convoy.....	27
1.2 LITERATURE REVIEW	28
1.3 OBJECTIVES	31
1.4 TEXT ORGANIZATION	33
2. DYNAMIC MODELING	34
2.1 NOTATION.....	34
2.2 COORDINATE SYSTEMS	36
2.3 KINEMATIC TRANSFORMATIONS	37
2.3.1 Rotation matrices.....	37
2.3.2 Transformation from <i>b</i> -frame to <i>h</i> -frame	39
2.3.3 Transformation from <i>b</i> -frame to <i>n</i> -frame.....	43
2.4 SHIP DYNAMICS	43
2.4.1 Inertia matrix.....	43
2.4.2 Rigid-body dynamics	44
2.5 HYDRODYNAMICS AND HYDROSTATICS	46
2.5.1 Radiation-induced components	47
2.5.2 Viscous components	49
2.5.3 Hydrostatic restoration.....	50
2.6 ENVIRONMENT MODELS.....	50
2.6.1 Waves	51

2.6.2	Wind.....	56
2.6.3	Current.....	58
2.7	THE EQUATIONS OF MOTIONS.....	59
2.7.1	Maneuvering.....	60
2.7.2	Seakeeping.....	62
2.7.3	Unified model for maneuvering and seakeeping.....	63
3.	CONTROL.....	69
3.1	CONTROL APPROACHES.....	69
3.1.1	PID controller.....	70
3.1.2	Backstepping controller.....	71
3.2	NONLINEAR PASSIVE OBSERVER.....	74
3.2.1	Observer model.....	75
3.2.2	Observer design.....	77
3.2.3	Gains determination.....	77
3.3	THE LINE-OF-SIGHT GUIDANCE SYSTEM.....	79
4.	UNDERWAY SIDE-BY-SIDE OPERATION.....	81
4.1	HYDRODYNAMIC INTERACTIONS.....	84
4.1.1	Suction loads.....	84
4.1.2	Wave interaction.....	85
4.2	HYDRODYNAMIC CALCULATIONS.....	86
4.2.1	Calculation of modal periods.....	86
4.2.2	The lid method.....	88
4.2.3	Loading conditions.....	89
4.3	DYNAMICS.....	90
4.3.1	Equations of motions.....	90
4.3.2	Hydrodynamic suction loads.....	91
4.3.3	Fenders loads.....	92

4.3.4	Mooring loads	94
4.3.5	Environmental loads.....	96
5.	CONVOY OPERATION	98
5.1	DYNAMICS.....	99
5.2	CONTROL.....	100
5.2.1	References generator (shuttle tanker).....	100
5.2.2	Controllers.....	101
5.3	ACTUATORS DYNAMICS.....	105
6.	SIMULATIONS AND RESULTS	107
6.1	SIDE-BY-SIDE.....	109
6.1.1	Fenders properties	109
6.1.2	Mooring system.....	109
6.1.3	Hydrodynamic data	110
6.1.4	Environmental action	117
6.1.5	Simulations results	118
6.2	CONVOY	126
6.2.1	Shuttle tanker actuators properties.....	127
6.2.2	Environmental action	129
6.2.3	Simulations results	129
7.	CONCLUSIONS	138
7.1	SIDE-BY-SIDE.....	138
7.2	CONVOY	139
7.3	FINAL CONSIDERATIONS AND RECOMMENDATIONS FOR FUTURE WORK.....	140
	REFERENCES	142
	APPENDIX A – The Lyapunov Direct Method	149
A.1	DEFINITION OF STABILITY ACCORDING TO LYAPUNOV	149
A.2	LYAPUNOV'S DIRECT METHOD	149

LIST OF FIGURES

Figure 1.1 - Offloading operation with a DP-shuttle tanker.	23
Figure 1.2 - Side-by-side operation.....	24
Figure 1.3 - Side-by-side operation scheme.....	26
Figure 1.4 – Underway replenishment operation.....	26
Figure 1.5 – Convoy operation scheme.....	27
Figure 2.1 – Coordinate systems.....	37
Figure 2.2 – Added mass (surge) for a tanker versus frequency of encounter. ..	48
Figure 2.3 – Comparison between JONSWAP and Pierson-Moskowitz spectra.	53
Figure 2.4 – RAOs for sway (left) and yaw (right) motions for a pipelaying barge and for a 100% loaded VLCC	53
Figure 2.5 – Illustration of the process of transforming wave elevation in ship motions.....	54
Figure 2.6 – Wind coefficients (surge) versus incidence direction.....	57
Figure 2.7 – Wind coefficients (sway) versus incidence direction.....	58
Figure 2.8 – Wind coefficients (yaw) versus incidence direction.	58
Figure 2.9 – Usual approach of superposing LF and WF motions	64
Figure 2.10 – Unified model for maneuvering and seakeeping	68
Figure 3.1 – PID controller structure.....	70
Figure 3.2 – Integrator windup phenomenon, where y is the process output, y_{sd} is the setpoint, u is the control signal and I is the integral part. Extracted from	71
Figure 3.3 – Line-of-sight procedure for calculation of ψ_{ref}	80
Figure 4.1 – Side-by-side operation.....	81
Figure 4.2 – Maneuvering and berthing.....	82
Figure 4.3 - Typical mooring scheme.....	83
Figure 4.4 – Wave field between two approaching ships.....	85
Figure 4.5 – Ships advancing in waves.....	87
Figure 4.6 – A lid (red) is placed between hulls for attenuation of the free- surface elevation.....	89
Figure 4.7 – Fenders avoid steel-steel contact between ships hulls.....	92
Figure 4.8 – Fender model.....	93

Figure 4.9 – Fenders reaction forces X deflection percentage (top) and displacement (bottom).....	94
Figure 5.1 - Convoy operation.....	98
Figure 6.1 – Mooring scheme.....	111
Figure 6.2 – Damped free surface elevation – for a unitary incident wave amplitude – for loading condition 1. The x-axis corresponds to points distributed along the lid length, with 0 and 38 corresponding to the aft- and fore-most extremities, respectively.	112
Figure 6.3 – Parametric approximation for the retardation function (VLCC – surge-surge).	114
Figure 6.4 – Connection between the equations of motions and the state-space system for approximation of the memory functions vector μ	114
Figure 6.5 – Sway-sway hydrodynamic coefficients referent to the VLCC (A11, B11), to the coupled effects on the VLCC due to the shuttle tanker motions (A12, B12), to the coupled effects on the shuttle tanker due to the VLCC motions (A21, B21) and to the shuttle tanker (A22, B22).....	116
Figure 6.6 – Sway-sway added masses calculated for both isolated and interacting ships.....	116
Figure 6.7 – XY positions for side-by-side operation under loading condition 1, $H_s = 3.5$ m, $T_p = 15.0$ s, wave incidence of 195° and mooring arrangement 8-4-6.....	118
Figure 6.8 – Fender loads for side-by-side operation under loading condition 1, $H_s = 3.5$ m, $T_p = 15.0$ s, wave incidence of 195° and mooring arrangement 8-4-6.....	119
Figure 6.9 – Traction in mooring lines for side-by-side operation under loading condition 1, $H_s = 3.5$ m, $T_p = 15.0$ s, wave incidence of 195° and mooring arrangement 8-4-6.....	120
Figure 6.10 – Roll, pitch and yaw motions for side-by-side operation under loading condition 1, $H_s = 3.5$ m, $T_p = 15.0$ s, wave incidence of 195° and mooring arrangement 8-4-6.	120
Figure 6.11 – Mooring system conditions for side-by-side operation under loading condition 1, wave incidence of 195° and mooring arrangement 8-4-6.....	121

Figure 6.12 – Mooring system conditions for side-by-side operation under loading condition 1, wave incidence of 315° and mooring arrangement 8-4-6.....	122
Figure 6.13 – Mooring system conditions for side-by-side operation under loading condition 1, wave incidence of 195° and mooring arrangement 8-4-4.....	122
Figure 6.14 – Mooring system conditions for side-by-side operation under loading condition 1, wave incidence of 315° and mooring arrangement 8-4-4.....	122
Figure 6.15 – Roll, pitch and yaw motions for side-by-side operation under loading condition 1, Hs = 3.5 m, Tp = 15.0s, wave incidence of 195° and mooring arrangement 8-4-4.....	123
Figure 6.16 – Mooring system conditions for side-by-side operation under loading condition 1, wave incidence of 195° and mooring arrangement 6-4-4.....	123
Figure 6.17 – Mooring system conditions for side-by-side operation under loading condition 1, wave incidence of 315° and mooring arrangement 6-4-4.....	123
Figure 6.18 – Mooring system conditions for side-by-side operation under loading condition 2, wave incidence of 195° and mooring arrangement 8-4-6.....	123
Figure 6.19 – Mooring system conditions for side-by-side operation under loading condition 2, wave incidence of 315° and mooring arrangement 8-4-6.....	124
Figure 6.20 – Mooring system conditions for side-by-side operation under loading condition 2, wave incidence of 195° and mooring arrangement 8-4-4.....	124
Figure 6.21 – Mooring system conditions for side-by-side operation under loading condition 2, wave incidence of 315° and mooring arrangement 8-4-4.....	124
Figure 6.22 – Mooring system conditions for side-by-side operation under loading condition 2, wave incidence of 195° and mooring arrangement 6-4-4.....	124

Figure 6.23 – Mooring system conditions for side-by-side operation under loading condition 2, wave incidence of 195° and mooring arrangement 6-4-4.	125
Figure 6.24 – Mooring system conditions for side-by-side operation under loading condition 3, wave incidence of 195° and mooring arrangement 8-4-6.	125
Figure 6.25 – Mooring system for side-by-side operation under loading condition 3, wave incidence of 315° and mooring arrangement 8-4-6.	125
Figure 6.26 – Mooring system conditions for side-by-side operation under loading condition 3, wave incidence of 195° and mooring arrangement 8-4-4.	125
Figure 6.27 – Mooring system conditions for side-by-side operation under loading condition 3, wave incidence of 315° and mooring arrangement 8-4-4.	126
Figure 6.28 – Mooring system conditions for side-by-side operation under loading condition 3, wave incidence of 195° and mooring arrangement 6-4-4.	126
Figure 6.29 – Mooring system conditions for side-by-side operation under loading condition 3, wave incidence of 195° and mooring arrangement 6-4-4.	126
Figure 6.30 – Rudder lift coefficient for the shuttle tanker.	128
Figure 6.31 – Distance between manifolds Dmf	130
Figure 6.32 – XY positions for convoy operation under loading condition 1, $H_s = 1.5\text{m}$, $T_p = 8.0\text{s}$, wave incidence 195° and no wind loads.	131
Figure 6.33 – Distance between manifolds for convoy operation under loading condition 1, $H_s = 1.5\text{m}$, $T_p = 8.0\text{s}$, wave incidence 195° and no wind loads.	131
Figure 6.34 – Low-frequency estimates for convoy operation under loading condition 1, $H_s = 1.5\text{m}$, $T_p = 8.0\text{s}$, wave incidence 195° and no wind loads.	132
Figure 6.35 - Rudder commanded and effective deflection for convoy operation under loading condition 1, $H_s = 1.5\text{m}$, $T_p = 8.0\text{s}$, wave incidence 195° and no wind loads.	132

Figure 6.36 – Results for convoy operation under loading condition 1, wave incidence of 120° and in presence of wind.	133
Figure 6.37 – Results for convoy operation under loading condition 1, wave incidence of 120° and in absence of wind.	133
Figure 6. 38 – Results for convoy operation under loading condition 1, wave incidence of 195° and in presence of wind.	134
Figure 6.39 – Results for convoy operation under loading condition 1, wave incidence of 195° and in absence of wind.....	134
Figure 6.40 – Results for convoy operation under loading condition 2, wave incidence of 120° and in presence of wind.	134
Figure 6.41 – Results for convoy operation under loading condition 2, wave incidence of 120° and in absence of wind.	135
Figure 6.42 – Results for convoy operation under loading condition 2, wave incidence of 195° and in presence of wind.	135
Figure 6.43 – Results for convoy operation under loading condition 2, wave incidence of 195° and in absence of wind.....	135
Figure 6.44 – Results for convoy operation under loading condition 3, wave incidence of 120° and in presence of wind.	136
Figure 6.45 – Results for convoy operation under loading condition 3, wave incidence of 120° and in absence of wind.	136
Figure 6.46 – Results for convoy operation under loading condition 3, wave incidence of 195° and in presence of wind.	136
Figure 6.47 – Results for convoy operation under loading condition 3, wave incidence of 195° and in absence of wind.....	136
Figure 6.48 – Results for convoy operation under loading condition 4, wave incidence of 120° and in presence of wind.	137
Figure 6.49 – Results for convoy operation under loading condition 4, wave incidence of 120° and in absence of wind.	137
Figure 6.50 – Results for convoy operation under loading condition 4, wave incidence of 195° and in presence of wind.	137
Figure 6.51 – Results for convoy operation under loading condition 4, wave incidence of 195° and in absence of wind.....	137

LIST OF TABLES

Table 2.1 – Notation for generalized positions, velocities and forces.	35
Table 6.1 – VLCC main dimensions.	107
Table 6.2 – Shuttle tanker main dimensions.....	108
Table 6.3 –Compression X induced force relation for fenders.	110
Table 6.4 – Mooring lines properties.	111
Table 6.6 – Main properties of the shuttle tanker rudder.....	127
Table 6.7 – Waves parameters for the convoy simulations.....	129

LIST OF SYMBOLS

Vectors and matrices are written in **bold** characters, while scalars are generally in *italic*. When the same symbol is assigned to two or more distinct meanings, a subscript is placed in at least one of them for sake of distinction. Following, the most relevant adopted in this symbols are presented as to ease consultation throughout the text reading.

Roman alphabet

A	Added mass and inertia matrix
A (∞)	Asymptotic infinite-frequency added mass matrix
A ₀	Zero-frequency added mass matrix
<i>A</i> _L	Lateral ship projected area above water surface
<i>A</i> _r	Rudder area
<i>A</i> _T	Transverse ship projected area above water surface
A _r	State matrix for the memory effects state-space approximation
<i>A</i> _{wp}	Water plane area
b	Bias forces and moments vector
B	Potential damping matrix
B _r	Input matrix for the memory effects state-space approximation
<i>B</i> _s	Ship beam
C _A	Added mass Coriolis and centripetal matrix
<i>C</i> _B	Block coefficient
<i>C</i> _{h,i}	Coefficient for calculation of hydrodynamic suction loads ($i = X, Y, N$)
<i>C</i> _{i,curr}	Coefficient for calculation of current loads ($i = X, Y, N$)
<i>C</i> _{i,wind}	Coefficient for calculation of wind loads ($i = X, Y, N$)
<i>C</i> _L	Rudder lift coefficient
<i>c</i> _m	Rudder mean chord
C _r	Output matrix for the memory effects state-space approximation
C _{RB}	Rigid-body Coriolis and centripetal matrix

d	Vector of damping loads
d_L	Longitudinal distance assigned for the convoy operation
d_T	Transversal distance assigned for the convoy operation
D_i	Drift coefficient ($i = 1,2,6$)
D_{mf}	Distance between manifolds
D_p	Propeller diameter
D_{rope}	Mooring rope diameter
D_s	Ship depth
$D_{wdd,i}$	Wave drift damping coefficient ($i = 1,2,6$)
D	Damping matrix
D_r	Feedthrough matrix for the memory effects state-space approximation
f	Ship freeboard
F_i^{MD}	Waves mean drift forces ($i = 1,2,6$)
F_n	Froud number
g	Acceleration of gravity
g	Vector of restoration loads
G	Restoration matrix
\overline{GM}_L	Longitudinal metacentric height
\overline{GM}_T	Transversal metacentric height
G_{PID}	PID controller transfer function
h_r	Rudder height
H_s	Significant wave height
I_i	Ship moment of inertia relative to i -axis ($i = x, y, z$)
I_{ij}	Ship product of inertia ($i, j = x, y, z, i \neq j$)
J_bⁿ	Coordinates rotation matrix from body- to Earth-fixed systems
k	Wave number
K	Moment in roll direction
K	Matrix of retardation functions
K₁	Gain matrix for the observer wave-frequency model
K₂	Gain matrix for the observer kinematics model

K_{rope}	Mooring rope stiffness
l_h	Hose length
l_δ	Moment arm from the ship center of gravity to the rudder center of pressure
L_{oa}	Length overall
L_{pp}	Length between perpendiculars
L_{rope}	Mooring rope length
m	Ship mass
M	Moment on pitch direction
\mathbf{M}	Inertia matrix
\mathbf{M}_{RB}	Rigid-body inertia matrix
N	Moment on yaw direction
N_{curr}	Current moment in yaw
N_{wind}	Wind moment in yaw
o_b	Origin of the body-fixed coordinate system
o_n	Origin of the Earth-fixed coordinate system
o_s	Origin of the seakeeping coordinate system
p	Angular velocity in roll
p_{los}	Line-of-sight position
q	Angular velocity in pitch
r	Angular velocity in yaw
\mathbf{R}_a^b	Matrix for rotation of a vector in frame a to a frame b
R_e	Reynolds number
S_s	Ship wetted hull area
S_w	Wave spectrum
\mathbf{T}	Matrix with time constants for the bias model
\mathbf{T}_a	Euler angles attitude matrix
T_{max}	Main propeller maximum thrust
T_{min}	Main propeller minimum thrust
T_p	Wave peak period
T_{rope}	Mooring rope traction
T_s	Ship draft
u	Linear velocity in surge

u_{ref}	Surge velocity reference
U_{curr}	Current speed
U_s	Service speed
U_{wind}	Wind speed
v	Linear velocity in sway
w	Linear velocity in heave
\mathbf{w}	Vector of zero-mean gaussian white noise
x	Position in surge direction
y	Position in sway direction
z	Position in heave direction
X	Force in surge direction
X_{curr}	Current force in surge
X_i^{WF}	1 st –order wave load ($i = 1,2,6$)
X_{wind}	Wind force in surge
Y	Force in sway direction
y_{min}	Minimum safe separation distance assigned for the convoy operation
y_{sep}	Separation distance assigned for the convoy operation
Y_{curr}	Current force in sway
Y_{wind}	Wind force in sway
Z	Force in heave direction

Greek alphabet

α_r	Current relative incidence direction
β_r	Wave relative incidence direction
γ_r	Wind relative incidence direction
δ_r	Rudder deflection
Δ	Ship displacement
Γ	Output matrix for the observer wave-frequency model
ζ_i	Damping for the observer wave model ($i = 1,2,3$)
ζ_{ni}	Notch filter damping for the observer wave model ($i = 1,2,3$)

$\boldsymbol{\eta}$	Vector with 6 DOF coordinates in the Earth-fixed system
$\boldsymbol{\eta}_1$	Vector of positions in the Earth-fixed system
$\boldsymbol{\eta}_2$	Vector of Euler angles in the Earth-fixed system
$\boldsymbol{\eta}_h$	Vector with horizontal 3 DOF coordinates in the Earth-fixed system
$\boldsymbol{\eta}_{SBS}$	Coupled vector of coordinates for the side-by-side model
$\boldsymbol{\eta}_{wf}$	Vector of wave-frequency positions
θ	Euler angle respective to pitch
$\boldsymbol{\kappa}$	Gain matrix for the observer low-frequency model
λ_e	Wave-length of encounter
λ_{proj}	Projection of the wave-length in the ship advance direction
$\boldsymbol{\Lambda}$	Gain matrix for the observer bias model
Λ_g	Rudder effective aspect ratio
$\boldsymbol{\mu}$	Vector of memory effects
\boldsymbol{v}	Vector with 6 DOF velocities in the body-fixed system
\boldsymbol{v}_1	Vector of linear velocities in the body-fixed system
\boldsymbol{v}_2	Vector of angular velocities in the body-fixed system
\boldsymbol{v}_h	Vector with horizontal 3 DOF velocities in the body-fixed system
\boldsymbol{v}_{SBS}	Coupled vector of velocities for the side-by-side model
$\boldsymbol{\xi}$	Vector with 6 DOF coordinates in the seakeeping system
ξ_i	Coordinate in i -direction ($i = 1, \dots, 6$) of the seakeeping system
ρ_{Air}	Density of air
ρ_w	Density of water
σ_i	Parameter for adjustment of the observer wave model ($i = 1, 2, 3$)
σ_{rope}	Mooring rope tension
$\boldsymbol{\Sigma}$	Input matrix for the observer wave-frequency model
$\boldsymbol{\tau}$	Vector with 6 DOF loads in the body-fixed system
$\boldsymbol{\tau}_1$	Vector of forces in the body-fixed system
$\boldsymbol{\tau}_2$	Vector of moments in the body-fixed system

τ_{ctr}	Vector of control loads
τ_{backs}	Vector of control loads determined by the backstepping controller
τ_{env}	Vector of environmental loads
τ_{fnd}	Vector of fender loads
τ_{hdl}	Vector of hydrodynamic suction loads
τ_{hyd}	Vector of hydrodynamic loads
τ_{mrn}	Vector of mooring system loads
τ^{PID}	PID controller load
τ_{WF}	Vector of first-order wave loads
ϕ	Euler angle respective to roll
χ	State vector for the memory effects approximation
ψ	Euler angle respective to yaw
ψ_{ref}	Heading reference
ω	Wave frequency
ω_{0i}	Modal frequency for the observer wave model ($i = 1,2,3$)
ω_{ci}	Cut frequency for the observer wave model ($i = 1,2,3$)
ω_e	Frequency of encounter
ω_p	Wave peak frequency
Ω	State matrix for the observer wave-frequency model

Other symbols and notation

∇	Ship volumetric displacement
\cdot	(over the symbol) Time derivation
T	(superscript) Transposed matrix
\wedge	(over the symbol) Estimated value
\sim	(over the symbol) Offset between real and desired values
$_$	(over the symbol) Offset between real and estimated values

Quem bater primeiro a dobra do mar

Dá de lá bandeira qualquer

Aponta pra fé e rema

“Dois Barcos”, Marcelo Camelo

1. INTRODUCTION

Oil production in Brazil is expected to increase considerably in the next decades. In a moment characterized by increase in consumption and depletion of many of the current proven reserves, exploration of the Pre-salt fields is supposed to put the country among prominent oil exporters. In fact, world oil demand is presumed to increase from 94 mb/d¹ in 2015 to 106 mb/d in 2030, while the output at the current producing fields is going to drop from 51 mb/d in 2015 to 27 mb/d in 2030 (IEA, 2008). Thus, production in new fields will be vital to supply world demand for energy in the next decades.

The important role Brazil is going to play in the oil industry makes it indispensable to start the development of solutions for a wide spectrum of challenges. Pre-salt oil fields lie at high depths and up to 300 km far from the coast. Thus, optimal usage of resources is imperative to ensure economic viability in the exploitation process. Advanced technology will be required in many operations, leading to high costs in virtually every stage of the production. In this sense, any solution that may lead to a more efficient utilization of the exploitation equipment, oil rigs and ships is very welcome.

The present work focuses on alternatives to improve the utilization of shuttle tankers. These ships, usually provided with *dynamic positioning systems*, are broadly used in offloading operations, which consist in the transfer of oil from a FPSO² to a tanker (Figure 1.1).

Dynamic positioning (DP) systems are intended to control a ship in surge, sway and yaw motions exclusively by means of thrusters (FOSSEN, 2002). They are important during an offloading operation in order to keep the shuttle tanker – subjected to environment action – with a safe position relative to the FPSO, avoiding incidents like shocks and hose disconnections. However, a DP system considerably increases the costs of a ship, such that a so-called *DP shuttle tanker* should be used in a very rational way in order to diminish the total expenses involved in the supply chain.

¹ Million barrels per day.

² Acronym for Floating, Production, Storage and Offloading unity. Roughly speaking, this is a kind of platform capable of both explore and keep oil until it is offloaded to the shuttle tanker.



Figure 1.1 - Offloading operation with a DP-shuttle tanker.

Once loaded, a shuttle tanker cruises to the coast, where it discharges the oil in an onshore terminal before travelling back to the production fields. This oil may be intended for either intern consumption or exportation. In the latter case, another tanker (normally a VLCC³) loads the oil in the shore-based terminal before following to its destination.

The cruise speed of a shuttle tanker is about 15 knots. Hence, a fast calculation results that it would take about 22 hours to course a round-trip between a FPSO and a shore-based terminal (admitting a distance of 300 km). Considering the time spent for approaching and berthing in the terminal, it is possible to consider that the ship wastes at least one day travelling for each offloading operation.

Other drawbacks are involved in the procedure described above. First, an increase in oil exportation would reflect in the number of VLCCs wasting time waiting to berth in Brazilian harbors, which is again undesirable under the economic aspect. Also, Pre-salt fields extend to 800 km of Brazil's coast (PETROBRAS, 2012), demanding a wise logistic solution to distribute shuttle tankers among the production sites. The necessary quantity of ships increases when they spend much time travelling to the coast instead of keeping close to the oil fields.

³ *Very Large Crude Carrier.*

A worthy alternative to overcome these disadvantages would be to avoid the time-consuming trips, by transferring the oil intended to exportation from the shuttle tanker directly to the VLCC. This could be performed around the exploration fields, so that at the end of the transfer process the shuttle tanker would already be close to the production units.

Obviously, the proposed solution is not free of caveats. In fact, as in any conventional offloading operation, it is imperative to assure a safe relative distance between ships, even under harsh environmental conditions. However, in general a VLCC is not provided with a station keeping system like dynamic positioning. Anchoring is also impracticable, considering that Pre-salt fields may lie at up to 2000 m water depth. The risks involved in the transfer of oil between two vessels in open sea make it indispensable to ensure controllability for both of them.

Course controllability may be attained if ships advance at moderate speed. This motivates the proposal of two different configurations for underway transfer of oil between two vessels in a seaway. One of them is the so-called *side-by-side* configuration, that is, ships navigate parallel while the oil is transferred from the shuttle tanker to the VLCC (Figure 1.2). The other one consists in a *convoy* formation, with the VLCC sailing ahead while the shuttle tanker follows behind during the transfer operation.



Figure 1.2 - Side-by-side operation.

Application of such alternatives for real oil transference procedures demands extensive previous analyses of operational viability and safety. When ships

operate at so short separation distances, the risks of an accident are critical and make imperative the verification of conditions (e.g. weather window) under which the operations are feasible. This can be done through analysis of numerical simulations outputs.

1.1 OPERATIONS DESCRIPTION

For ease of reference, the approached alternatives will be referred to as:

- Side-by-side
- Convoy

A description of some technical aspects and practicalities involved in these operations is given below.

1.1.1 Side-by-side

Side-by-side operations start with the VLCC following a straight trajectory while the shuttle tanker approaches from starboard. Fenders are then placed between ships to absorb shocks, and when the vessels are parallel and with manifolds aligned specialized personnel moor them together and handle the hose with the ships cranes. Separation distance is of the order of the fenders diameters, which for this case round 3 m. Then, the shuttle tanker powers its engine off and is towed by the VLCC. Figure 1.3 depicts a scheme for a side-by-side operation.

A similar operation is performed by worldwide navies. The so-called *underway replenishment* operations consist on the transfer of fuel, equipment or even personnel between two advancing ships (Figure 1.4). The differences are in the separation distances and advancing velocities, both higher than in side-by-side operations. Also, no towing takes place in this case.

The hydrodynamic interactions between both vessels are undoubtedly the largest matter in a side-by-side modeling. They arise from two main sources:

- the disturbed free-surface between ships, leading to significant wave forces acting in the hulls;
- the low pressure field between hulls, due to the increased fluid velocity in this region, leading to suction forces attracting the ships apart.

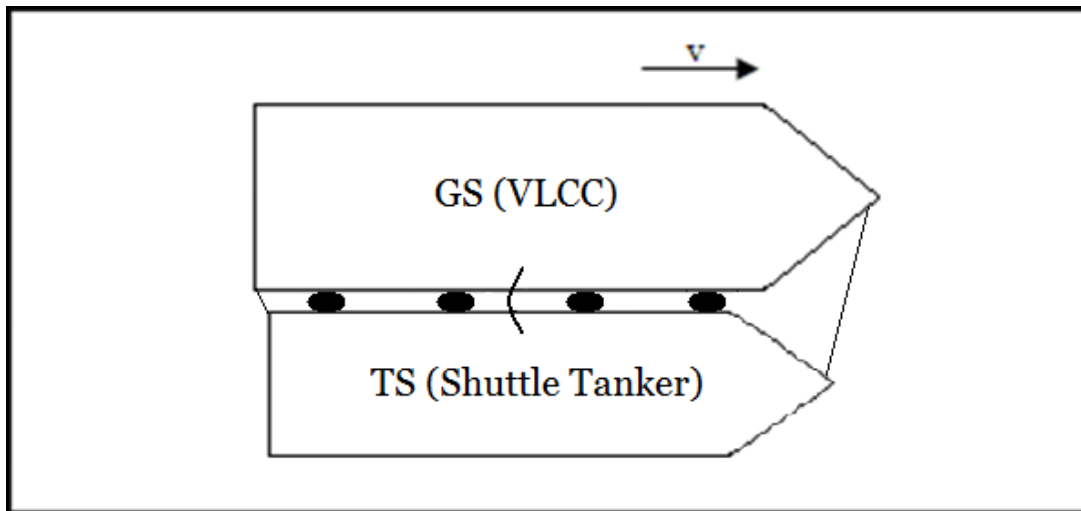


Figure 1.3 - Side-by-side operation scheme.



Figure 1.4 – Underway replenishment operation.

The presence of common forces induced by the mooring system demands the utilization of a unified approach for seakeeping and maneuvering. That is, both low-frequency and wave-frequency loads are considered in the same equations of motions. The operation is performed at a speed of approximately 5 knots. A key concern is the integrity of the mooring lines, which may be excessively loaded depending on the sea state. Therefore, simulations should focus on the analyses of these tensions in function of the environment harshness.

1.1.2 Convoy

An alternative for the side-by-side configuration is the convoy formation, which corresponds to the VLCC being followed by the shuttle tanker, as illustrated on Figure 1.5. Both ships must keep a given constant velocity and predefined relative longitudinal and transversal distances. It is admitted that no important hydrodynamic interactions take place in this alternative and, in contrast to the side-by-side operation, there is no transmission of wave frequency loads through mooring ropes. Hence, a conventional maneuvering model is enough to describe the system dynamics.

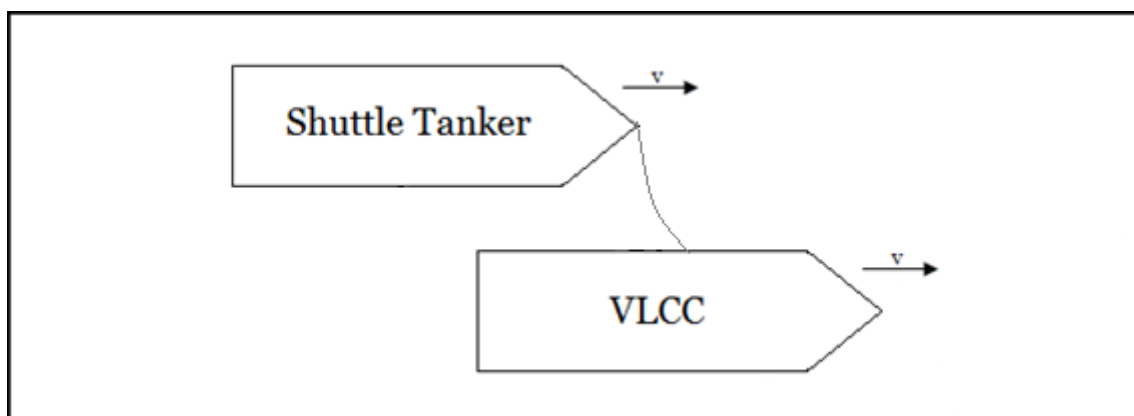


Figure 1.5 – Convoy operation scheme.

Control, on the other hand, is a very important element in this case. The VLCC is supposed to simply navigate with a given heading and constant velocity. Meanwhile, the shuttle tanker uses the VLCC position and instant speed to generate references in order to keep a constant relative position. This is critical to avoid hose disconnection or a collision between ships, so that the control system must be designed to respond fast for position disturbances. Once tunnel thrusters do not work properly when the ship navigates at moderate speed, a strategy for control of underactuated systems must be applied for the shuttle tanker autopilot.

In spite of being less likely to shocks than in the side-by-side configuration, convoy alternative has serious practical drawbacks. First, the tasks of hose connection and disconnection involve launching an extremity of such bulky and heavy structure between moving ships at a relatively far distance. Secondly, wise solutions must be developed in order to avoid hose dragging in water. However, this solution is attractive since it does not involve additional physical elements

for controllability – the only demand is the implementation of the proper control algorithm for the shuttle tanker autopilot system.

1.2 LITERATURE REVIEW

The deduction and understanding of the ship equations of motions demand a mature treatment of rigid-body dynamics. This is properly presented in (FOSSEN, 1994, 2002), where a vectorial approach is used to describe the ship kinematics and dynamics, leading to the equations of motion in 6 DOF. A rigorous kinematics treatment involving three coordinate frames is given in (PEREZ and FOSSEN, 2007). A basis on dynamics of linear systems is provided in (MEIROVITCH, 1970).

Another key topic for a proper comprehension of ship motions is hydrodynamics. A theoretical treatment devoted to marine systems is extensively covered in (NEWMAN, 1977), and (FALTINSEN, 1990) is a valuable reference on the effects of sea loads in floating structures.

The choice of proper environmental models is essential for ship dynamics modeling. A *quasi-explicit*⁴ heuristic model for estimating current loads on static ships is presented in (LEITE, ARANHA, *et al.*, 1998), and is extended in (SIMOS, TANNURI and ARANHA, 2001) to incorporate yaw damping terms. For both wind and current loads in tankers, (OCIMF, 1977) is considered to be a standard method due to its simplicity and coherent estimates. However, when two ships operate close from each other it is important to consider wind shadowing effects. Some investigations are available for the tandem configuration, like (BUCHNER and BUNNIK, 2002) and (TANNURI, FUCATU, *et al.*, 2010), but no works were found for the specific case of the side-by-side configuration.

Wave loads are calculated by means of coefficients and transfer functions provided by potential theory software based on the panels method, as explained on (WAMIT, 2006). A method for calculation of wave drift loads with influence of wave-current interaction is presented in (ARANHA, 1996), but this approach is not adequate for the case of two close ships advancing parallelly.

⁴ That is, dependent on the ship's main dimensions and only a few hydrodynamic coefficients.

Ship dynamics are usually divided in *maneuvering* and *seakeeping* theories. Both topics are overviewed on (PEREZ, FOSSEN and SØRENSEN, 2004) and more extensively on (LEWIS, 1998). Maneuvering is specifically considered in (SKJETNE, 2005) and (SKJETNE, SMOGELI and FOSSEN, 2004), where it is treated in a control-oriented point-of-view. Models based on hydrodynamic derivatives are widely used for maneuvering simulations. Descriptions of this approach are given in (NORRBIN, 1970), (INOUE, HIRANO and KIJIMA, 1981), (BERTRAM, 2000), (VAN BERLEKOM and GODDARD, 1972) and (PEREZ and BLANKE, 2008).

Some situations, however, demand the use a *unified model for both maneuvering and seakeeping* (BAILEY, PRICE and TEMAREL, 1997). This is the case when common forces are present in a multibody system, so that wave frequency loads are transmitted between ships. This leads to consideration of fluid memory effects on the equations of motions, represented by convolution integrals of *retardation functions* (CUMMINS, 1962), (OGILVIE, 1964). A formulation for the complete set of nonlinear equations of motions formulated for the unified model is presented in (FOSSEN, 2005).

At first sight, the unified model may be considered unviable for time-domain simulations due to the convolution integral to be evaluated at every time-step. This problem may be overcome by replacing the integral by a linear state-space model, with matrices determined by identification of a parametric representation of the convolution term (KRISTIANSEN and EGELAND, 2003), (HJUSTAD, KRISTIANSEN and EGELAND, 2004) and (KAASEN and MO, 2005). Several publications explain how to deal with this task in practice, (PEREZ and FOSSEN, 2009), (PEREZ and FOSSEN, 2009) and (TAGHIPUR, PEREZ and MOAN, 2008).

An alternative method for considering a unified model for maneuvering and seakeeping is the two-time scale model proposed in (SKEJIC, 2008) and (SKEJIC and FALTINSEN, 2008). This approach consists in considering the linear wave-induced motions to occur in a faster time-scale than the maneuvering dynamics, allowing the equations of motion for both seakeeping and maneuvering to be solved separately but without disregarding their interdependence.

A basis on linear control systems theory is provided in (DORF and BISHOP, 2001). It covers a wide range of subjects from frequency domain analysis to state-space systems, including classical control approaches and the most commonly used methods to determine stability. Nonlinear control is treated in a somewhat applied point of view in (MÁRQUEZ, 2003), while a deeper understanding on nonlinear systems theory for control purposes may be found in (KHALIL, 2001). (KRSTIC, KANELAKOPOULOS and KOKOTOVIC, 1995) presents the backstepping methodology for nonlinear control. (FOSSEN, 1994), (FOSSEN, 2002) and (SØRENSEN, 2005) are first references on application of control methods to marine systems. Application of nonlinear controllers to ships is covered in (FOSSEN and STRAND, 1998), and in (FOSSEN and STRAND, 1999) nonlinear observers design based on passivity theory is explored. A survey on industrial systems for guidance and control of ships is presented in (GOLDING, 2004).

Underway side-by-side operations are for some extent becoming popular in the oil industry. Safety procedures in such operations are provided in a guideline published by OCIMF⁵ (OCIMF, 2005). An overview of side-by-side operations is presented in (BERG and BAKKE, 2008), and a dynamic model is proposed in (SOUZA and MORISHITA, 2011). Criteria for fenders selection and mooring arrangements are described in (SAKAKIBARA and YAMADA, 2008). Obviously, the hydrodynamic interactions comprise a main source of worries for this configuration. The number of publications and conferences approaching this area is increasing, but there is still a lack of conclusive answers and methods concerning the phenomenon.

The behavior of the wave field between two ships in underway replenishment is modeled by means of potential theory in (CHEN and FANG, 2001). The influence of a ship motions due to the presence of a second one, also in underway replenishment, is investigated in (MCTAGGART, CUMMING, *et al.*, 2003). QUADVLIEG *et al.* (2011) describe the side-by-side case, where the very short clearance influences even more on the free-surface between ships than in the underway replenishment case.

⁵ Oil Companies International Marine Forum.

Potential theory-based software overestimate the wave elevation between close ships, since they disregard important viscous effects and thus lead to undamped resonant modes on the calculated wave elevation between the vessels. This problem may be overcome through modeling of a “lid” over the gap between the ships hulls, that is, an additional structure considered in the hydrodynamic calculations whose motions emulate the free surface elevation (BUCHNER, VAN DIJK and DE WILDE, 2001).

Models for the suction and repulsion forces that appear when two ships navigate parallel in calm water are available, but almost always refer to the case of maneuvering in channels, corresponding thus to shallow water. Some of them are (VARYANI, THAVALINGAM and KRISHNANKUTTY, 2004), where a model for calculating interaction loads is proposed and (VANTORRE, VERZHBITSKAYA and LAFORCE, 2002), which presents formulations based on model tests. (DE DECKER, 2006) used experimental shallow water data to develop a model for the side-by-side case, that is, with zero-relative speed. Analytical solutions are proposed in (WANG, 2007) and (XIANG and FALTINSEN, 2011).

The main concern for the convoy formation relates to the control of an underactuated system. Therefore, control of lateral motions is done indirectly by the shuttle tanker autopilot, whose heading references are generated through the *line-of-sight* guidance method. This is described in (BREIVIK, 2003) and (FOSSEN, BREIVIK and SKJETNE, 2003). Since the trajectory of the shuttle tanker is defined by the VLCC motions, the problem is one of *way-point tracking*, which is treated in (BREIVIK, HOVSTEIN and FOSSEN, 2008). These references also propose control strategies for both surge velocity and yaw moment. A problem involving path-following and maintenance of a given formation pattern is treated in (SOUZA, OSHIRO and MORISHITA, 2010). However, it relates to a very low-speed situation, so that all ships may control their horizontal positions by means of tunnel thrusters.

1.3 OBJECTIVES

The purpose of the present work is to analyze the viability of two different alternatives of oil transfer between two ships in open sea, viz, side-by-side and convoy configurations. The task is divided into three main stages:

- a. Development of dynamic models and control approaches for two different configurations of ship-to-ship oil transfer operations in a seaway, viz.: side-by-side and convoy formation.
- b. Implementation of numerical simulators based on the resultant models.
- c. Analysis of the results and conclusions about the feasibility of each configuration, based on environmental conditions and operational aspects (e.g. mooring arrangements, thrusters' capacity, etc).

Once each situation demands a different approach for dynamics and control, it may be more convenient to list the objectives for each operation individually:

Side-by-side

- Formulation of the nonlinear equations of motions in 6 degrees of freedom correspondent to a unified approach for both maneuvering and seakeeping.
- Development of models for the loads involved in the operation, viz., hydrodynamic interaction loads, fenders, mooring system and environment.
- Discussion about the calculation of hydrodynamic data for ships in interaction.
- Design of a control law for surge and yaw motions of the guide ship.
- Time-domain simulations for different environmental conditions, mooring arrangements and loading conditions. Analysis of the mooring lines tractions during the operation and determination of the suitable mooring arrangements for a given environmental condition.

Convoy

- Development of a maneuvering model based on hydrodynamic derivatives, including environmental action.
- Design of an autopilot for the shuttle tanker, based on the line-of-sight strategy, a backstepping controller and nonlinear controller observer.
- Simulations for test of the LOS-based autopilot, considering different incidence and harshness of the environmental agents, in order to verify if the shuttle tanker autopilot is able to properly follow the VLCC without hose disconnection or collisions.

1.4 TEXT ORGANIZATION

The necessary theoretical background for the development of dynamic modeling is considered in Chapter 2. It starts presenting the adopted notation, following with coordinate systems, kinematics and rigid-body dynamics. Then, basic hydrodynamics are discussed, followed by a review on environmental loads and models for their consideration in the ship dynamics. Finally, the 6 DOF equations of motions for maneuvering and seakeeping are derived, followed by a unified model for both approaches.

Chapter 3 introduces notions of control systems design. The PID controller is presented, followed by the nonlinear backstepping control strategy. Then, a nonlinear observer based on passivity theory is presented, and the chapter ends with a description of the line-of-sight method for guidance, which is used in the convoy formation operation.

Underway side-by-side operations are particularly considered in Chapter 4. An overview of a complete operation is briefly presented, followed by a discussion on the hydrodynamics interactions and the introduction of methods for calculating the hydrodynamic data. Then, the operation modeling is developed. The coupled equations of motions for the unified maneuvering and seakeeping approach are written, and models for hydrodynamic interaction, fenders, mooring system and environment are proposed.

The convoy operation is detailed in Chapter 5. First, the maneuvering model introduced in Chapter 4 is adapted to be applied with a model of hydrodynamic derivatives. Then, the algorithm for references generation is proposed, and the control approaches presented on Chapter 3 are utilized for development of the shuttle tanker autopilot system. The chapter ends with models for the actuators dynamics.

Simulations procedures and their respective results are exposed on Chapter 6. The ships dimensions for all loading cases are presented, and the combinations of drafts – and, consequently, freeboards – are listed for each loading condition. Following, simulations results for the side-by-side operation are presented, and all the same is done for the convoy operation. Final considerations and suggestions for future works are presented on Chapter 7.

2. DYNAMIC MODELING

Modeling of ship dynamics involves an elaborate combination of rigid-body theory and hydrodynamics. In fact, ship motions are intrinsically complex due to their highly coupled character and to the complicated response of a vessel to its interaction with the surrounding fluid. Thus, a reasonable comprehension on the physical origins of the forces and moments acting on the system is imperative for a clear understanding and mathematical description of the motions.

Ship motions may hardly be analyzed by means of a single system of coordinates. It is convenient to approach each sort of problem with an appropriate frame, such that distinct systems are usually utilized. Therefore, it is necessary to establish a clear relation between the coordinates of different frames, allowing the solutions obtained for one of them to be straightforwardly related to the other one.

Environment plays an important role in ship dynamics and must be considered in the dynamics formulation through the usage of reliable models available in the literature. Furthermore, it is also interesting to have some comprehension on the way such environment agents disturb the system, such that these models may be properly applied to the model.

Usually, ship dynamics are divided into two main areas of study, viz., *maneuvering* and *seakeeping*. The first of them comprises the analysis of a vessel response to its control surfaces (like rudders and similar), propulsion system and low-frequency environment loads. Water is admitted to be calm, that is, no 1st order wave loads are considered. Seakeeping, on the other hand, refers to the behavior of a ship when excited by waves. Sometimes, however, the practice of separating maneuvering from seakeeping does not comply with the requirements of the problem, such that a unified approach should be used.

2.1 NOTATION

The position and motion of a rigid-body in space are described in 6 degrees of freedom (DOF). Therefore, 6 independent variables are necessary to model a ship moving in the ocean. Three of them are used to assign the position, while the other three define the ship angles of orientation.

The notation adopted in this work to describe generalized positions, velocities and forces in 6 DOF is that introduced by *The Society of Naval Architects and Marine Engineers* (SNAME, 1950), as presented in Table 2.1.

Table 2.1 – Notation for generalized positions, velocities and forces (SNAME, 1950).

DOF	Motion	Positions/Euler angles	Linear/angular velocities	Forces/moments
1	surge	x	u	X
2	sway	y	v	Y
3	heave	z	w	Z
4	roll	ϕ	p	K
5	pitch	θ	q	M
6	yaw	ψ	r	N

Ship dynamics may be conveniently formulated in the vectorial notation presented in (FOSSÉN, 1994):

$$\begin{aligned}\boldsymbol{\eta}_1 &= [x, y, z]^T \\ \boldsymbol{\eta}_2 &= [\phi, \theta, \psi]^T\end{aligned}\tag{2.1}$$

$$\begin{aligned}\boldsymbol{\eta} &= [\boldsymbol{\eta}_1^T, \boldsymbol{\eta}_2^T]^T \\ \mathbf{v}_1 &= [u, v, w]^T \\ \mathbf{v}_2 &= [p, q, r]^T\end{aligned}\tag{2.2}$$

$$\begin{aligned}\mathbf{v} &= [\mathbf{v}_1^T, \mathbf{v}_2^T]^T \\ \boldsymbol{\tau}_1 &= [X, Y, Z]^T \\ \boldsymbol{\tau}_2 &= [K, M, N]^T\end{aligned}\tag{2.3}$$

$$\boldsymbol{\tau} = [\boldsymbol{\tau}_1^T, \boldsymbol{\tau}_2^T]^T$$

This approach leads to a compact formulation for the equations of motions based on vectors and matrices, as it will be seen later in this chapter.

2.2 COORDINATE SYSTEMS

The position and motion of a ship in 6 DOF are usually described according to three dextral orthogonal coordinate systems, namely (PEREZ and FOSSEN, 2007):

- The Earth-fixed coordinate system, also called *n*-frame
- The seakeeping coordinate system, also called *s*-frame
- The body-fixed coordinate system, also called *b*-frame

Earth-fixed coordinate system (*n*-frame). With its origin o_n fixed in a plane tangent to the Earth surface, this system is admitted to be an inertial frame⁶. The x_n -axis points towards North, the y_n -axis points towards East and the z_n -axis points downwards, perpendicular to a plane tangential to the Earth in o_n (Figure 2.1). The vectors of *positions* η_1 and of *Euler angles* η_2 compose the *vector of positions* η , and are defined according to the *n*-frame, as they relate to the *absolute* position and orientation of the ship.

Seakeeping coordinate system (*s*-frame). This coordinate system is considered to move with the ship, with both constant speed and heading corresponding to the average motion of the vessel (supposed to perform a straight trajectory with mean uniform velocity). Its origin O_s is defined in a way to let the z_s -axis cross the ship center of gravity. The horizontal x_s and y_s axes are assumed to keep parallel to the still water surface, such that the ship oscillates around the frame as it is excited by waves. The x_s -axis points forward, the y_s -axis points starboard and the z_s -axis points downwards. This frame is most appropriate for calculation of radiation and wave excitation forces and moments, for the wave elevation at the ship hull may be evaluated around its mean position and used as input for hydrodynamic solvers. A vector of generalized positions of the *s*-frame in respect to the body-fixed coordinate system (described below) may be defined as:

$$\xi = [\xi_1, \xi_2, \xi_3, \xi_4, \xi_5, \xi_6]^T \quad (2.4)$$

⁶ This is a reasonable assumption, since marine vehicles velocities are generally low and, therefore, the inertial forces due to the Earth rotation become negligible in comparison to the hydrodynamic forces involved.

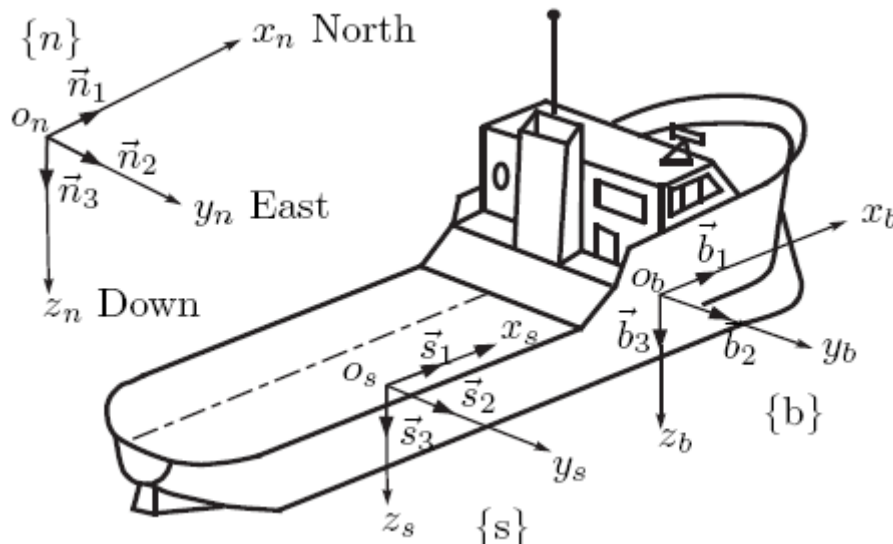


Figure 2.1 – Coordinate systems (PEREZ and FOSSEN, 2007).

Body-fixed coordinate system (b -frame). The b -frame is considered to be fixed to the ship. The origin o_b may be placed anywhere, but it is a common practice to consider it to be settled amidships, in the intersection between the longitudinal plane of symmetry and the design water level. The x_b -axis points the bow, the y_b -axis points starboard and the z_b -axis points downwards. Since it is attached to the moving body, the frame oscillates around the s -frame. Besides, the velocities and accelerations vector \mathbf{v} of the ship with respect to the Earth-fixed system are expressed in the b -frame, so that the forces and moments are decomposed in respect to its axes. Therefore, the maneuvering equations of motions are formulated around o_b .

2.3 KINEMATIC TRANSFORMATIONS

When dealing with different coordinate systems, it is imperative to develop a practical procedure to transform the coordinates given in one frame into those correspondents to the other. This is performed through the usage of the so called *rotation matrices*, whose calculation will be derived below.

2.3.1 Rotation matrices

Let \mathbf{R}_a^b denote the rotation matrix which transforms a vector from a frame a to a frame b , that is⁷:

⁷ The notation \mathbf{v}_O^a refers to a vector in point O decomposed in coordinates of frame a .

$$\mathbf{v}_0^b = \mathbf{R}_a^b \mathbf{v}_0^a \quad (2.5)$$

The matrix \mathbf{R}_a^b is an element of $SO(3)$, that is, the set of *special orthogonal matrices of order 3*:

$$SO(3) = \{\mathbf{A} | \mathbf{A} \in \mathbb{R}^{3 \times 3}, \mathbf{A}^{-1} = \mathbf{A}^T, \det(\mathbf{A}) = 1\} \quad (2.6)$$

A rotation of frame b relative to frame a is called *simple* when it is performed about a single axis. According to Euler's theorem of rotation, it is possible to describe any change in the relative orientation of two reference frames a and b by means of a simple rotation of b about a . Therefore, if the rotation is performed about an axis parallel to the unit vector $\boldsymbol{\lambda} = [\lambda_1, \lambda_2, \lambda_3]$ and by an angle α , the rotation matrix \mathbf{R}_a^b may also be denoted as $\mathbf{R}_{\boldsymbol{\lambda}, \alpha}$ and is calculated according to (FOSSSEN, 2002):

$$\mathbf{R}_{\boldsymbol{\lambda}, \alpha} = \mathbf{I}_{3 \times 3} + \sin(\alpha) \mathbf{S}(\boldsymbol{\lambda}) + [1 - \cos(\alpha)] \mathbf{S}^2(\boldsymbol{\lambda}) \quad (2.7)$$

where $\mathbf{I}_{3 \times 3}$ is an identity matrix of order 3 and $\mathbf{S}(\boldsymbol{\lambda})$ is a *skew-symmetric*⁸ matrix defined as:

$$\mathbf{S}(\boldsymbol{\lambda}) = \begin{bmatrix} 0 & -\lambda_3 & \lambda_2 \\ \lambda_3 & 0 & -\lambda_1 \\ -\lambda_2 & \lambda_1 & 0 \end{bmatrix} \quad (2.8)$$

Using formula (2.7), the simple rotations ϕ , θ and ψ about the n -frame axes x_n , y_n and z_n , respectively, may be performed through the following rotation matrices:

$$\mathbf{R}_{x_n, \phi} = \begin{bmatrix} 1 & 0 & 0 \\ 0 & c\phi & -s\phi \\ 0 & s\phi & c\phi \end{bmatrix} \quad (2.9)$$

$$\mathbf{R}_{y_n, \theta} = \begin{bmatrix} c\theta & 0 & s\theta \\ 0 & 1 & 0 \\ -s\theta & 0 & c\theta \end{bmatrix} \quad (2.10)$$

⁸ A matrix \mathbf{S} is said to be *skew-symmetric* if it verifies $\mathbf{S} = -\mathbf{S}^T$. The skew-symmetric matrix can be used to perform the cross-product of two vectors \mathbf{u} and \mathbf{v} , once it may be verified that $\mathbf{u} \times \mathbf{v} = \mathbf{S}(\mathbf{v})^T \mathbf{u}$.

$$\mathbf{R}_{z_n, \psi} = \begin{bmatrix} c\psi & -s\psi & 0 \\ s\psi & c\psi & 0 \\ 0 & 0 & 1 \end{bmatrix} \quad (2.11)$$

where “c ·” denotes “cos(·)”, “s ·” denotes “sin(·)” and ϕ , θ and ψ , presented in Table 2.1, are called *Euler angles*.

2.3.2 Transformation from *b*-frame to *h*-frame

As stated in (2.6), the *b*-frame oscillates in respect to the *h*-frame by the angles ξ_4 , ξ_5 and ξ_6 , which relate to the Euler angles according to (FOSSSEN, 2005):

$$\xi_4 = \phi \quad (2.12)$$

$$\xi_5 = \theta \quad (2.13)$$

$$\xi_6 = \psi - \frac{1}{T} \int_t^{t+T} \psi(\tau) d\tau \quad (2.14)$$

Equation (2.14) states that ξ_6 is taken as the time average of the yaw oscillation in a period T . Denoting $\Theta_s = [\xi_4, \xi_5, \xi_6]^T$, the rotation matrix $\mathbf{R}_b^s(\Theta_s)$ is then given by:

$$\mathbf{R}_b^s(\Theta_s) = \mathbf{R}_{z_b, \xi_6} \mathbf{R}_{y_b, \xi_5} \mathbf{R}_{x_b, \xi_4} \quad (2.15)$$

with (assuming small angle⁹ rotations):

$$\mathbf{R}_{x_b, \xi_4} = \begin{bmatrix} 1 & 0 & 0 \\ 0 & 1 & -\xi_4 \\ 0 & \xi_4 & 1 \end{bmatrix} \quad (2.16)$$

$$\mathbf{R}_{y_b, \xi_5} = \begin{bmatrix} 1 & 0 & \xi_5 \\ 0 & 1 & 0 \\ -\xi_5 & 0 & 1 \end{bmatrix} \quad (2.17)$$

$$\mathbf{R}_{z_b, \xi_6} = \begin{bmatrix} 1 & -\xi_6 & 0 \\ \xi_6 & 1 & 0 \\ 0 & 0 & 1 \end{bmatrix} \quad (2.18)$$

Hence, $\mathbf{R}_b^s(\Theta_s)$ assumes the following form:

⁹ Such that the approximations $\sin(\alpha) \approx \alpha$ and $\cos(\alpha) \approx 1$ hold.

$$\mathbf{R}_b^s(\boldsymbol{\Theta}_s) = \begin{bmatrix} 1 & -\xi_6 & \xi_5 \\ \xi_6 & 1 & -\xi_4 \\ -\xi_5 & \xi_4 & 1 \end{bmatrix} \quad (2.19)$$

It is easy to notice that the angular velocities of both the Earth-fixed and the seakeeping coordinate systems in respect to the body-fixed frame are equal, i.e.:

$$\boldsymbol{\omega}_{bn}^b = \boldsymbol{\omega}_{bs}^b \quad (2.20)$$

Therefore, the velocity of the s -frame origin in respect to the b -frame $\mathbf{v}_{o_s}^b$ may be obtained from vectorial kinematics:

$$\mathbf{v}_{o_s}^b = \mathbf{v}_{o_n}^b + \boldsymbol{\omega}_{bn}^b \times \mathbf{r}_{o_s}^b \quad (2.21)$$

$\mathbf{r}_{o_s}^b$ being the vector from o_n to o_s . Thus, the following relationship holds:

$$\begin{bmatrix} \mathbf{v}_{o_s}^b \\ \boldsymbol{\omega}_{bs}^b \end{bmatrix} = \mathbf{H}(\mathbf{r}_{o_s}^b) \begin{bmatrix} \mathbf{v}_{o_n}^b \\ \boldsymbol{\omega}_{bn}^b \end{bmatrix} \quad (2.22)$$

with the matrix $\mathbf{H}(\mathbf{r}_{o_s}^b)$ given by:

$$\mathbf{H}(\mathbf{r}_{o_s}^b) = \begin{bmatrix} \mathbf{I}_{3 \times 3} & \mathbf{S}(\mathbf{r}_{o_s}^b) \\ \mathbf{0}_{3 \times 3} & \mathbf{I}_{3 \times 3} \end{bmatrix} \quad (2.23)$$

From (2.19) and (2.23) one obtains:

$$\begin{bmatrix} \mathbf{R}_s^b(\boldsymbol{\Theta}_s) & \mathbf{0}_{3 \times 3} \\ \mathbf{0}_{3 \times 3} & \mathbf{R}_s^b(\boldsymbol{\Theta}_s) \end{bmatrix} \begin{bmatrix} \mathbf{v}_{o_s}^s \\ \boldsymbol{\omega}_{bs}^s \end{bmatrix} = \mathbf{H}(\mathbf{r}_{o_s}^b) \begin{bmatrix} \mathbf{v}_{o_n}^b \\ \boldsymbol{\omega}_{bn}^b \end{bmatrix} \quad (2.24)$$

Noticing that $\mathbf{R}_s^b(\boldsymbol{\Theta}_s) = \mathbf{R}_b^s(\boldsymbol{\Theta}_s)^{-1}$, it comes from (2.24):

$$\mathbf{v}_{o_s}^s = \mathbf{R}_b^s(\boldsymbol{\Theta}_s) \left[\mathbf{v}_{o_s}^s + \mathbf{S}(\mathbf{r}_{o_s}^b)^T \boldsymbol{\omega}_{bs}^b \right] \quad (2.25)$$

$$\boldsymbol{\omega}_{bs}^s = \mathbf{R}_b^s(\boldsymbol{\Theta}_s) \boldsymbol{\omega}_{bs}^b \quad (2.26)$$

Considering that the s -frame moves with constant speed U and that ξ_6 is small, the velocities of the b -frame are given by:

$$\begin{aligned}
u &= U + \delta u \\
v &= \delta v \\
w &= \delta w \\
p &= \delta p \\
q &= \delta q \\
r &= \delta r
\end{aligned} \tag{2.27}$$

Assuming longitudinal symmetry and that the ship is sufficiently slender, it may be considered that motions in surge, heave and pitch are decoupled from sway, roll and yaw. Besides, it is also admitted that higher-order terms are negligible, such that equations (2.25) and (2.26) may be expanded as:

$$\begin{aligned}
\dot{\xi}_1 &= \delta u + z_{o_s} \delta q \\
\dot{\xi}_2 &= \delta v + x_{o_s} \delta r - z_{o_s} \delta p + U \xi_6 \\
\dot{\xi}_3 &= \delta w - x_{o_s} \delta q - U \xi_5 \\
\dot{\xi}_4 &= \delta p \\
\dot{\xi}_5 &= \delta q \\
\dot{\xi}_6 &= \delta r
\end{aligned} \tag{2.28}$$

Consequently,

$$\begin{aligned}
\ddot{\xi}_1 &= \delta \dot{u} + z_{o_s} \delta \dot{q} \\
\ddot{\xi}_2 &= \delta \dot{v} + x_{o_s} \delta \dot{r} - z_{o_s} \delta \dot{p} + U \delta r \\
\ddot{\xi}_3 &= \delta \dot{w} - x_{o_s} \delta \dot{q} - U \delta q \\
\ddot{\xi}_4 &= \delta \dot{p} \\
\ddot{\xi}_5 &= \delta \dot{q} \\
\ddot{\xi}_6 &= \delta \dot{r}
\end{aligned} \tag{2.29}$$

Considering sinusoidal motions for both pitch and yaw:

$$\begin{aligned}
\xi_5 &= A_1 \sin(\omega_e t) & \xi_6 &= A_2 \sin(\omega_e t) \\
\dot{\xi}_5 &= \omega_e A_1 \cos(\omega_e t) & \dot{\xi}_6 &= \omega_e A_2 \cos(\omega_e t) \\
\ddot{\xi}_5 &= -\omega_e^2 A_1 \sin(\omega_e t) & \ddot{\xi}_6 &= -\omega_e^2 A_2 \sin(\omega_e t)
\end{aligned} \tag{2.30}$$

where A_1 and A_2 are the motions amplitudes and ω_e is the *frequency of encounter*, given by:

$$\omega_e = \left| \omega - \frac{U}{g} \omega^2 \cos(\psi_r) \right| \tag{2.31}$$

with g being the acceleration of gravity and ψ_r the relative wave incidence. From (2.30), it is easy to notice that:

$$\begin{aligned}\xi_5 &= -\frac{1}{\omega_e^2} \ddot{\xi}_5 \\ \xi_6 &= -\frac{1}{\omega_e^2} \ddot{\xi}_6\end{aligned}\tag{2.32}$$

Hence, the set of equations (2.28) may be rewritten as:

$$\begin{aligned}\dot{\xi}_1 &= \delta u + z_{o_s} \delta q \\ \dot{\xi}_2 &= \delta v + x_{o_s} \delta r - z_{o_s} \delta p - \frac{U}{\omega_e^2} \delta \dot{r} \\ \dot{\xi}_3 &= \delta w - x_{o_s} \delta q + \frac{U}{\omega_e^2} \delta \dot{r} \\ \dot{\xi}_4 &= \delta p \\ \dot{\xi}_5 &= \delta q \\ \dot{\xi}_6 &= \delta r\end{aligned}\tag{2.33}$$

Finally, assigning the following form for the matrices \mathbf{J}_s and \mathbf{L}_s :

$$\mathbf{J}_s = \begin{bmatrix} 1 & 0 & 0 & 0 & z_{o_s} & 0 \\ 0 & 1 & 0 & -z_{o_s} & 0 & x_{o_s} \\ 0 & 0 & 1 & 0 & -x_{o_s} & 0 \\ 0 & 0 & 0 & 1 & 0 & 0 \\ 0 & 0 & 0 & 0 & 1 & 0 \\ 0 & 0 & 0 & 0 & 0 & 1 \end{bmatrix}\tag{2.34}$$

$$\mathbf{L}_s = \begin{bmatrix} 0 & 0 & 0 & 0 & 0 & 0 \\ 0 & 0 & 0 & 0 & 0 & 1 \\ 0 & 0 & 0 & 0 & -1 & 0 \\ 0 & 0 & 0 & 0 & 0 & 0 \\ 0 & 0 & 0 & 0 & 0 & 0 \\ 0 & 0 & 0 & 0 & 0 & 0 \end{bmatrix}\tag{2.35}$$

the relation between the s -frame and the b -frame is then given by:

$$\dot{\xi} = \mathbf{J}_s \delta \mathbf{v} - \frac{U}{\omega_e^2} \mathbf{L}_s \delta \dot{\mathbf{v}}\tag{2.36}$$

$$\ddot{\xi} = \mathbf{J}_s \delta \dot{\mathbf{v}} + U \mathbf{L}_s \delta \mathbf{v}\tag{2.37}$$

with $\delta \mathbf{v}$ defined according to:

$$\delta \mathbf{v} = [\delta u, \delta v, \delta w, \delta p, \delta q, \delta r]^T \quad (2.38)$$

2.3.3 Transformation from \mathbf{b} -frame to \mathbf{n} -frame

The rotation matrix from the body-fixed frame to the Earth-fixed coordinate system is calculated by:

$$\mathbf{R}_b^n(\boldsymbol{\eta}_2) = \mathbf{R}_{z_n, \psi} \mathbf{R}_{y_n, \theta} \mathbf{R}_{x_n, \phi} \quad (2.39)$$

From equations (2.9)-(2.11), it follows that:

$$\mathbf{R}_b^n(\boldsymbol{\eta}_2) = \begin{bmatrix} c\psi c\theta & -s\psi c\phi + c\psi s\theta s\phi & s\psi s\phi + c\psi c\phi s\theta \\ s\psi c\theta & c\psi c\phi + s\psi s\theta s\phi & -c\psi s\phi + s\theta s\psi c\phi \\ -s\theta & c\theta s\phi & c\theta c\phi \end{bmatrix} \quad (2.40)$$

Therefore, the position vector time-derivative $\dot{\boldsymbol{\eta}}_1$ is related to the velocity vector \mathbf{v}_1 according to:

$$\dot{\boldsymbol{\eta}}_1 = \mathbf{R}_b^n(\boldsymbol{\eta}_2) \mathbf{v}_1 \quad (2.41)$$

Similarly, the time-derivatives of the Euler angles may be related to \mathbf{v}_2 according to:

$$\dot{\boldsymbol{\eta}}_2 = \mathbf{T}_a(\boldsymbol{\eta}_2) \mathbf{v}_2 \quad (2.42)$$

with the *Euler angle attitude matrix* $\mathbf{T}_a(\boldsymbol{\eta}_2)$ defined as:

$$\mathbf{T}_a(\boldsymbol{\eta}_2) = \begin{bmatrix} 1 & s\phi t\theta & c\phi t\theta \\ 0 & c\phi & -s\phi \\ 0 & s\phi/c\theta & c\phi/c\theta \end{bmatrix} \quad (2.43)$$

where “t.” denotes “tan(·)”. It is important to emphasize that $\mathbf{T}_a(\boldsymbol{\eta}_2)$ is not defined for $\theta = \frac{\pi}{2} \pm n\pi$, $n \in \mathbb{N}$. This is not a problem for a surface vessel, though, since it is absolutely unlikely for a ship to get such high pitch angles.

2.4 SHIP DYNAMICS

2.4.1 Inertia matrix

The ship 6 DOF rigid-body inertia is represented by the following matrix:

$$\mathbf{M}_{RB} = \begin{bmatrix} m & 0 & 0 & 0 & mz_g & -my_g \\ 0 & m & 0 & -mz_g & 0 & mx_g \\ 0 & 0 & m & my_g & -mx_g & 0 \\ 0 & -mz_g & my_g & I_x & -I_{xy} & -I_{xz} \\ mz_g & 0 & -mx_g & -I_{yx} & I_y & -I_{yz} \\ -my_g & mx_g & 0 & -I_{zx} & -I_{zy} & I_z \end{bmatrix} \quad (2.44)$$

with m being the ship mass, x_g , y_g and z_g the coordinates of its center of gravity with respect to o_b and I_i and I_{ij} ($i \neq j$) the momenta and products of inertia, respectively.

2.4.2 Rigid-body dynamics

The development of a mathematical model for the ships dynamics will follow the *Newton-Euler formulation*, as proposed in (FOSSSEN, 2002). Everything starts with Newton's Second law, which relates force \mathbf{f} , mass m and acceleration $\dot{\mathbf{v}}$ according to:

$$\mathbf{f} = m\dot{\mathbf{v}} \quad (2.45)$$

Newton's expression was further explored by Euler, who formulated it in terms of conservation of linear ($\mathbf{p} = m\mathbf{v}$) and angular ($\mathbf{h} = I\boldsymbol{\omega}_{ab}$) momenta. The so-called *Euler's First and Second Axioms* are respectively expressed as:

$$\dot{\mathbf{p}} = \mathbf{f} \quad (2.46)$$

$$\dot{\mathbf{h}} = \mathbf{m} \quad (2.47)$$

\mathbf{m} being the momentum acting on the body. Two models will now be formulated, referring for both the b - and the s -frames.

***b*-frame (maneuvering) formulation**

The symmetry properties of marine vehicles encourage a formulation developed for the body-fixed coordinate system. However, (2.45) holds only for inertial systems, such that some relation between accelerations on both the n - and b -frames must be derived. Denoting \mathbf{v}_g^b the velocity of the ship center of gravity CG and \mathbf{r}_g^b its distance vector from o_b , rigid-body condition states that:

$$\mathbf{v}_g^b = \mathbf{v}_{o_b}^b + \boldsymbol{\omega}_{nb}^b \times \mathbf{r}_g^b \quad (2.48)$$

where $\boldsymbol{\omega}_{nb}^b = \mathbf{v}_2$. Therefore,

$$\mathbf{v}_g^n = \mathbf{R}_b^n \mathbf{v}_g^b = \mathbf{R}_b^n (\mathbf{v}_{o_b}^b + \boldsymbol{\omega}_{nb}^b \times \mathbf{r}_g^b) \quad (2.49)$$

Time differentiating \mathbf{v}_g^n and substituting in Euler's first axiom (2.46) yields:

$$m[\dot{\mathbf{v}}_{o_b}^b + \mathbf{S}(\dot{\boldsymbol{\omega}}_{nb}^b)\mathbf{r}_g^b + \mathbf{S}(\boldsymbol{\omega}_{nb}^b)\mathbf{v}_{o_b}^b + \mathbf{S}^2(\boldsymbol{\omega}_{nb}^b)\mathbf{r}_g^b] = \mathbf{f}_o^b \quad (2.50)$$

For the rotational motion, it is first necessary to write the expressions for the angular momenta in o_b and CG with respect to the b -frame, $\mathbf{h}_{o_b}^b$ and \mathbf{h}_g^b :

$$\mathbf{h}_{o_b}^b = \mathbf{I}_{o_b} \boldsymbol{\omega}_{nb}^b + m\mathbf{r}_g^b \times \mathbf{v}_{o_b}^b \quad (2.51)$$

$$\mathbf{h}_g^b = \mathbf{h}_{o_b}^b - m\mathbf{r}_g^b \times \mathbf{v}_g^b \quad (2.52)$$

where \mathbf{I}_{o_b} is a partition from \mathbf{M}_{RB} :

$$\mathbf{I}_{o_b} = \begin{bmatrix} I_x & -I_{xy} & -I_{xz} \\ -I_{yx} & I_y & -I_{yz} \\ -I_{zx} & -I_{zy} & I_z \end{bmatrix} \quad (2.53)$$

Differentiating (2.52) and applying Euler's second axiom (2.47) yields:

$$\mathbf{I}_{o_b} \dot{\boldsymbol{\omega}}_{nb}^b + \mathbf{S}(\boldsymbol{\omega}_{nb}^b)\mathbf{I}_{o_b} \boldsymbol{\omega}_{nb}^b + m\mathbf{S}(\mathbf{r}_g^b)\dot{\mathbf{v}}_{o_b}^b + m\mathbf{S}(\mathbf{r}_g^b)\mathbf{S}(\boldsymbol{\omega}_{nb}^b)\mathbf{v}_{o_b}^b = \mathbf{m}_o^b \quad (2.54)$$

The total set of maneuvering 6 DOF equations of motion comes from (2.50) and (2.54):

$$\begin{aligned} m[\dot{u} - vr + wq - x_g(q^2 + r^2) + y_g(pq - \dot{r}) + z_g(pr + \dot{q})] &= X \\ m[\dot{v} - wp + ur - y_g(r^2 + p^2) + z_g(qr - \dot{p}) + z_g(qp + \dot{r})] &= Y \\ m[\dot{w} - uq + vp - z_g(p^2 + q^2) + x_g(rp - \dot{q}) + y_g(rq + \dot{p})] &= Z \\ I_x \dot{p} + (I_z - I_y)qr - (\dot{r} + pq)I_{xz} + (r^2 - q^2)I_{yz} + (pr - \dot{q})I_{xy} \\ &\quad + m[y_g(\dot{w} - uq + vp) - z_g(\dot{v} - wp + ur)] = K \\ I_y \dot{q} + (I_x - I_z)rp - (\dot{p} + qr)I_{xy} + (p^2 - r^2)I_{zx} + (qp - \dot{r})I_{yz} \\ &\quad + m[z_g(\dot{u} - vr + wq) - x_g(\dot{w} - uq + vp)] = M \\ I_z \dot{r} + (I_y - I_x)pq - (\dot{q} + rp)I_{yz} + (q^2 - p^2)I_{xy} + (rq - \dot{p})I_{zx} \\ &\quad + m[x_g(\dot{v} - wp + ur) - y_g(\dot{u} - vr + wq)] = N \end{aligned} \quad (2.55)$$

A more compact representation for (2.55) may be obtained using the vectorial formulation introduced in (FOSSSEN, 1991):

$$\mathbf{M}_{RB}\dot{\mathbf{v}} + \mathbf{C}_{RB}(\mathbf{v})\mathbf{v} = \boldsymbol{\tau} \quad (2.56)$$

with the *Coriolis and centripetal matrix* $\mathbf{C}_{RB}(\mathbf{v}) = -\mathbf{C}_{RB}^T(\mathbf{v})$ given by:

$$\mathbf{C}_{RB}(\mathbf{v}) = \begin{bmatrix} \mathbf{0}_{3 \times 3} & -m\mathbf{S}(\mathbf{v}_1) - m\mathbf{S}(\mathbf{v}_2)\mathbf{S}(\mathbf{r}_g^b) \\ -m\mathbf{S}(\mathbf{v}_1) + m\mathbf{S}(\mathbf{r}_g^b)\mathbf{S}(\mathbf{v}_2) & -\mathbf{S}(\mathbf{I}_0\mathbf{v}_2) \end{bmatrix} \quad (2.57)$$

The generalized forces vector $\boldsymbol{\tau}$ is composed by a parcel due to hydrodynamic and hydrostatic loads $\boldsymbol{\tau}_{hyd}$, an environment term $\boldsymbol{\tau}_{env}$ and a control loads vector $\boldsymbol{\tau}_{con}$, composed of forces/moments due to control, mooring, fenders and any other positioning element. Hence:

$$\boldsymbol{\tau} = \boldsymbol{\tau}_{hyd} + \boldsymbol{\tau}_{env} + \boldsymbol{\tau}_{con} \quad (2.58)$$

s-frame (seakeeping) formulation

Once the seakeeping coordinate system moves with constant speed and direction with respect to the Earth-fixed frame, it is also considered to be inertial. Therefore, Newton's Second Law may be directly applied:

$$\mathbf{M}_{RB,s}\ddot{\boldsymbol{\xi}} = \delta\boldsymbol{\tau} \quad (2.59)$$

Where $\mathbf{M}_{RB,s}$ is the inertia matrix calculated in terms of the *s*-frame, related to \mathbf{M}_{RB} according to:

$$\mathbf{M}_{RB} = \mathbf{J}_S^T \mathbf{M}_{RB,s} \mathbf{J}_S \quad (2.60)$$

Again, the generalized forces vector $\delta\boldsymbol{\tau}$ is a superposition of hydrodynamic (and hydrostatic), environmental and control loads:

$$\delta\boldsymbol{\tau} = \delta\boldsymbol{\tau}_{hyd} + \delta\boldsymbol{\tau}_{WF} + \delta\boldsymbol{\tau}_{con} \quad (2.61)$$

Where $\delta\boldsymbol{\tau}_{WF}$ corresponds to first-order wave loads, whose origin will be further explained in section 2.6. Environmental action other than 1st order wave loads are not in scope of seakeeping analysis.

2.5 HYDRODYNAMICS AND HYDROSTATICS

The hydrodynamic components of τ_{hyd} in equation (2.58) comprise radiation-induced and viscous forces and moments. In this section the origin of these loads are briefly discussed, and a model for their inclusion in the equations of motion is presented. Following, hydrostatic restoration is also presented, together with a method for their calculation in function of the ship properties and position in the Earth-fixed frame.

2.5.1 Radiation-induced components

Radiation-induced loads consist in the forces and moments originated in a body when it is forced to oscillate with wave excitation frequency, assuming that no incident waves are present (FALTINSEN, 1990). They can be calculated as the sum of two components – one proportional to the body accelerations, and other to its velocities. Therefore, it is usual to compute such loads through coefficients assigned as *added mass* and *potential damping*, respectively. These coefficients are obtained from linear potential theory.

Added mass and inertia

Added (*virtual*) mass and inertia may be conceived as coefficients that, when multiplied by the body acceleration, provide the loads from pressure effects in the structure when it oscillates due to a forced motion. Added mass is a function of wave frequency, as illustrated in Figure 2.2. It is important to point out the asymptotic behavior of the data for $\omega_e \rightarrow \infty$.

It is convenient to represent added mass with a *matrix of added mass and inertia* \mathbf{A} , defined as:

$$\mathbf{A} = \mathbf{A}(\omega_e) = - \begin{bmatrix} X_{\dot{u}} & X_{\dot{v}} & X_{\dot{w}} & X_{\dot{p}} & X_{\dot{q}} & X_{\dot{r}} \\ Y_{\dot{u}} & Y_{\dot{v}} & Y_{\dot{w}} & Y_{\dot{p}} & Y_{\dot{q}} & Y_{\dot{r}} \\ Z_{\dot{u}} & Z_{\dot{v}} & Z_{\dot{w}} & Z_{\dot{p}} & Z_{\dot{q}} & Z_{\dot{r}} \\ K_{\dot{u}} & K_{\dot{v}} & K_{\dot{w}} & K_{\dot{p}} & K_{\dot{q}} & K_{\dot{r}} \\ M_{\dot{u}} & M_{\dot{v}} & M_{\dot{w}} & M_{\dot{p}} & M_{\dot{q}} & M_{\dot{r}} \\ N_{\dot{u}} & N_{\dot{v}} & N_{\dot{w}} & N_{\dot{p}} & N_{\dot{q}} & N_{\dot{r}} \end{bmatrix} \quad (2.62)$$

The term $-X_{\dot{v}} = -X_{\dot{v}}(\omega_e)$, for example, expresses the force X in surge due to an acceleration in sway \dot{v} , i.e.:

$$X = -X_{\dot{v}}\dot{v} \quad (2.63)$$

It is also necessary to define the *hydrodynamic Coriolis and centripetal matrix* $C_A(\mathbf{v})$. Let the symmetric matrix $\bar{\mathbf{A}}$ be defined as:

$$\bar{\mathbf{A}} = \frac{1}{2}(\mathbf{A} + \mathbf{A}^T) = \begin{bmatrix} \bar{\mathbf{A}}_{11} & \bar{\mathbf{A}}_{12} \\ \bar{\mathbf{A}}_{21} & \bar{\mathbf{A}}_{22} \end{bmatrix} \quad (2.64)$$

It comes that:

$$\mathbf{C}_A(\mathbf{v}) = \begin{bmatrix} \mathbf{0}_{3 \times 3} & -\mathbf{S}(\bar{\mathbf{A}}_{11}\mathbf{v}_1 + \bar{\mathbf{A}}_{12}\mathbf{v}_2) \\ -\mathbf{S}(\bar{\mathbf{A}}_{11}\mathbf{v}_1 + \bar{\mathbf{A}}_{12}\mathbf{v}_2) & -\mathbf{S}(\bar{\mathbf{A}}_{21}\mathbf{v}_1 + \bar{\mathbf{A}}_{22}\mathbf{v}_2) \end{bmatrix} \quad (2.65)$$

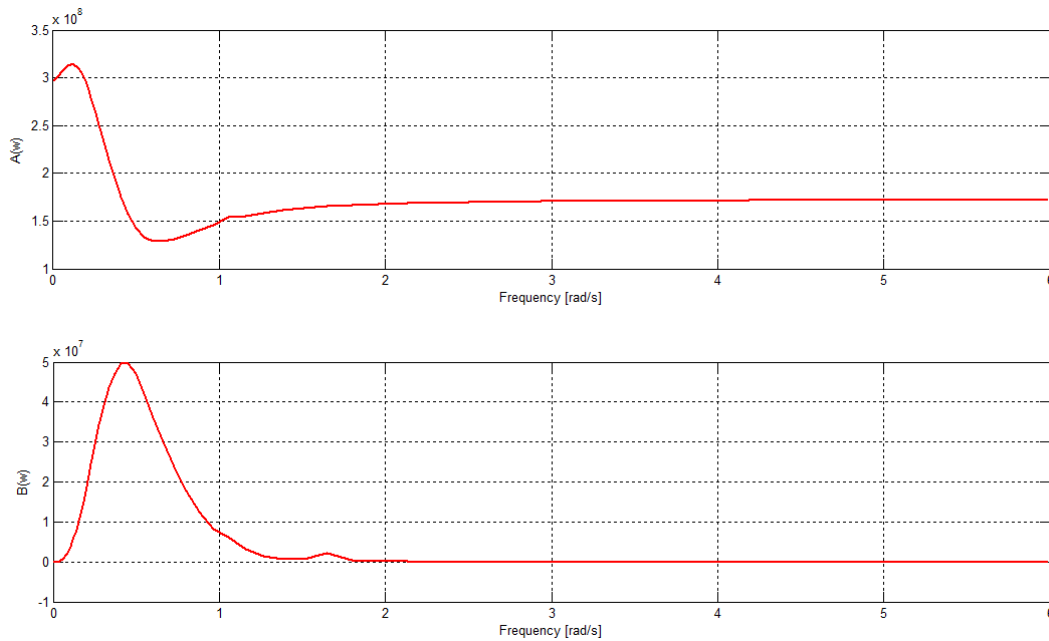


Figure 2.2 – Added mass (surge) for a tanker versus frequency of encounter.

Potential damping

An oscillating floating body damps energy in the form of irradiated waves. This is the principle behind so-called *potential damping*, dissipative forces proportional to the body velocities in 6 DOF. As in the case for added mass, potential damping may be calculated by coefficients that, when multiplied by the velocities, provide the correspondent forces and moments. Figure 2.2 shows that potential damping vanishes for both $\omega_e \rightarrow 0$ and $\omega_e \rightarrow \infty$. Hence, it is not a useful term to be considered for control system purposes, but will be important when fluid memory effects are to be regarded in the modeling, as presented in section 2.7.3. As for the added mass, a *potential damping matrix* \mathbf{B} may also be defined, such that loads due to radiation effects $\boldsymbol{\tau}_{rad}$ may be calculated according to:

$$\boldsymbol{\tau}_{rad} = \mathbf{A}\dot{\mathbf{v}} + \mathbf{B}\mathbf{v} + \mathbf{C}_A(\mathbf{v})\mathbf{v} \quad (2.66)$$

Both added mass and potential damping coefficients may be obtained from hydrodynamic software. These solvers may be based on both the panels-method (like *WAMIT* and *ANSYS AQWA*) or on the strip theory (like *VERES* and *Octopus Seaway*).

2.5.2 Viscous components

Viscous loads arise from viscid effects like skin friction and vortex shedding (FOSSEN, 2002). Skin friction forces may be considered as the sum of both a linear and a nonlinear component. The linear is based on laminar boundary layer theory, being very important in the low-frequency motion of a body (and, consequently, for the control system design). The nonlinear parcel originates from the turbulent boundary layer, and corresponds to a high-frequency contribution. Finally, by *vortex-shedding* one refers to the energy damped in form of vortices originated from the ship motion.

As observed in (SKJETNE, SMOGELI and FOSSEN, 2004), the damping component is the most uncertain among the parcels that compose the hydrodynamic loads. Let the damping loads vector $\mathbf{d}(\mathbf{v})$ be defined as:

$$\mathbf{d}(\mathbf{v}) = [X_d(\mathbf{v}), Y_d(\mathbf{v}), Z_d(\mathbf{v}), K_d(\mathbf{v}), M_d(\mathbf{v}), N_d(\mathbf{v})]^T \quad (2.67)$$

It is convenient to assign $\mathbf{d}(\mathbf{v})$ as a sum of linear and nonlinear components:

$$\mathbf{d}(\mathbf{v}) = \mathbf{D}_l\mathbf{v} + \mathbf{D}_n(\mathbf{v})\mathbf{v} = \mathbf{D}(\mathbf{v})\mathbf{v} \quad (2.68)$$

The terms inside \mathbf{D}_l and \mathbf{D}_n may be calculated according to truncated Taylor series expansions, as the widely used models proposed in (ABKOWITZ, 1964) and (NORRBIN, 1970). A representation for $Y_d(\mathbf{v})$ may be given, e.g., by:

$$Y_d(\mathbf{v}) = -Y_v v - Y_r r - Y_{|v|v} |v|v - Y_{|v|r} |v|r \dots \quad (2.69)$$

where the coefficients $Y_v, Y_{|v|v}, \dots$ may be obtained through PMM¹⁰ model tests. Some publications provide such coefficients, but they rarely relate to motions other than surge, sway, yaw and, sometimes, roll.

¹⁰ *Planar motion mechanism.*

2.5.3 Hydrostatic restoration

Restoration forces and moments arise from the balance between weight and buoyancy, as stated by Archimedes' principle. According to (FOSSSEN, 2002), the vector of restoration loads for box-shaped vessels $\mathbf{g}(\boldsymbol{\eta})$ may be approximated by a linear model, assuming yz -symmetry and small roll and pitch angles and heave displacement:

$$\mathbf{g}(\boldsymbol{\eta}) \approx \begin{bmatrix} 0 \\ 0 \\ \rho_w g A_{wp}(0) z \\ \rho_w g \nabla \overline{GM}_T \phi \\ \rho_w g \nabla \overline{GM}_L \theta \\ 0 \end{bmatrix} \quad (2.70)$$

where ρ_w is the water density, $A_{wp}(0)$ is the equilibrium water plane area, $\nabla = m/\rho_w$ is the volumetric displacement and \overline{GM}_T and \overline{GM}_L are the transversal and longitudinal metacentric heights, respectively. This approximation procedure is such that the vector $\mathbf{g}(\boldsymbol{\eta})$ is already projected on the body-fixed coordinate system. Let the *restoration matrix* \mathbf{G} be defined as:

$$\mathbf{G} = - \begin{bmatrix} 0 & 0 & 0 & 0 & 0 & 0 \\ 0 & 0 & 0 & 0 & 0 & 0 \\ 0 & 0 & \rho g A_{wp}(0) & 0 & 0 & 0 \\ 0 & 0 & 0 & \rho g \nabla \overline{GM}_T & 0 & 0 \\ 0 & 0 & 0 & 0 & \rho g \nabla \overline{GM}_L & 0 \\ 0 & 0 & 0 & 0 & 0 & 0 \end{bmatrix} \quad (2.71)$$

The vector $\mathbf{g}(\boldsymbol{\eta})$ may then be calculated according to:

$$\mathbf{g}(\boldsymbol{\eta}) = \mathbf{G}\boldsymbol{\eta} \quad (2.72)$$

Finally, the vector of hydrodynamic and hydrostatic forces and moments may be defined:

$$\boldsymbol{\tau}_{hyd} = -\boldsymbol{\tau}_{add} - \mathbf{d}(\mathbf{v}) - \mathbf{g}(\boldsymbol{\eta}) = -\mathbf{A}\dot{\mathbf{v}} - \mathbf{B}\mathbf{v} - \mathbf{C}_A(\mathbf{v}) - \mathbf{D}(\mathbf{v})\mathbf{v} - \mathbf{G}\boldsymbol{\eta} \quad (2.73)$$

2.6 ENVIRONMENT MODELS

Environmental loads in ocean vehicles and structures originate from three main agents, viz.

- Waves

- Wind
- Current

Thus, for simulation purposes it is necessary to adopt reliable models for both describing such phenomena and estimating their loads in ships. This topic will be approached in the present section.

2.6.1 Waves

Friction between wind and the ocean surface causes the appearance of small perturbations in the water. Persistent wind action makes such perturbations to grow until small waves begin to arise. These waves brake when they reach a certain height, and their associated energy is damped. Therefore, when an ocean storm begins a *developing sea* – characterized by short length λ waves – is observed. Thus, the wave energy spectrum of a developing sea presents high-frequency peak and narrow form. If the storm is long enough, a *fully developed sea* takes place and the energy is distributed along wave components with different associated frequencies. When the intense winds finally stop blowing, the predominant frequency starts to decay, such that long waves – known as *swells* – are then originated. From the dispersion relation for infinite water depth, the wave velocity is given by (FALTINSEN, 1990):

$$c = \frac{\omega}{k} = \frac{g}{\omega} \quad (2.74)$$

where $k = 2\pi/\lambda$ is the *wave number*. It may be concluded that low-frequency swells have higher velocities, such that they propagate for longer distances and may be observed very far from the place where they were originated.

The variation of wave elevation along the ship produces changes in the distribution of the pressure field acting in the hull, inducing forces and moments on it. Loads proportional to the wave height are called *first order wave loads* and have the same frequency as the exciting waves. Components proportional to the square of the wave height, on the other hand, are called *second order wave loads*, which may be divided in *slow drift* (very small frequency) and *mean drift* (zero frequency) forces.

1st order wave loads

Sea waves may be represented in the frequency domain through a *wave spectrum* $S_w(\omega)$:

$$S_w(\omega) = \lim_{\Delta\omega \rightarrow \infty} \frac{A^2(\omega)}{2\Delta\omega} \quad (2.75)$$

where $\Delta\omega$ is the frequency interval between two successive wave components, and A is the wave amplitude. The wave spectrum may be approximated by empirical expressions dependent on parameters which characterize the sea state, like the *significant wave height*¹¹ H_s and *peak period*¹² T_p . For developing seas, a widely used formulation is the *JONSWAP* spectrum, which was elaborated based on North-Sea wave elevation analyses:

$$S_w(\omega) = \frac{5H_s^2\omega_p^2[1 - 0,287 \ln(\gamma)]}{16\omega^5} \cdot \exp\left[-\frac{5}{4}\left(\frac{\omega_p}{\omega}\right)^4\right] \gamma^{\exp\left(-\frac{(\omega-\omega_p)^2}{2\sigma^2\omega_p^2}\right)} \quad (2.76)$$

where γ is a parameter related to the spectrum shape, ω_p is the peak frequency and σ is determined according to:

$$\sigma = \begin{cases} 0,07 & (\omega \leq \omega_p) \\ 0,09 & (\omega > \omega_p) \end{cases} \quad (2.77)$$

For fully developed seas, it is most convenient to use the *Pierson-Moskowitz* formulation:

$$S_w(\omega) = \frac{g^2}{123\omega^5} \exp\left[-\frac{5}{4}\left(\frac{\omega_p}{\omega}\right)^4\right] \quad (2.78)$$

Figure 2.3 shows both spectra calculated for $H_s = 5,0 \text{ m}$ and $T_p = 10,0 \text{ s}$.

First-order wave action in marine systems is usually regarded through the usage of *response amplitude operators* (RAOs). This approach is widely used in most applications and consists in calculating the body motions directly from the wave elevation time-series, other than integrating the 1st-order wave loads in the ship equations of motions.

¹¹ Mean value of the third highest waves among a set of measurements.

¹² Mean value of the periods between peaks of consecutive wave elevations.

RAOs are complex functions dependent on the wave-frequency and relative incidence direction:

$$RAO_i(j\omega, \beta_r) = \frac{y_i^{WF}(j\omega, \beta_r)}{\zeta} \quad (2.79)$$

where β_r is the wave relative incidence, y_i^{WF} is the amplitude of the wave-frequency motion in DOF i ($i = 1, 2, \dots, 6$) and ζ is the exciting wave elevation. Hence, it comes that the RAO modulus expresses the relation between the motion amplitude and the wave elevation, while the phase relates to the lag between the exciting wave and the ship response. Figure 2.4 shows examples of RAOs calculated for the sway and yaw motions of a barge and a VLCC.

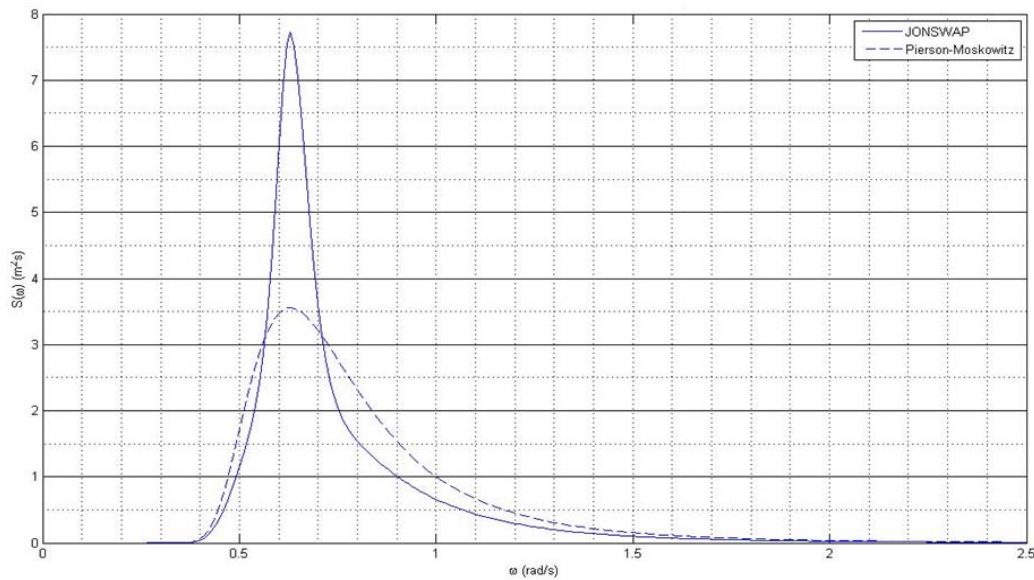


Figure 2.3 – Comparison between JONSWAP and Pierson-Moskowitz spectra.

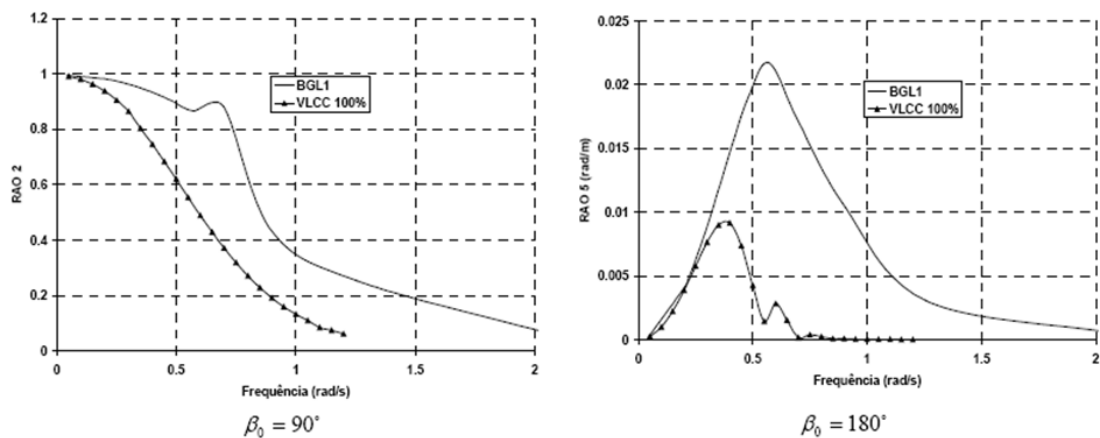


Figure 2.4 – RAOs for sway (left) and yaw (right) motions for a pipelaying barge and for a 100% loaded VLCC (TANNURI, 2002).

From the RAO and the wave spectrum it is possible to obtain the *motion spectrum* $S_{m,i}$, according to:

$$S_{m,i}(\omega) = |RAO_i(\omega)|^2 S_w(\omega) \quad (2.80)$$

Time-series of the wave motions are derived from (2.80) by means of inverse Fourier transform, as presented in (FALTINSEN, 1990):

$$y_i^{WF}(t) = \sum_{j=1}^n \sqrt{2S_{m,i}(\omega_j)\Delta\omega} \cos(\omega_j t + \phi_{RAO,j} + \phi_{aleat,j}) \quad (2.81)$$

where $\phi_{RAO,j} = \text{phase}(RAO(\omega_j))$ and $\phi_{rand,j}$ is a random value uniformly distributed in $[0, 2\pi]$. Figure 2.5 illustrates the process of transforming wave elevations to ship motions.

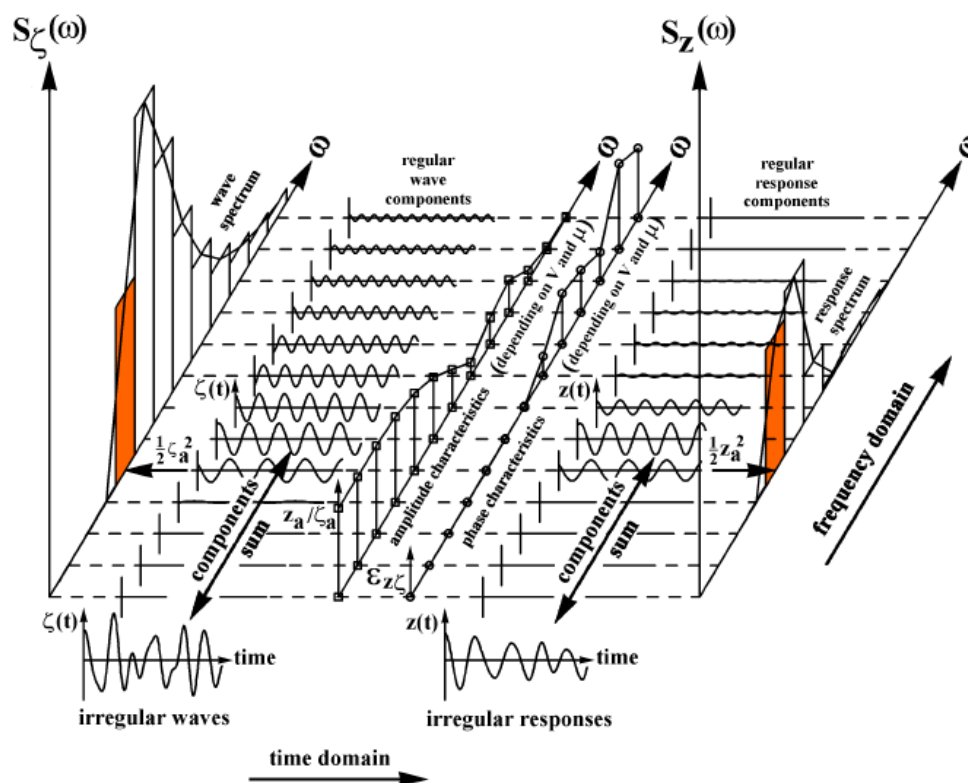


Figure 2.5 – Illustration of the process of transforming wave elevation in ship motions (JOURNÉE and PINKSTER, 2002).

Sometimes, the presented approach is not adequate to consider the motions induced by the first-order wave loads. As it will be shown further in the next section, problems involving interactions between bodies demand the wave

frequency forces to be considered in the equations of motions. In this case, RAOs are replaced by *force transfer functions* (FTF), defined as:

$$FTF_i(j\omega, \beta_r) = \frac{X_i^{WF}(j\omega, \beta_w)}{\zeta} \quad (2.82)$$

where X_i^{WF} is the wave-frequency induced force in DOF i . A procedure similar to that developed in (2.80) and (2.81) leads to the *load spectrum* $S_{\tau,i}(\omega)$ and time-domain realization $X_i^{WF}(t)$.

Both RAO and FTF data may be obtained from hydrodynamic solvers, as those presented in section 2.5.1.

2nd order wave loads

Important effects relate to the mean-drift forces and moments, since they do not have zero mean (like the first-order and slow-drift components) and therefore make the body to drift away from its position or path. Besides, the interaction of wave and current – known as *wave drift damping* – is an important source of resistance for the surge motion in higher sea states, and is considered as a component added to drift forces, proportional to the relative velocity of the hull and the water.

Mean-drift wave loads originate from the reflection of incident waves by the body. The change of direction of these waves leads to a huge variation in the linear momentum associated to the water particles. Mean drift forces comprise the reaction to this momentum switch. The amount of reflected waves depends on the body size relative to the wave length. In fact, the shorter are the waves when compared to the body, the more they are reflected – and thus, larger is the force. Oppositely, when the body size is comparable to the wave length, it tends to follow the surface elevation and, therefore, to reflect a smaller portion of the waves. Thus, in this case the forces are less significant.

Second-order wave loads also comprise the slow-drift forces and moments, whose frequencies are usually close to those of moored systems. Therefore, they may induce significant motions in structures like FPSOs and semi-submersible platforms, but are not important in the case of underway ships.

Calculation of mean-drift loads in irregular seas demands the use of drift coefficients $D(\omega, \beta_r)$, weighted by the wave spectrum. Such coefficients correspond to the mean-drift forces evaluated for a given frequency and incidence direction, normalized by the square of the wave amplitude. For the scope of this work, only loads in surge, sway and yaw are of importance. The generalized mean-drift forces are then calculated according to:

$$F_i^{MD}(t) = 2 \int_0^{\infty} S(\omega) D_i(\omega, \beta_r) d\omega, \quad i = 1, 2, 6 \quad (2.83)$$

Wave-drift damping evaluation will follow the procedure proposed in (ARANHA, 1996), where the effect is regarded through alteration of the drift coefficients. Let U_{curr} and α_r be the current velocity (relative to the hull) and relative incidence direction, respectively. The new coefficients are calculated according to:

$$\begin{aligned} D_{wdd,i}(\omega, \beta_r) = & D_i(\omega, \beta_r) \\ & + \frac{U_{curr}}{c} \{ \cos(\alpha_r) [b_{wi} \cos(\beta_r) + b_{ri} \sin(\beta_r)] \\ & + \sin(\alpha_r) [b_{wi} \sin(\beta_r) + b_{ri} \cos(\beta_r)] \} \end{aligned} \quad (2.84)$$

where the coefficients b_{ri} and b_{wi} are determined by:

$$b_{ri} = - \frac{2 \partial D_i(\omega, \beta_r)}{\partial \beta_r} \quad (2.85)$$

$$b_{wi} = 4 D_i(\omega, \beta_r) + \omega \frac{\partial D_i(\omega, \beta_r)}{\partial \omega} \quad (2.86)$$

Then, in order to consider the wave-drift damping effect the original drift coefficients $D_i(\omega, \beta_r)$ in (2.83) must be replaced by the new coefficients $D_{wdd,i}(\omega, \beta_r)$ calculated in (2.84). (TANNURI, 2002) shows that for a static VLCC under current of 1.2 m/s and 5.5 m height waves, with peak period of 11.4s, this correction may lead to a variation of 100% over the original value (i.e., without wave-drift damping). It is important to emphasize, however, that the formulation above was developed for a single body, and therefore is not adequate for application on the side-by-side case.

2.6.2 Wind

Wind plays an important role in ship dynamics, mainly when the weather conditions are severe and the vessel has a large portion of the hull and structures above the water level – which is the case for ballasted ships. Some relatively simple methods for wind loads calculation are available in the literature, involving coefficients obtained in model tests.

The model for tankers proposed in (OCIMF, 1977) is adopted in this work. Given the wind velocity U_{wind} and relative incidence direction γ_r , the forces and moments are calculated according to:

$$\begin{aligned} X_{wind} &= \frac{1}{2} \rho_{Air} A_T C_{X,wind}(\gamma_r) U_{wind}^2 \\ Y_{wind} &= \frac{1}{2} \rho_{Air} A_L C_{Y,wind}(\gamma_r) U_{wind}^2 \\ N_{wind} &= \frac{1}{2} \rho_{Air} A_L L C_{N,wind}(\gamma_r) U_{wind}^2 \end{aligned} \quad (2.87)$$

where ρ_{Air} is the density of the air, A_L and A_T are the lateral and transverse areas above water surface, L is the ship length and the coefficients $C_{X,wind}$, $C_{Y,wind}$ and $C_{N,wind}$ are obtained from the curves on Figures 2.6, 2.7 and 2.8.

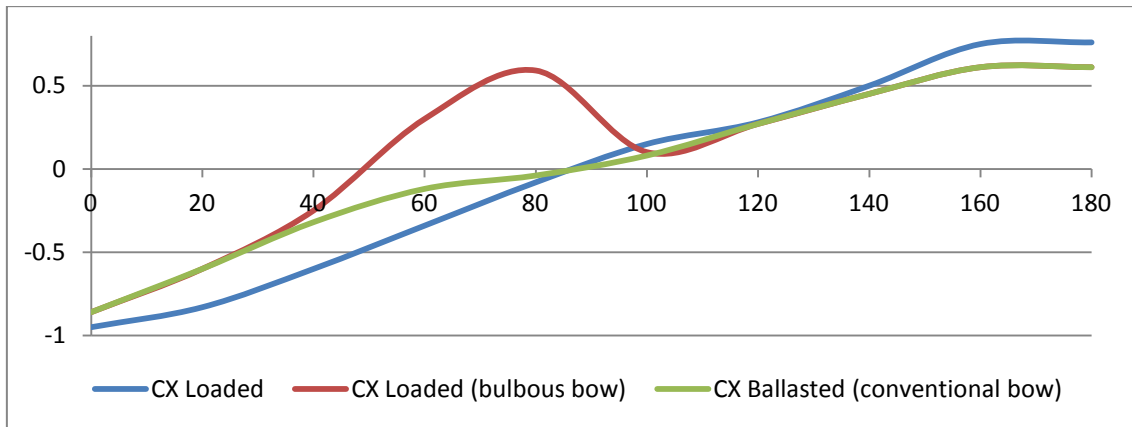


Figure 2.6 – Wind coefficients (surge) versus incidence direction.

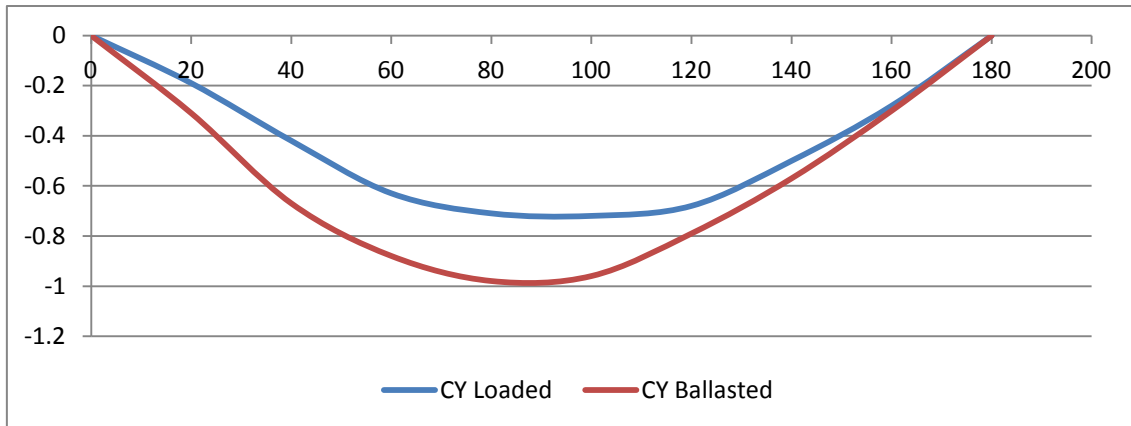


Figure 2.7 – Wind coefficients (sway) versus incidence direction.

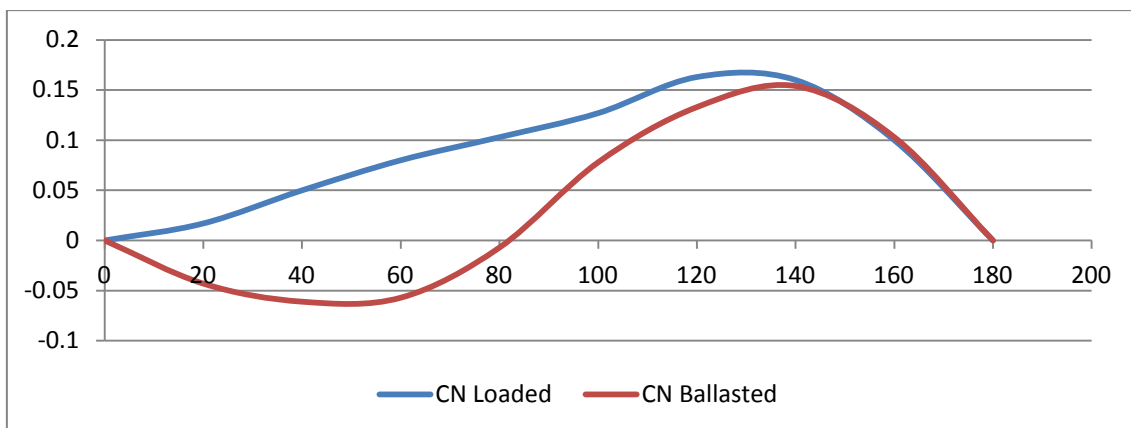


Figure 2.8 – Wind coefficients (yaw) versus incidence direction.

2.6.3 Current

Ocean water circulates due to gravity, wind friction and water density variation, generating ocean currents (FOSSSEN, 2002). This phenomenon induces a drift effect on floating structures, and should thus be considered in ship dynamics. When viscous coefficients are considered as presented on section 2.5.2, current loads are accounted for by simply considering the fluid velocity relative to the fluid in equation (2.68). A correction must be also performed on the calculation of radiation forces, as will be explained in section 2.7.1.

It may happen however, that viscous coefficients are not available or the current incidence exceeds the limit of acceptance for their utilization. In this case, adoption of a model may be more adequate for the formulation purposes, like the heuristic short-wing proposed by (LEITE, ARANHA, *et al.*, 1998). Given the water density ρ_{water} , the current velocity U_{curr} and relative incidence direction

α_r , the ship draft T_s and length between perpendiculars L_{pp} , the current loads may be calculated through the following expressions:

$$\begin{aligned} X_{curr} &= \frac{1}{2} \rho_{water} T_s L_{pp} C_{X,curr}(\alpha_r) U_{curr}^2 \\ Y_{curr} &= \frac{1}{2} \rho_{water} T_s L_{pp} C_{Y,curr}(\alpha_r) U_{curr}^2 \\ N_{curr} &= \frac{1}{2} \rho_{water} T_s L_{pp}^2 C_{N,curr}(\alpha_r) U_{curr}^2 \end{aligned} \quad (2.88)$$

where the coefficients $C_{X,curr}$, $C_{Y,curr}$ and $C_{N,curr}$ are calculated through:

$$\begin{aligned} C_{X,curr}(\alpha_r) &= \left(\frac{0.09375}{(\log_{10} R_e - 2)^2} \frac{S_s}{T_s L_{pp}} \right) \cos(\alpha_r) \\ &\quad + \frac{1}{8} \frac{\pi T_s}{L_{pp}} (\cos(3\alpha_r) - \cos(\alpha_r)) \\ C_{Y,curr}(\alpha_r) &= \left(C_Y - \frac{\pi T_s}{2 L_{pp}} \right) \sin(\alpha_r) |\sin(\alpha_r)| \\ &\quad + \frac{\pi T_s}{L_{pp}} \left(\frac{\sin^3(\alpha_r)}{2} + 1 + 0.4 \frac{C_B B_s}{T_s} \right) \sin(\alpha_r) |\cos(\alpha_r)| \\ C_{N,curr}(\alpha_r) &= -\frac{1}{L_{pp}} \left(C_Y - \frac{\pi T_s}{2 L_{pp}} \right) \sin(\alpha_r) |\sin(\alpha_r)| \\ &\quad - \frac{\pi T_s}{L_{pp}} \sin(\alpha_r) \cos(\alpha_r) \\ &\quad - \left(\frac{1 + |\cos(\alpha_r)|}{2} \right)^2 \frac{\pi T_s}{L_{pp}} \left(\frac{1}{2} - 2.4 \frac{T_s}{L_{pp}} \right) \sin(\alpha_r) |\cos(\alpha_r)| \end{aligned} \quad (2.89)$$

where R_e is the Reynolds number, S_s is the wetted hull area, C_B is the ship block coefficient and C_Y is a hydrodynamic coefficient.

The formulation above is only valid when the vessel rotational speed may be considered negligible. If, however, the ship is not static, an extended model including terms of damping due to yaw, as proposed in (SIMOS, TANNURI and ARANHA, 2001), must be chosen.

2.7 THE EQUATIONS OF MOTIONS

Ship dynamics are usually approached by two different ways, depending on the analysis objective. When the study focuses on course keeping, turning ability

and controllability – in calm water – it is referred to as *maneuvering*. If, on the other hand, one aims on the motions of a ship subjected to waves while moving with constant speed and heading, the analysis is known as *seakeeping*. Usually, the outcomes of both models are superposed for control systems design purposes.

Some situations, however, demand a combination of both maneuvering and seakeeping models (PEREZ, FOSSEN and SØRENSEN, 2004). Therefore, a unified model will be presented based on the formulation proposed in (FOSSEN, 2005). Such approach is necessary for the case, e.g., of two ships advancing in waves with interaction forces (e.g. mooring loads), where the division of the problem as stated above is inadequate.

2.7.1 Maneuvering

In the study of maneuvering, it is admitted that no first-order motions due to waves affect the ship. Therefore, the hydrodynamic coefficients correspond to the zero-frequency asymptotic values, i.e.:

$$\mathbf{A} = \mathbf{A}(0) = \mathbf{A}_0 \quad (2.90)$$

$$\mathbf{B} = \mathbf{B}(0) = \mathbf{0}_{6 \times 6} \quad (2.91)$$

Such that equation (2.73) reduces to:

$$\boldsymbol{\tau}_{hyd} = -\mathbf{A}_0 \dot{\mathbf{v}} - \mathbf{C}_{A_0}(\mathbf{v}) - \mathbf{D}(\mathbf{v})\mathbf{v} - \mathbf{G}\boldsymbol{\eta} \quad (2.92)$$

Replacing $\boldsymbol{\tau}_{hyd}$ in (2.58) by the above expression and then substituting the result in (2.56) yields:

$$(\mathbf{M}_{RB} + \mathbf{A}_0)\dot{\mathbf{v}} + [\mathbf{C}_{RB}(\mathbf{v}) + \mathbf{C}_{A_0}(\mathbf{v})]\mathbf{v} + \mathbf{D}(\mathbf{v})\mathbf{v} + \mathbf{G}\boldsymbol{\eta} = \boldsymbol{\tau}_{env} + \boldsymbol{\tau}_{con} \quad (2.93)$$

The velocity vector \mathbf{v} may not be directly integrated in time in order to get the positions and orientation angles. The coordinates transformation from b - to n -frame is performed through (2.41) and (2.42), in order to obtain the vector $\boldsymbol{\eta}$. Let $\mathbf{J}_b^n(\mathbf{v})$ be defined as:

$$\mathbf{J}_b^n(\boldsymbol{\eta}_2) = \begin{bmatrix} \mathbf{R}_b^n(\boldsymbol{\eta}_2) & \mathbf{0}_{3 \times 3} \\ \mathbf{0}_{3 \times 3} & \mathbf{T}_a(\boldsymbol{\eta}_2) \end{bmatrix} \quad (2.94)$$

Such that the relation below holds:

$$\dot{\boldsymbol{\eta}} = \mathbf{J}_b^n(\boldsymbol{\eta}_2)\mathbf{v} \quad (2.95)$$

The formulation above does not consider the effect of ocean currents. In fact, current makes the absolute velocity vector \mathbf{v} to be different from the velocity of the water relative to the hull. Let the *current velocity vector* \mathbf{v}_c , correspondent to the components of the current in the x_b and y_b axes, be defined as:

$$\mathbf{v}_c = \begin{bmatrix} U_{curr} \cos(\alpha_r) \\ U_{curr} \sin(\alpha_r) \\ 0 \\ 0 \\ 0 \\ 0 \end{bmatrix} \quad (2.96)$$

The *relative velocity vector* \mathbf{v}_r is obtained according to:

$$\mathbf{v}_r = \mathbf{v} - \mathbf{v}_c = \begin{bmatrix} u_r \\ v_r \\ z \\ p \\ q \\ r \end{bmatrix} \quad (2.97)$$

Radiation loads depend on the relative velocity, since they are related to the pressure exerted by the water in the ship hull. Therefore, $\boldsymbol{\tau}_{hyd}$ in (2.92) must be calculated in terms of \mathbf{v}_r , i.e. (SKJETNE, SMOGELI and FOSSEN, 2004):

$$\boldsymbol{\tau}_{hyd} = -\mathbf{A}_0 \dot{\mathbf{v}}_r - \mathbf{C}_{A_0}(\mathbf{v}_r) - \mathbf{D}(\mathbf{v}_r)\mathbf{v}_r - \mathbf{G}\boldsymbol{\eta} \quad (2.98)$$

From the definition of the first two elements u_c and v_c of vector \mathbf{v}_c (as defined in (2.98)), it may be easily deduced that their time-derivatives may be calculated as:

$$\begin{aligned} \dot{u}_c &= r v_c \\ \dot{v}_c &= -r u_c \end{aligned} \quad (2.99)$$

Such that $\dot{\mathbf{v}}_r$ is obtained through:

$$\dot{\mathbf{v}}_r = \dot{\mathbf{v}} - \dot{\mathbf{v}}_c = \begin{bmatrix} \dot{u} - r v_c \\ \dot{v} + r u_c \\ \dot{z} \\ \dot{p} \\ \dot{q} \\ \dot{r} \end{bmatrix} \quad (2.100)$$

Finally, equation (2.93) may be rewritten, considering the relative velocity effects:

$$\begin{aligned} \mathbf{M}_{RB}\dot{\mathbf{v}} + \mathbf{A}_0\dot{\mathbf{v}}_r + \mathbf{C}_{RB}(\mathbf{v})\mathbf{v} + \mathbf{C}_{A_0}(\mathbf{v}_r)\mathbf{v}_r + \mathbf{D}(\mathbf{v}_r)\mathbf{v}_r + \mathbf{G}\boldsymbol{\eta} \\ = \boldsymbol{\tau}_{env} + \boldsymbol{\tau}_{con} \end{aligned} \quad (2.101)$$

The equations of motion in 6 DOF are only meaningful when vertical (heave, roll and pitch) motions are to be considered in the model. This is usually the case when the relative motions of two bodies close from each other are to be analyzed. However, most of the cases in maneuvering concern only to horizontal (surge, sway and yaw) motions. Especially for marine control design, the equations of motions in 3 DOF are more likely to be utilized than the complete formulation presented above. Let the subscript h indicate the horizontal motions. The position $\boldsymbol{\eta}_h$ and velocity \mathbf{v}_h vectors are defined as:

$$\begin{aligned} \boldsymbol{\eta}_h &= [x, y, \psi]^T \\ \mathbf{v}_h &= [u, v, r]^T \end{aligned} \quad (2.102)$$

The matrices for 3 DOF are composed of the correspondent terms from \mathbf{M}_{RB} , \mathbf{A}_0 , $\mathbf{C}_{RB}(\mathbf{v})$, $\mathbf{C}_{A_0}(\mathbf{v}_r)$, $\mathbf{D}(\mathbf{v}_r)$ and \mathbf{G} .

2.7.2 Seakeeping

Following the same approach used for maneuvering, seakeeping equations of motion are formulated departing from the rigid-body dynamics results of section 2.4.2. Once only the effect of first-order wave loads is to be considered, the hydrodynamic (plus hydrostatic) term $\delta\boldsymbol{\tau}_{hyd}$ depends only on the radiation and restoration forces:

$$\delta\boldsymbol{\tau}_{hyd} = -\mathbf{A}_s(\omega_e)\ddot{\boldsymbol{\xi}} - \mathbf{B}_s(\omega_e)\dot{\boldsymbol{\xi}} - \mathbf{G}_s\boldsymbol{\xi} \quad (2.103)$$

where the subscript s states that the matrices are computed for the seakeeping coordinate system. It is worth to point out the dependence on the encounter frequency for both the added mass and potential damping. From (2.59), (2.61) and (2.103) it comes that:

$$[\mathbf{M}_{RB,s} + \mathbf{A}_s(\omega_e)]\ddot{\boldsymbol{\xi}} + \mathbf{B}_s(\omega_e)\dot{\boldsymbol{\xi}} + \mathbf{G}_s\boldsymbol{\xi} = \delta\boldsymbol{\tau}_{WF} + \delta\boldsymbol{\tau}_{con} \quad (2.104)$$

The term $\delta\boldsymbol{\tau}_{WF}$ may be obtained from the wave elevation and the FTF, as explained in section 2.6. Hydrodynamic solvers calculate both RAOs and FTFs from equation (2.104), disregarding the control term $\delta\boldsymbol{\tau}_{con}$. For a discrete range of encounter frequencies ω_e , $\delta\boldsymbol{\tau}_{WF}$ is admitted as a sinusoidal wave excitation, and from the calculated response it is possible to obtain the desired transfer function.

The formulation above is developed for the s -frame. To derive the same results for the b -frame, (2.36) and (2.37) are substituted in (2.104) and both sides of the resultant equation are multiplied by \mathbf{J}_s^T :

$$\begin{aligned} \mathbf{J}_s^T[\mathbf{M}_{RB,s} + \mathbf{A}_s(\omega_e)](\mathbf{J}_s\delta\dot{\mathbf{v}} + U\mathbf{L}_s\delta\mathbf{v}) + \mathbf{J}_s^T\mathbf{B}_s(\omega_e)\left(\mathbf{J}_s\delta\mathbf{v} - \frac{U}{\omega_e^2}\mathbf{L}_s\delta\dot{\mathbf{v}}\right) \\ + \mathbf{J}_s^T\mathbf{G}_s\xi = \mathbf{J}_s^T(\delta\boldsymbol{\tau}_{WF} + \delta\boldsymbol{\tau}_{con}) \end{aligned} \quad (2.105)$$

Using relation (2.60) and making the following substitutions:

$$\begin{aligned} \tilde{\mathbf{A}}(\omega_e) &= \mathbf{J}_s^T\mathbf{A}_s(\omega_e)\mathbf{J}_s - \frac{U}{\omega_e^2}\mathbf{J}_s^T\mathbf{B}_s(\omega_e)\mathbf{L}_s \\ \tilde{\mathbf{D}}(\omega_e) &= \mathbf{J}_s^T\mathbf{B}_s(\omega_e)\mathbf{J}_s \\ \mathbf{C}_{RB} &= U\mathbf{J}_s^T\mathbf{M}_{RB,s}\mathbf{L}_s \\ \tilde{\mathbf{C}}_A(\omega_e) &= U\mathbf{J}_s^T\mathbf{A}_s(\omega_e)\mathbf{L}_s \\ \tilde{\mathbf{N}}(\omega_e) &= \tilde{\mathbf{C}}_A(\omega_e) + \tilde{\mathbf{D}}(\omega_e) \\ \mathbf{G} &= \mathbf{J}_s^T\mathbf{G}_s \\ \boldsymbol{\tau}_{WF} &= \mathbf{J}_s^T\delta\boldsymbol{\tau}_{WF} \\ \boldsymbol{\tau}_{con} - \bar{\boldsymbol{\tau}}_{con} &= \mathbf{J}_s^T\delta\boldsymbol{\tau}_{con} \end{aligned} \quad (2.106)$$

where $\bar{\boldsymbol{\tau}}_{con}$ is the necessary control load for the ship to advance with velocity U , it finally comes (FOSSEN, 2005):

$$[\mathbf{M}_{RB} + \tilde{\mathbf{A}}(\omega_e)]\delta\dot{\mathbf{v}} + \mathbf{C}_{RB}\delta\mathbf{v} + \tilde{\mathbf{N}}(\omega_e)\delta\mathbf{v} + \mathbf{G}\xi = \boldsymbol{\tau}_{WF} + (\boldsymbol{\tau}_{con} - \bar{\boldsymbol{\tau}}_{con}) \quad (2.107)$$

Equations of motions for pure maneuvering and seakeeping have already been presented. Now, a unified model for both approaches will be presented, based on time-domain transformation of equation (2.107).

2.7.3 Unified model for maneuvering and seakeeping

As stated in the beginning of this section, the low-frequency (LF) and wave-frequency (WF) components outputted by the maneuvering and seakeeping models, respectively, are usually superposed in the design of control systems for marine vehicles. The scheme on Figure 2.9 illustrates this principle.

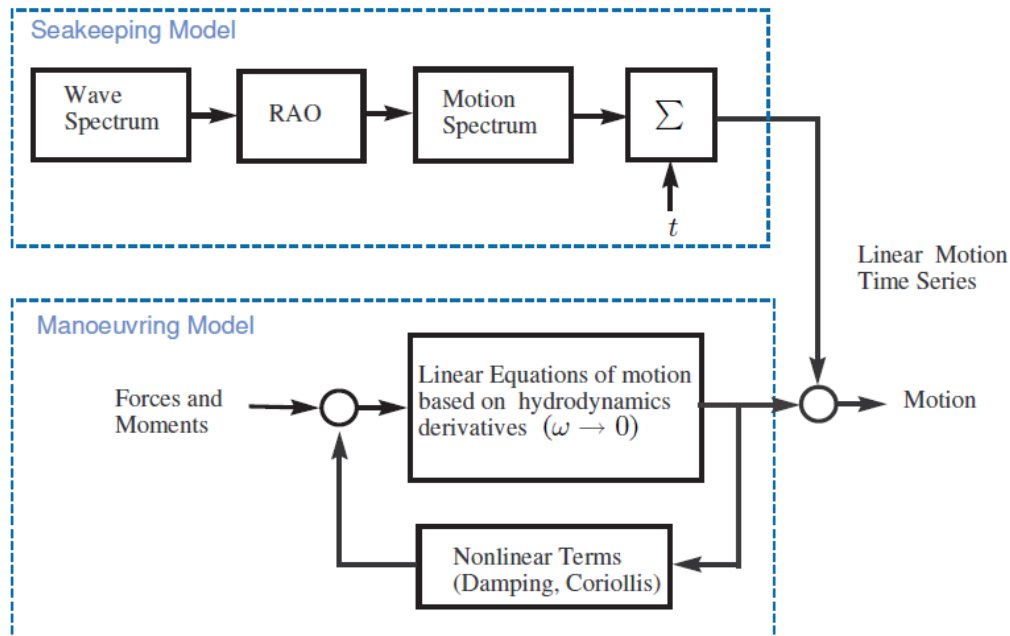


Figure 2.9 – Usual approach of superposing LF and WF motions (PEREZ, FOSSEN and SØRENSEN, 2004).

Although practical and acceptable for most design purposes, this approach may be inadequate in some situations. Multibody operations with interactions between bodies involve energy exchanges among the systems, and this effect is not reproduced by the LF+WF method (PEREZ, FOSSEN and SØRENSEN, 2004). A pertinent example is the case of two ships moored together and advancing in waves. Each of them is excited by waves, generating wave-frequency tensions on the mooring lines. Then, WF motions are not induced only by waves, but also through the lines, and thus they cannot be described by time-domain realization of the RAO based motion spectrum.

Another shortcoming of the superposition method comes from the use of zero-frequency added mass and damping coefficients in the maneuvering model. This practice neglects fluid memory effects, leading to unmodeled dynamics which may affect the control performance for rough sea states. Finally, the procedure of just summing LF and WF signals fails in physical rigor. First-order wave forces and moments should be considered in the equations of motions, as any

other load acting on the body. In the example above, the WF forces for each ship would act together with those (also with WF) induced by the ropes, allowing the real motion to be reproduced.

However, it is not a trivial task to consider wave-frequency excitation forces in time-domain equations of motions. In fact, from the definition of radiation forces in 2.5.1 it arises that both added mass and potential damping coefficients must be regarded as frequency-dependent if the body is forced to oscillate by a harmonic excitation. Unless the input has a perfectly defined frequency – which is not the case for irregular (realistic) seas –, the equations of motion would not have any mathematical meaning, for they would depend both on time and frequency.

This obstacle may be overcome by the approach proposed in (CUMMINS, 1962). It consists in regarding some components of ship motions as impulse-response functions. Therefore, the velocity potential is described as a sum of two components: one actuating during the excitation occurrence, and other for the subsequent effects which arise from this excitation. Departing from Cummins' results, the following expression for $\delta\tau_{rad}$ is obtained:

$$\delta\tau_{rad} = -\mathbf{A}'_s \ddot{\xi} - \int_{-\infty}^t \mathbf{K}_s(t-t') \dot{\xi}(t') dt' - \mathbf{G}'_s \xi \quad (2.108)$$

Where $\mathbf{K}_s(t)$ is a *matrix of retardation functions*, whose deduction will be presented bellow. Substituting in (2.59), the so-called *Cummins Equation* is obtained:

$$[\mathbf{M}_{RB,S} + \mathbf{A}'_s] \ddot{\xi} + \int_{-\infty}^t \mathbf{K}_s(t-t') \dot{\xi}(t') dt' + \mathbf{G}'_s \xi = \delta\tau_{WF} \quad (2.109)$$

where the control forces vector $\delta\tau_{con}$ is disregarded for the formulation. Let the body oscillations ξ have the form:

$$\xi = \cos(\omega t) \mathbf{I}_{6 \times 6} \quad (2.110)$$

Substituting in (2.109) yields:

$$\begin{aligned}
& -\omega^2 \left\{ [\mathbf{M}_{RB,S} + \mathbf{A}'_s] \cos(\omega t) - \frac{1}{\omega} \int_0^\infty \mathbf{K}_s(t') \sin(\omega t') dt' \right\} \cos(\omega t) \\
& \quad - \omega \left\{ \int_0^\infty \mathbf{K}_s(t') \cos(\omega t') dt' \right\} \sin(\omega t) \\
& \quad + \mathbf{G}'_s \cos(\omega t) = \delta \boldsymbol{\tau}_{WF}
\end{aligned} \tag{2.111}$$

The same procedure is now applied for equation (2.106)¹³, leading to:

$$\begin{aligned}
& -\omega^2 [\mathbf{M}_{RB,S} + \mathbf{A}_s(\omega)] \cos(\omega t) - \omega \mathbf{B}_s(\omega) \sin(\omega t) \\
& \quad + \mathbf{G}_s \cos(\omega t) = \delta \boldsymbol{\tau}_{WF}
\end{aligned} \tag{2.112}$$

Comparing the terms of equations (2.111) and (2.112), it is noticed that the following relations hold (OGILVIE, 1964):

$$\mathbf{A}_s(\omega) = \mathbf{A}'_s - \frac{1}{\omega} \int_0^\infty \mathbf{K}_s(t') \sin(\omega t') dt' \tag{2.113}$$

$$\mathbf{B}_s(\omega) = \int_0^\infty \mathbf{K}_s(t') \cos(\omega t') dt' \tag{2.114}$$

$$\mathbf{G}_s = \mathbf{G}'_s \tag{2.115}$$

Since (2.113) must be valid for all values of ω , the value of \mathbf{A}'_s may be obtained by making $\omega = \infty$:

$$\mathbf{A}'_s = \mathbf{A}_s(\infty) \tag{2.116}$$

The matrix of retardation functions $\mathbf{K}_s(t)$ comes from inverse Fourier transform of (2.114):

$$\mathbf{K}_s(t) = \frac{2}{\pi} \int_0^\infty \mathbf{B}_s(\omega) \cos(\omega t) d\omega \tag{2.117}$$

Equation (2.109) may be rewritten in terms of the above relations, leading to:

$$[\mathbf{M}_{RB,S} + \mathbf{A}_s(\infty)] \ddot{\boldsymbol{\xi}} + \int_{-\infty}^t \mathbf{K}_s(t-t') \dot{\boldsymbol{\xi}}(t') dt' + \mathbf{G}_s \boldsymbol{\xi} = \delta \boldsymbol{\tau}_{WF} \tag{2.118}$$

These results may be applied to the *b*-frame formulation (2.107), leading to:

¹³ The subscript *e* was suppressed for the general formulation development.

$$\begin{aligned}
& [\mathbf{M}_{RB} + \tilde{\mathbf{A}}(\infty)]\delta\dot{\mathbf{v}} + \mathbf{C}_{RB}\delta\mathbf{v} + \tilde{\mathbf{N}}(\infty)\delta\mathbf{v} + \int_{-\infty}^t \mathbf{K}_s(t-t')\delta\mathbf{v}(t')dt' \\
& + \mathbf{G}\xi = \boldsymbol{\tau}_{WF} + (\boldsymbol{\tau}_{con} - \bar{\boldsymbol{\tau}}_{con})
\end{aligned} \tag{2.119}$$

Finally, using the following definitions:

$$\begin{aligned}
\mathbf{M} &= \mathbf{M}_{RB} + \tilde{\mathbf{A}}(\infty) \\
\mathbf{D} &= \tilde{\mathbf{N}}(\infty) = \mathbf{C}_A(\mathbf{v}) \\
\boldsymbol{\mu} &= \int_{-\infty}^t \mathbf{K}_s(t-t')\delta\mathbf{v}(t')dt'
\end{aligned} \tag{2.120}$$

And substitutions:

$$\begin{aligned}
\delta\mathbf{v} &= \mathbf{v} - \bar{\mathbf{v}} \\
\bar{\boldsymbol{\tau}} &= \mathbf{C}_{RB}\bar{\mathbf{v}} + \mathbf{D}\bar{\mathbf{v}} \\
\mathbf{G}\xi &= \mathbf{G}\eta
\end{aligned} \tag{2.121}$$

The complete model is then written as:

$$\begin{aligned}
\mathbf{M}\dot{\mathbf{v}} + [\mathbf{C}_{RB} + \mathbf{C}_A(\mathbf{v})]\mathbf{v} + \boldsymbol{\mu} + \mathbf{G}\eta &= \boldsymbol{\tau}_{WF} + \boldsymbol{\tau}_{con} \\
\dot{\boldsymbol{\eta}} &= \mathbf{J}_b^n(\boldsymbol{\eta}_2)\mathbf{v}
\end{aligned} \tag{2.122}$$

where (2.95) was repeated for the sake of clearness. The unified model for maneuvering and seakeeping is depicted on Figure 2.10.

The convolution term in (2.120) is inconvenient for computational and control design purposes. Therefore, it is advantageous to approximate it by a set of state space equations, like proposed in (HJUSTAD, KRISTIANSEN and EGELAND, 2004):

$$\dot{\boldsymbol{\chi}} = \mathbf{A}_r\boldsymbol{\chi} + \mathbf{B}_r\delta\mathbf{v} \tag{2.123}$$

$$\boldsymbol{\mu} = \mathbf{C}_r\boldsymbol{\chi} + \mathbf{D}_r\delta\mathbf{v} \tag{2.124}$$

where the matrices \mathbf{A}_r , \mathbf{B}_r , \mathbf{C}_r and \mathbf{D}_r are obtained through identification methods. A survey on such methods is given in (TAGHIPUR, PEREZ and MOAN, 2008), where approaches are presented based on different sets of input data. Basically, the convolution term is represented by a parametric model

structure and a fitting criterion, and system identification is used in order to estimate the parameters.

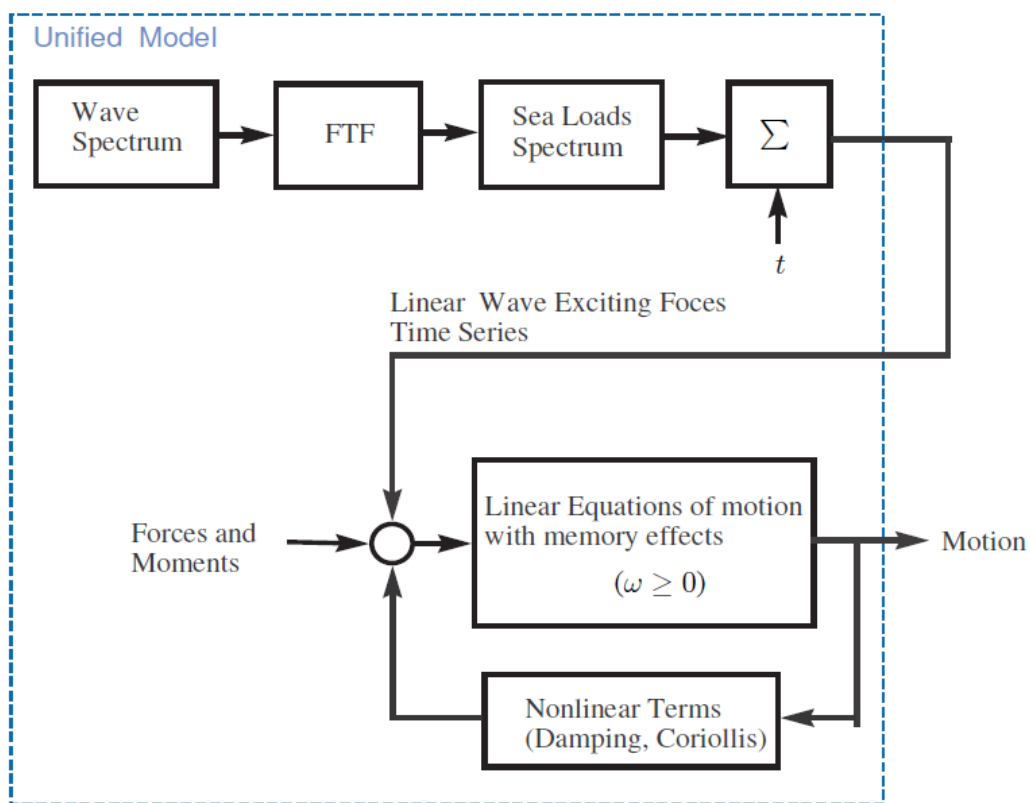


Figure 2.10 – Unified model for maneuvering and seakeeping (PEREZ, FOSSEN and Sørensen, 2004).

3. CONTROL

Control systems are broadly present in marine vehicles. Merchant ships are usually provided with autopilots, and dynamic positioning (DP) systems are common in tugboats, supply vessels and shuttle tankers. Many other technologies involve control applications in marine systems, including e.g. rudder-roll stabilization, active antiroll U-tube tanks and hydrofoil stabilizers.

The available literature introduces different strategies for control systems design, and some of them are particularly popular in marine vehicles. The traditional *PID controller* is undoubtedly a standard approach for most applications, but more sophisticated solutions have been developed in the last decades. One of them is the relatively recent *integrator backstepping*, a nonlinear strategy based on Lyapunov's method for stability.

Another important issue in marine control systems is *state estimation*. Acceptable performance of the actuators demands that only the low-frequency component of the signal is fed to the controllers. A *state observer* is a dynamic system that aims to reproduce unmeasured states of an observable system. An observer may separately estimate the low- and wave-frequency components of a ship motions, feeding only the first of them to the controller.

Sometimes, the number of actuators available on a ship is not enough to perform the desired control objective. An example is the problem of path-following, which comprises a ship having to keep a given trajectory with some specified speed. Once a merchant vessel is usually provided with a single screw and rudder set, it is only able to control the surge and yaw motions. One approach to overcome the lack of controllability of lateral motions is the so-called *line-of-sight* strategy, a guidance system consisting on a reference generator for the yaw controller that orients the ship such that it performs the specified path on the horizontal plane.

3.1 CONTROL APPROACHES

In spite of the intrinsic nonlinearity of ship dynamics, linear approaches still comprise a very popular strategy for marine control systems. In fact, last generation solutions developed in academia usually face some resistance from

industry, since the simple and cheap traditional controllers cope well with their necessities for most cases (BREIVIK, 2010).

In this work, the backstepping strategy is used for the shuttle tanker autopilot controller (in convoy configuration). For the autopilot of the VLCC, a PID controller is adopted.

3.1.1 PID controller

The *Proportional-Integral-Derivative* controller is popular in industry due to both its robustness and operational simplicity. Its performance depends on adjustment of three parameters, and its transfer function is given by:

$$G_{PID}(s) = K_P + \frac{K_I}{s} + K_D s \quad (3.1)$$

Where the K_P , K_I and K_D are the proportional, integral and derivative gains, respectively. In time-domain, the PID controller action is formulated as:

$$\tau^{PID}(t) = -K_P \tilde{x}(t) - K_D \dot{\tilde{x}}(t) - K_I \int_0^t \tilde{x}(t') dt' \quad (3.2)$$

with the *tracking error* $\tilde{x}(t)$ given by:

$$\tilde{x}(t) = x(t) - x_{ref}(t) \quad (3.3)$$

where $x_{ref}(t)$ is the reference (setpoint) signal. Figure 3.1 depicts the structure of a PID controller.

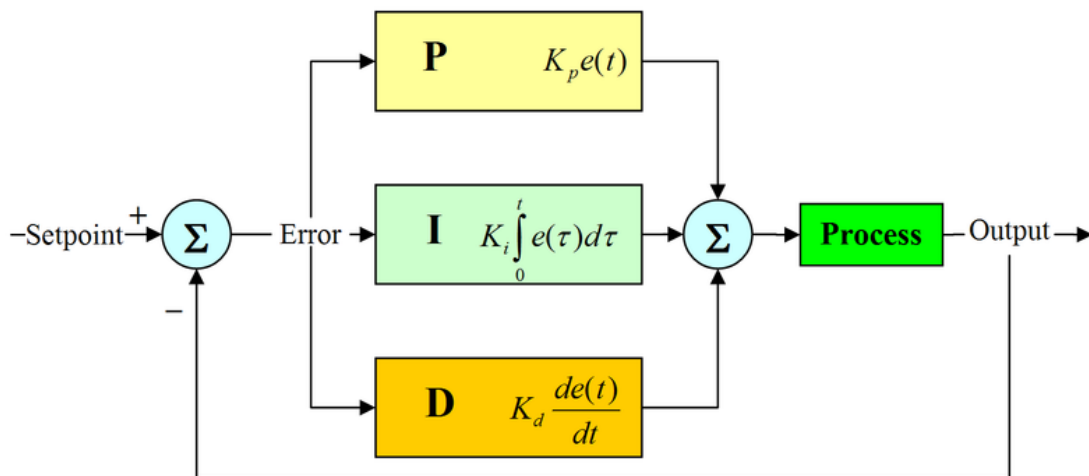


Figure 3.1 – PID controller structure.

When a PID controller is used in autopilot design, care must be taken with the so-called *integrator windup* phenomenon. When the actuator – in this case, the rudder – saturates, the error continues to be integrated so that the integrator in (3.2) “winds up”, that is, assumes a very large value (ÅSTRÖM and HÄGGLUND, 1995). This process is illustrated in Figure 3.2. The high change in the setpoint leads the actuator to saturation, as it may be noticed in the second graphic. However, even after the system output reaches the reference the actuator still keeps saturated due to the accumulated integral parcel, represented in the curve on the bottom of the figure.

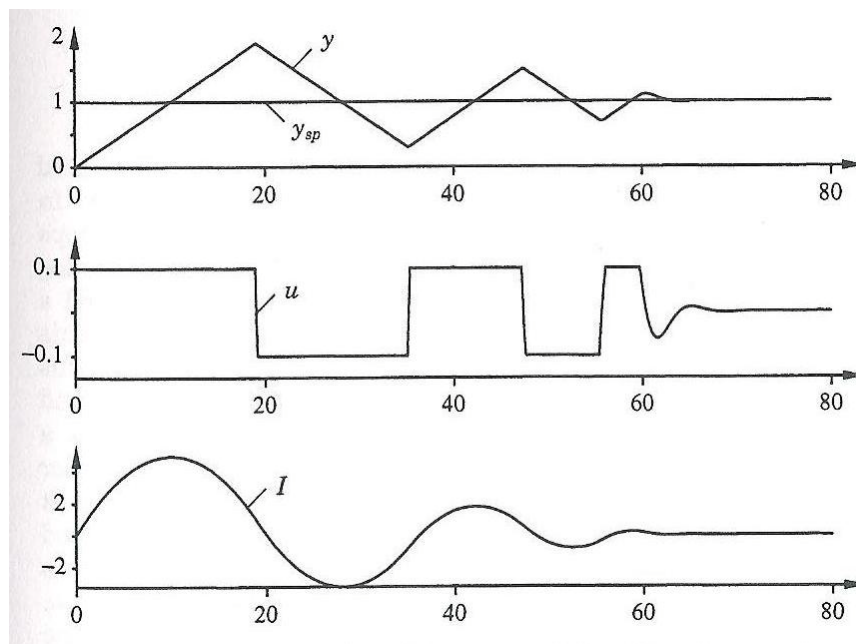


Figure 3.2 – Integrator windup phenomenon, where y is the process output, y_{sd} is the setpoint, u is the control signal and I is the integral part. Extracted from (ÅSTRÖM and HÄGGLUND, 1995).

Since the windup phenomenon may lead the system to destabilization, it is worth to avoid it by implementing some algorithms together with the controller. An effective and relatively simple method is to establish a bound to the integral parcel, by stopping the integration process when it reaches a predefined value.

3.1.2 Backstepping controller

Backstepping is a nonlinear strategy for control systems design through a recursive procedure based on the Lyapunov direct method for stability. An expedient feature is the possibility of taking advantage of some nonlinearities of the system, instead of just cancelling them as in *feedback linearization*

approach, for instance. Therefore, dependence of the control laws on unknown parameters of the system is diminished, together with the total amount of energy required for the controlling action. Derivation of backstepping formulation demands some insight on Lyapunov's theory for determining the stability of a system, as presented on Appendix A.

The integral backstepping method

Backstepping is a recursive technique for nonlinear control systems design, as presented in (KRSTIC, KANELLAPOULOS and KOKOTOVIC, 1995). When the system input is connected to a series of integrators, the method is called *integral backstepping*. Let a nonlinear system be defined, for example, by the following equations (FOSSEN and STRAND, 1998):

$$\dot{x}_1 = f(x_1) + x_2 \quad (3.4)$$

$$\dot{x}_2 = u \quad (3.5)$$

$$y = x_1 \quad (3.6)$$

where $x_1, x_2, y, u \in \mathbb{R}$ and the nonlinear function $f(x_1)$ has the following form:

$$f(x_1) = -a_0x_1 - a_1x_1^2 - a_2|x_1|x_1 \quad (3.7)$$

Considering the objective of the control as to lead $y(t) \rightarrow 0$ for $t \rightarrow \infty$, it comes that the desired result is to render $(x_1, x_2) = (0, -f(0))$ as an GAS equilibrium point. The recursive design is divided into two steps, as the system (3.4)-(3.5) involves two states. First, the following change of variables is introduced:

$$\mathbf{z} = \boldsymbol{\phi}(\mathbf{x}) \quad (3.8)$$

where $\mathbf{z} = [z_1, z_2]^T$, $\mathbf{x} = [x_1, x_2]^T$ and $\boldsymbol{\phi}$ is a *diffeomorphic function*. For the first step, the above transformation is defined for z_1 :

$$z_1 = x_1 \quad (3.9)$$

Then, regarding the state x_2 as a *virtual control* input:

$$x_2 \triangleq \alpha_1 + z_2 \quad (3.10)$$

where α_1 is called *stabilizing function*, it comes from (3.4), (3.9) and (3.10) that:

$$\dot{z}_1 = f(x_1) + \alpha_1 + z_2 \quad (3.11)$$

The choice of an expression for α_1 is a matter of analyzing $f(x_1)$ so that the “good” nonlinearities, i.e., those that help keeping the system stable should be kept. Meanwhile the “bad” ones (those that destabilize the system) are to be dominated. Thus, a suitable choice for α_1 could be:

$$\alpha_1 = -[k_1 + \kappa_1 z_1^2]z_1 \quad (3.12)$$

with $k_1, \kappa_1 > 0$, so that the “bad” nonlinearity $a_1 x_1^2$ of $f(x_1)$ is dominated (since the introduced term is proportional to x^3), while the “good” terms $a_0 x_1$ and $a_2 |x_1| x_1$ are not controlled, for they are useful to attain stability to the system. Substituting in (3.11):

$$\dot{z}_1 = -(a_0 + a_2 |z_1| + k_1)z_1 - a_1 z_1^2 - \kappa_1 z_1^3 + z_2 \quad (3.13)$$

Considering the Lyapunov candidate function:

$$V_1 = \frac{1}{2} z_1^2 \quad (3.14)$$

Time differentiation of V_1 yields:

$$\dot{V}_1 = \frac{\partial V_1}{\partial z_1} \dot{z}_1 = -(a_0 + a_2 |z_1| + k_1)z_1^2 - a_1 z_1^3 - \kappa_1 z_1^4 + z_1 z_2 \quad (3.15)$$

The second step departs from time derivation of z_2 . From (3.10) it comes that:

$$\dot{z}_2 = \dot{x}_2 - \dot{\alpha}_1 = u - \dot{\alpha}_1 \quad (3.16)$$

Let a Lyapunov candidate V_2 be defined as:

$$V_2 = V_1 + \frac{1}{2} z_2^2 \quad (3.17)$$

Proceeding with the same approach as for V_1 :

$$\dot{V}_2 = -(a_0 + a_2 |z_1| + k_1)z_1^2 - a_1 z_1^3 - \kappa_1 z_1^4 + z_2(z_1 + u - \dot{\alpha}_1) \quad (3.18)$$

Choosing the control law u as:

$$u = \dot{\alpha}_1 - k_2 z_2 - z_1 \quad (3.19)$$

Substitution in (3.18) yields:

$$\dot{V}_2 = -(a_0 + a_2|z_1| + k_1)z_1^2 - a_1 z_1^3 - \kappa_1 z_1^4 - k_2 z_2^2 \quad (3.20)$$

which can be rewritten as:

$$\begin{aligned} \dot{V}_2 &= -\left(\frac{a_1}{2\sqrt{\kappa_1}}z_1 + \sqrt{\kappa_1}z_1^2\right)^2 - \frac{a_1^2}{4\kappa_1}z_1^2 - (a_0 + a_2|z_1| + k_1)z_1^2 - k_2 z_2^2 \\ &\leq -\left(a_0 + k_1 - \frac{a_1^2}{4\kappa_1}\right)z_1^2 - k_2 z_2^2 \end{aligned} \quad (3.21)$$

Finally, rendering $\dot{V}_2 < 0$ is a matter of choosing the controller gains according to the following relations:

$$\begin{aligned} \kappa_1 &> 0 \\ k_1 &> \frac{a_1^2}{4\kappa_1} - a_0 \\ k_2 &> 0 \end{aligned} \quad (3.22)$$

Such that the control design is complete. This approach will be particularized for application in a ship autopilot on Chapter 5.

3.2 NONLINEAR PASSIVE OBSERVER

State estimation is performed by an approximate mathematical model of a real system, corrected by the difference between measurement and estimates multiplied by appropriate gains. Such gains must be calculated in a way to make the observer state to converge to the real system state.

A nonlinear observer comprises a model with nonlinear equations. This is attractive for inherently nonlinear systems, like marine vehicles, since it is not necessary to linearize the equations around a discretized envelope of heading angles, in opposition to the procedure involving a linear observer (e.g. Kalman Filter) (FOSSSEN, 2002).

The adopted formulation was based in (FOSSSEN and STRAND, 1999) and (ZAKARTCHOUK JR, 2010), and applies passivity theory in order to assure that the estimates converge to the real system state. That is, the observer gains are

determined as to assign passivity to the error dynamics, ensuring that they asymptotically converge to zero.

Such references, however, are developed for dynamic positioning (DP) applications, such that their formulation disregards the Coriolis and centripetal matrix under assumption of low velocities. Here, the system to be observed is an underway ship, such that the surge velocity cannot be disregarded. Proper linearization of that matrix around the surge service velocity ensures that the necessary assumptions for the observer functionality are fulfilled, though.

3.2.1 Observer model

The maneuvering model in 3 DOF (section 2.7.1) may be simplified according to:

$$\begin{aligned} \mathbf{M}\dot{\mathbf{v}} + \mathbf{N}\mathbf{v} &= \boldsymbol{\tau}_{env} + \boldsymbol{\tau}_{con} \\ \dot{\boldsymbol{\eta}} &= \mathbf{J}(\boldsymbol{\eta})\mathbf{v} \end{aligned} \quad (3.23)$$

where the influence of the current speed in radiation forces was neglected and the damping matrix was admitted as being purely linear. The inertia matrix \mathbf{M} is considered to be strictly positive and symmetric¹⁴, that is, $\mathbf{M} = \mathbf{M}^T > 0$ and is composed by both rigid-body and added-mass components, i.e., $\mathbf{M} = (\mathbf{M}_{RB} + \mathbf{A}_0)$, while \mathbf{N} is the sum of the linear damping terms and the Coriolis and centripetal matrix linearized around $\mathbf{v}_h = [U_s \ 0 \ 0]^T$, U_s being the service speed:

$$\mathbf{N} = \mathbf{C} + \mathbf{D} \quad (3.24)$$

$$\mathbf{C} = \begin{bmatrix} 0 & 0 & 0 \\ 0 & 0 & (m - X_{\dot{u}})U_s \\ 0 & -(m - X_{\dot{u}})U_s & 0 \end{bmatrix} \quad (3.25)$$

$$\mathbf{D} = - \begin{bmatrix} X_u & 0 & 0 \\ 0 & Y_n & Y_r \\ 0 & N_v & N_r \end{bmatrix} \quad (3.26)$$

with the damping coefficients as defined in section 2.5.2. It is important to observe that $\mathbf{C} = -\mathbf{C}^T$, such that:

¹⁴ The added mass matrix is actually non-symmetric for advancing ships, but since surge speed is moderate it will be admitted as symmetric in this formulation.

$$(\mathbf{N} + \mathbf{N}^T) = (\mathbf{D} + \mathbf{C} + \mathbf{D}^T + \mathbf{C}^T) = (\mathbf{D} + \mathbf{D}^T) \quad (3.27)$$

This result is mandatory for the extension of the formulation in (FOSSEN and STRAND, 1999) to the case of an underway ship.

The vector of environmental loads $\boldsymbol{\tau}_{env}$ is the body-fixed projection of a *bias forces and moments* vector $\mathbf{b} \in \mathbb{R}^3$, admitted as a slowly varying Gaussian process, that is:

$$\boldsymbol{\tau}_{env} = \mathbf{J}^T(\boldsymbol{\eta})\mathbf{b} \quad (3.28)$$

$$\dot{\mathbf{b}} = -\mathbf{T}^{-1}\mathbf{b} + \boldsymbol{\Psi}\mathbf{n} \quad (3.29)$$

with $\mathbf{T} \in \mathbb{R}^{3 \times 3}$ being a diagonal matrix with time constants, $\boldsymbol{\Psi} \in \mathbb{R}^{3 \times 3}$ a matrix of gains and $\mathbf{n} \in \mathbb{R}^3$ a vector of zero-mean white Gaussian noise.

Finally, the model for WF-motions arises from an approximation for the ship response power spectrum P^i :

$$P^i = |h_{wf}^i(j\omega)|^2 \quad (3.30)$$

$i = 1, 2, 3$, with the transfer function $h_{wf}^i(s)$ given by (FOSSEN, 2002):

$$h_{wf}^i(s) = \frac{\sigma_i s}{s^2 + 2\zeta_i \omega_{0i} s + \omega_{0i}^2} \quad (3.31)$$

ω_{0i} and ζ_i being the modal frequency and damping for the approximated spectrum, respectively, and σ_i a parameter for adjustment of the approximation. Representing (3.31) in a state-space model one gets:

$$\begin{aligned} \dot{\boldsymbol{\xi}} &= \boldsymbol{\Omega}\boldsymbol{\xi} + \boldsymbol{\Sigma}\mathbf{w} \\ \boldsymbol{\eta}_{wf} &= \boldsymbol{\Gamma}\boldsymbol{\xi} \end{aligned} \quad (3.32)$$

where $\boldsymbol{\xi} \in \mathbb{R}^6$ is the state vector, $\boldsymbol{\eta}_{wf} \in \mathbb{R}^3$ is the output vector with the WF-motions, $\mathbf{w} \in \mathbb{R}^3$ is a vector of zero-mean white gaussian noise and the matrices $\boldsymbol{\Omega}$, $\boldsymbol{\Sigma}$ and $\boldsymbol{\Gamma}$ are defined as following:

$$\boldsymbol{\Omega} = \begin{bmatrix} \mathbf{0}_{3 \times 3} & \mathbf{I}_{3 \times 3} \\ \boldsymbol{\Omega}_{21} & \boldsymbol{\Omega}_{22} \end{bmatrix} \quad (3.33)$$

$$\Sigma = \begin{bmatrix} \mathbf{0}_{3 \times 3} \\ \Sigma_2 \end{bmatrix} \quad (3.34)$$

$$\Gamma = [\mathbf{0}_{3 \times 3} \quad \mathbf{I}_{3 \times 3}] \quad (3.35)$$

with the matrices $\Omega_{21}, \Omega_{22}, \Sigma_2 \in \mathbb{R}^{3 \times 3}$ given by:

$$\Omega_{21} = - \begin{bmatrix} \omega_{01} & 0 & 0 \\ 0 & \omega_{02} & 0 \\ 0 & 0 & \omega_{03} \end{bmatrix} \quad (3.36)$$

$$\Omega_{22} = - \begin{bmatrix} 2\zeta_1 \omega_{01} & 0 & 0 \\ 0 & 2\zeta_2 \omega_{02} & 0 \\ 0 & 0 & 2\zeta_3 \omega_{03} \end{bmatrix} \quad (3.37)$$

$$\Sigma_2 = \begin{bmatrix} \sigma_1 & 0 & 0 \\ 0 & \sigma_2 & 0 \\ 0 & 0 & \sigma_3 \end{bmatrix} \quad (3.38)$$

3.2.2 Observer design

In this work, the observer is intended to separately estimate the low- and wave-frequency components of a ship motions. Also, the vector of bias loads is also estimated by the observer, so that it may be considered as feedforward in the controller.

With basis on the model presented in the last section, the observer equations may be defined as following:

$$\dot{\hat{\xi}} = \Omega \hat{\xi} + \mathbf{K}_1 \tilde{\mathbf{y}} \quad (3.39)$$

$$\dot{\hat{\eta}} = \mathbf{J}(\mathbf{y}) \hat{\mathbf{v}} + \mathbf{K}_2 \tilde{\mathbf{y}} \quad (3.40)$$

$$\dot{\hat{\mathbf{b}}} = -\mathbf{T}^{-1} \hat{\mathbf{b}} + \Lambda \tilde{\mathbf{y}} \quad (3.41)$$

$$\mathbf{M} \dot{\hat{\mathbf{v}}} = -\mathbf{N} \hat{\mathbf{v}} + \mathbf{J}^T(\mathbf{y}) \hat{\mathbf{b}} + \mathbf{J}^T(\mathbf{y}) \kappa \tilde{\mathbf{y}} + \boldsymbol{\tau}_{con} \quad (3.42)$$

$$\dot{\hat{\mathbf{y}}} = \hat{\eta} + \Gamma \hat{\xi} \quad (3.43)$$

where $\mathbf{y} \in \mathbb{R}^3$ is the measurement, $\tilde{\mathbf{y}} = \mathbf{y} - \hat{\mathbf{y}} \in \mathbb{R}^3$ is the position estimation error and $\mathbf{K}_1 \in \mathbb{R}^{6 \times 3}$, $\mathbf{K}_2 \in \mathbb{R}^{3 \times 3}$, $\Lambda \in \mathbb{R}^{3 \times 3}$ and $\kappa \in \mathbb{R}^{3 \times 3}$ are gain matrices for the observer, whose calculation are based on the passivity of the estimation error dynamics.

3.2.3 Gains determination

Let the gain matrices have the following structure:

$$\mathbf{K}_1 = \begin{bmatrix} k_{11}^o & 0 & 0 \\ 0 & k_{12}^o & 0 \\ 0 & 0 & k_{13}^o \\ k_{21}^o & 0 & 0 \\ 0 & k_{22}^o & 0 \\ 0 & 0 & k_{23}^o \end{bmatrix} \quad (3.44)$$

$$\mathbf{K}_2 = \begin{bmatrix} k_{31}^o & 0 & 0 \\ 0 & k_{32}^o & 0 \\ 0 & 0 & k_{33}^o \end{bmatrix} \quad (3.45)$$

$$\mathbf{\Lambda} = \begin{bmatrix} \lambda_1^o & 0 & 0 \\ 0 & \lambda_2^o & 0 \\ 0 & 0 & \lambda_3^o \end{bmatrix} \quad (3.46)$$

$$\mathbf{\kappa} = \begin{bmatrix} \kappa_1^o & 0 & 0 \\ 0 & \kappa_2^o & 0 \\ 0 & 0 & \kappa_3^o \end{bmatrix} \quad (3.47)$$

The following procedure ensures that the estimates converge to the real states according to passivity theory, through proper determination for the gains above. Also, the gains are chosen in a way that the observer works as a notch filter, improving its performance on wave filtering. Let ω_{0i} be the dominating frequencies of the responses and $\omega_{ci} > \omega_{0i}$ the desired filter cut-off frequency. Also, let $\zeta_{ni} > \zeta_i$ be the notch effect parameter. The gains of \mathbf{K}_1 and \mathbf{K}_2 are then defined according to:

$$k_{1i}^o = -2\omega_{ci}(\zeta_{ni} - \zeta_i) \frac{1}{\omega_{0i}} \quad (3.48)$$

$$k_{2i}^o = 2\omega_{0i}(\zeta_{ni} - \zeta_i) \quad (3.49)$$

$$k_{3i}^o = \omega_{ci} \quad (3.50)$$

Once fulfilled the above requirements, the remainder gains should be assigned as to satisfy the following relation:

$$\frac{1}{T_i} \ll \frac{\lambda_i}{\kappa_i} < \omega_0 < \omega_{ci} \quad (3.51)$$

where $T_i \gg 1$ are the terms of the T matrix on equation (3.29). The above choices for the observer gains are enough to satisfy the requirements for passivity, as developed in (FOSSSEN and STRAND, 1999), where the proofs and stability analyses may be found.

3.3 THE LINE-OF-SIGHT GUIDANCE SYSTEM

A popular application of control theory in marine vehicles is the design of autopilots, systems intended to control the ship heading ψ by means of its rudder(s). Therefore, for a given reference ψ_{ref} , the objective of an autopilot is to render the heading offset ϵ_ψ to zero, that is:

$$\epsilon_\psi = \psi_{ref} - \psi \rightarrow 0 \text{ for } t \rightarrow \infty \quad (3.52)$$

Besides, an autopilot generally also controls the surge velocity of the ship, by increasing or decreasing the propeller(s) rotation in order to keep the required speed u_{ref} . Therefore, a ship provided with an autopilot may keep constant speed and headings without interference of a human operator.

Maintaining a constant heading, however, is not enough to keep a ship over a given trajectory. In fact, the vessel may drift away from it due bias loads from current, wind and second order wave effects, even though it preserves the commanded value for ψ_{ref} . The reason for this is that keeping a vessel advancing over a desired path (including its orientation) is a problem in 3 DOF, which cannot be simultaneously controlled by means of independent control inputs in only 2 DOF. That is, a ship provided with only main propellers and rudders is *underactuated* for the problem of horizontal motions (BREIVIK, 2003).

A relatively simple way to overcome this problem is by usage of the *line-of-sight* (LOS) guidance system, which consists in a methodology to generate a reference heading ψ_{ref} such that the ship points to the trajectory. That is, when the ship drifts away from the desired path, the value for ψ_{ref} is calculated as to orient her back to it.

The first step for applying the LOS strategy is to divide the desired trajectory in waypoints. Then, the ship current position is compared with the so-called *LOS position* $p_{los} = (x_{los}, y_{los})$, which corresponds to a point located on the segment

defined by the previous p_{k-1} and next p_k waypoints. The ship position p_s is considered to be the center of a circle with radius equal to nL , where $n \in \mathbb{N}$ and L is the ship length. This circle intercepts the segment in two points, and p_{los} is chosen to be the one closest to p_k . Then, ψ_{ref} is calculated according to:

$$\psi_{ref}(t) = \text{atan} \left(\frac{y_{los} - y(t)}{x_{los} - x(t)} \right) \quad (3.53)$$

Let $\Delta x = x_k - x_{k-1}$ and $\Delta y = y_k - y_{k-1}$ denote the distances between the next and previous x and y waypoints positions. The calculation of x_{los} and y_{los} may be carried out by solving the following set of equations (FOSSEN, BREIVIK and SKJETNE, 2003):

$$(y_{los} - y)^2 + (x_{los} - x)^2 = (nL)^2 \quad (3.54)$$

$$\frac{y_{los} - y_{k-1}}{x_{los} - x_{k-1}} = \frac{y_k - y_{k-1}}{x_k - x_{k-1}} \quad (3.55)$$

Also, it is necessary to create a switching algorithm in order to select the waypoints according to the ship instantaneous position. This task is done by attributing a value $R_k \leq nL$ for each waypoint, so that it is considered to be the current one if the ship is inside the *circle of acceptance* with center in p_k and radius R_k . The procedure described above is represented on Figure 3.3.

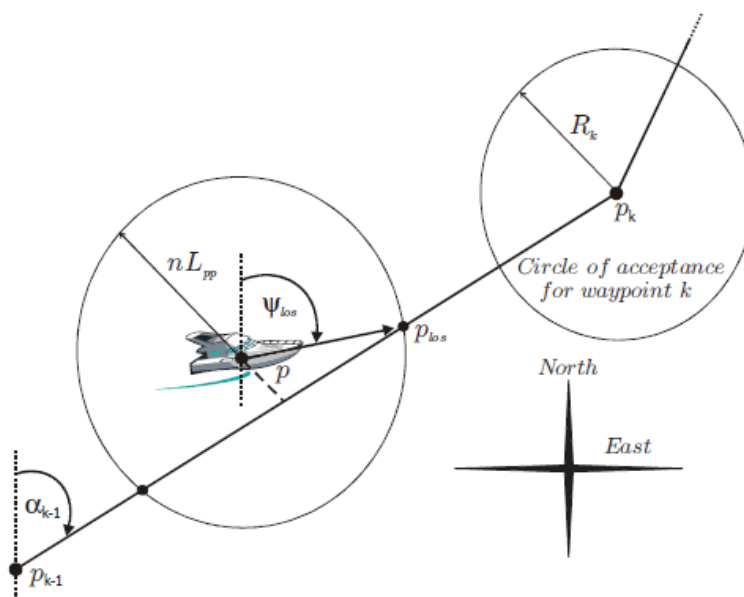


Figure 3.3 – Line-of-sight procedure for calculation of ψ_{ref} (BREIVIK, 2003).

4. UNDERWAY SIDE-BY-SIDE OPERATION

A functional alternative for oil transfer between two ships consists in disposing them side-by-side, as illustrated in Figure 4.1. It is attractive in the sense of hoses handling, since the small distance between both vessels allows this task to be done by cranes. Also, ships are moored together so as to avoid excessive relative motions, enhancing the safety of the operation.



Figure 4.1 – Side-by-side operation (OCIMF, 2005).

A side-by-side operation may be whether static or with underway vessels. In the first case, one of the tankers is anchored and the transfer is carried out with stationary ships. In spite of the gain in safety, a drawback is that it is out of question to anchor a shuttle tanker in deep sea every time an offloading operation is to be performed. In fact, this solution fits usually to the case when one of the ships is an anchored FPSO, like described in (BUCHNER, VAN DIJK and DE WILDE, 2001).

For the purposes of oil transfer in deep sea, moving alternatives must be considered. These can be performed both with ships drifting freely or advancing at low-speed (BERG and BAKKE, 2008). In the latter case, the shuttle tanker develops power ahead at approximately 5 knots, towing the VLCC together while the cargo is transferred. The operation may be divided into the following stages:

- approach maneuver;

- berthing;
- mooring;
- hose connection;
- cargo transfer;
- hose disconnection;
- unmooring, unberthing and departure maneuver.

These phases are briefly described below (OCIMF, 2005).

Approach maneuver

The VLCC keeps a straight trajectory at a speed of about 5 knots, while the shuttle tanker approaches parallelly to the VLCC course. At this moment, fenders should already be placed on the proper locations (preferably in the smaller ship, in order to diminish the probability of contact between hulls).

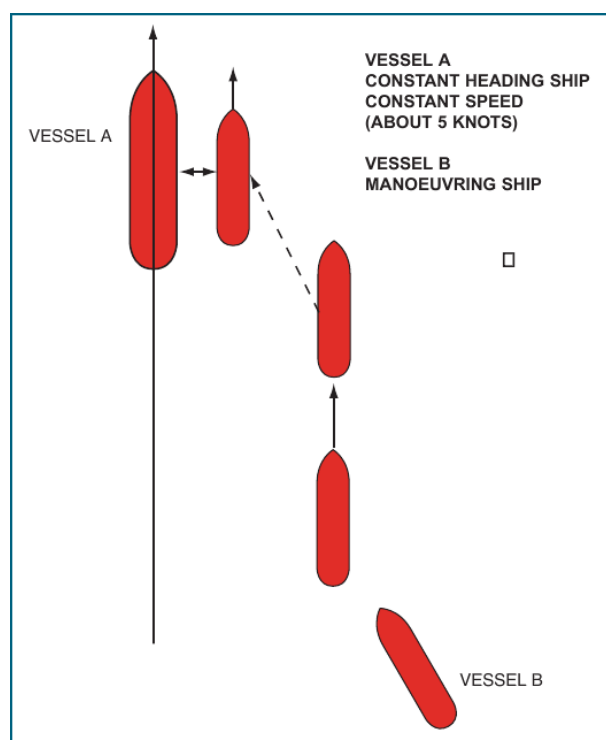


Figure 4.2 – Maneuvering and berthing (OCIMF, 2005).

Berthing

When ships are parallel and close high hydrodynamic interaction loads attract them apart. This effect must be taken into account for the purposes of fender selection.

Mooring

The choice of mooring lines must be based on the ships sizes, the expected differences between freeboards and on weather conditions. The mooring scheme should allow ships motions and freeboard changes, in order to avoid excessive tension in the ropes. OCIMF¹⁵ recommends 6 to 8 lines to link ships bows, 4-6 in the ships sterns and two pairs to be used within 35 meters fore and aft the ships manifolds (which are to be aligned for the transfer operation).

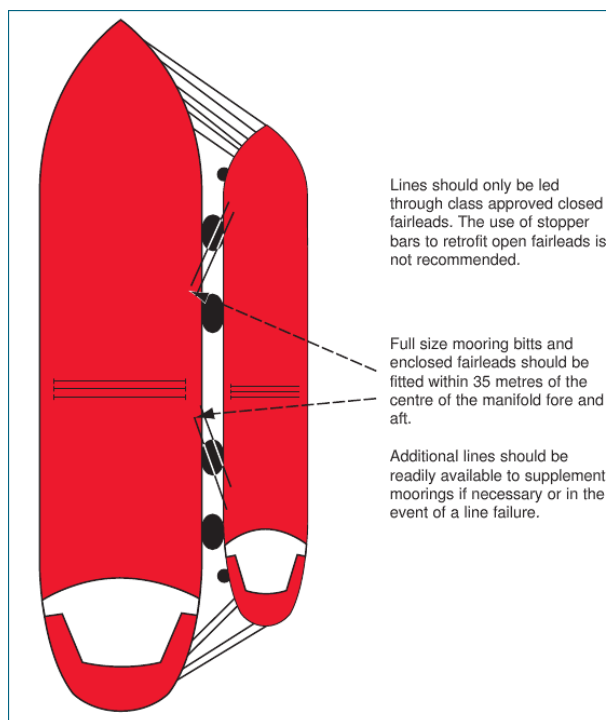


Figure 4.3 - Typical mooring scheme (OCIMF, 2005).

Hose connection and oil transfer

When ships are safely moored, the cranes handle the hoses and the specialized crew performs the connection so that the oil transfer may begin. Previous studies must be performed to determine the weather conditions under which operations would be suspended, in order to avoid undesirable hose disconnection.

Unberthing and departure maneuver

When the oil transfer is over, hoses are disconnected and ships are unmoored. Then, both vessels head to wind for unberthing, so that ships bows are repulsed

¹⁵ Oil Companies International Marine Forum.

away from each other. Separation is then performed and each ship may maneuver to follow its destination.

The present chapter focuses on the dynamics involved during the **transfer phase**. Thus, the next sections will treat the equations of motions, models for mooring lines and fenders and a discussion on hydrodynamic interactions. Subsequently, simulation results for different conditions are presented and discussed.

4.1 HYDRODYNAMIC INTERACTIONS

The condition of two advancing ships at a separation distance as short as 3 meters is not without complications, from the hydrodynamics point-of-view. In fact, important interaction effects are involved due to the fluid behavior between the vessels. They can be divided into two main classes of phenomena, viz.:

- *suction loads*, arisen from the alteration off the pressure field due to the fluid behavior between the hulls, in calm water;
- *wave interaction*, that is, effects related to the wave-field generated between hulls.

The influence of the effects listed above is determinant for the dynamics of a side-by-side operation. Thus, a discussion on this topic is presented in the following subsections.

4.1.1 Suction loads

When two ships navigate side-by-side and with zero relative speed, the flow between them is disturbed such that the resulting pressure field inducts a suction force in the hulls. A simplified explanation for this phenomenon comes from the faster velocity of the fluid between hulls. This would lead to a reduction on the pressure field and, consequently, to the suction forces.

However, studies concerning this kind of loads for the specific situation approached in the presented work – viz., deep-waters and zero relative speed – are incipient. The main studies on the area relate to encounter/overpassing maneuvers in shallow waters and with a separation distance comparable to the ships beams. Other publications tackle the underway replenishment operations, which consist in two ships navigating parallel and in deep waters, but at a distance of the order of half a ship length.

An interesting approach to overcome the lack of studies suitable for side-by-side operations is given in (DE DECKER, 2006). The method consists in using shallow water data from (VANTORRE, VERZHBITSKAYA and LAFORCE, 2002) to create a polynomial regression to estimate interaction forces and moments between ships navigating with zero-relative surge velocity. The author performed experiments and compared the results with the developed method. He concluded that the estimates performed with the model are considerably higher than those observed in the experiments. Anyway, his results are used in the present work, since those conditions are the most similar to the side-by-side case found in literature.

4.1.2 Wave interaction

Let two bodies float in calm water. If one of them is forced to oscillate it disturbs the free-surface around, inducing motions in the second body that, in turn, will also affect the fluid, and so on. If these bodies are subjected to waves, they will be constantly forced to oscillate, leading to the situation depicted on Figure 4.4, where the free-surface elevation between hulls is clearly higher in comparison with the sea.

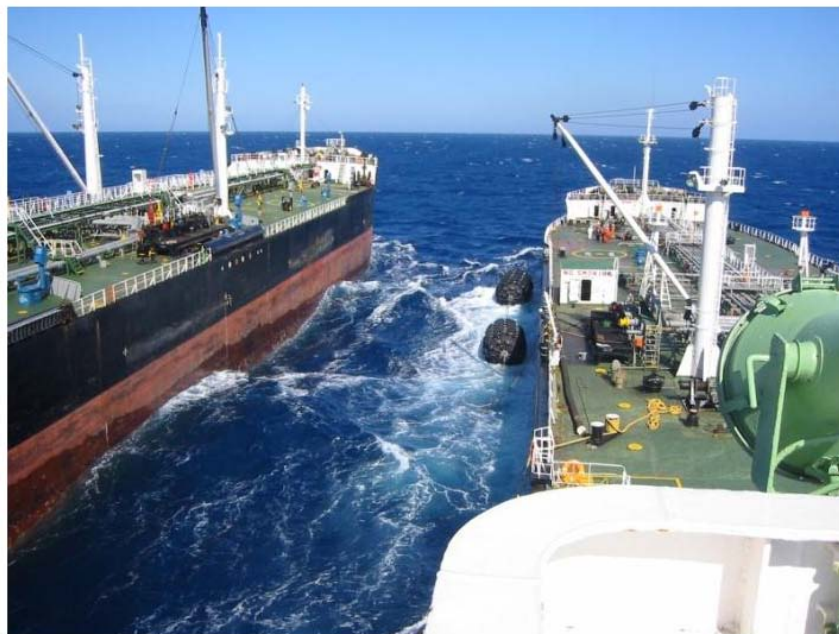


Figure 4.4 – Wave field between two approaching ships (QUADVLIEG, HALLMANN, et al., 2011).

As a consequence of such pronounced waves in the clearance between hulls, different values for ship responses to waves, mean drift loads and radiation effects are expected in comparison with the case of a single vessel in a seaway. A

reliable calculation of these loads is therefore very important for side-by-side operations modeling. However, usual hydrodynamic solvers based on potential theory overestimate wave elevations between close bodies. This happens due to the fact that they do not consider viscous effects in the near field, leading to resonant modes in the free-surface calculated within hulls.

A method was developed to overcome this drawback, based on the consideration of a numerical “lid” on the clearance between ship hulls in the calculation of hydrodynamic data. This approach, adopted in (HUIJSMANS, PINKSTER and DE WILDE, 2001), leads to a rather realistic estimation of wave elevation between ships and, therefore, provide better estimations of the wave loads in the side-by-side case.

4.2 HYDRODYNAMIC CALCULATIONS

For the present work, the adopted hydrodynamic data were obtained through the software WAMIT®. The calculations were performed by a specialized company who used an additional library for application of the lid method cited above.

At first sight, it may not seem adequate to use WAMIT for the present problem, for it is not able to consider bodies with surge velocity, so that ships have to be considered static during the calculations. Nevertheless, it was adopted due to its multibody feature and, mainly, because application of the lid method in hydrodynamic solvers is not trivial, whilst the necessary library and personnel for this task were already available for WAMIT.

Since resonant modes are of critical importance in the problem of wave interactions, they had to be considered in the calculations provided by WAMIT. Determination of these periods was based on the expected frequency of encounter and separation distance between ships.

4.2.1 Calculation of modal periods

Let λ_e be the *encounter wave length*, that is, the wave length associated to the *wave frequency of encounter* ω_e . The projection of the wave length in the ships advance direction λ_{proj} (Figure 4.5) is calculated according to:

$$\lambda_{proj} = \lambda_e \sin \beta \quad (4.1)$$

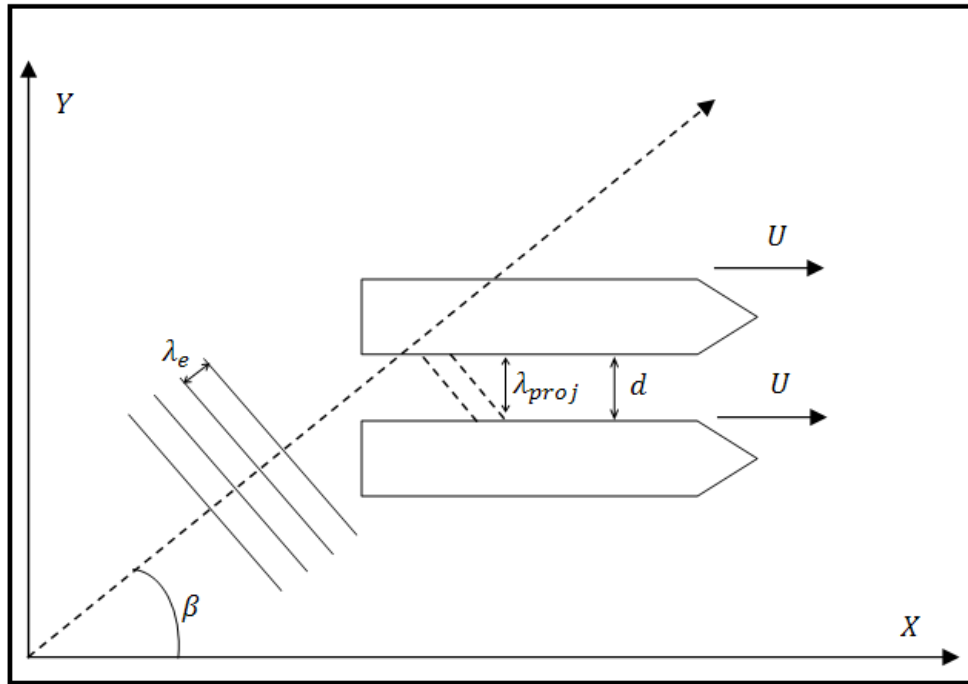


Figure 4.5 – Ships advancing in waves¹⁶.

The present case may be considered analogous to that of resonant modes in the free-surface of a tank with vertical walls. In this situation, the resonant wave lengths are given by:

$$\lambda_{proj} = \frac{2d}{n} \quad (4.2)$$

where $n \in \mathbb{N}^*$ is the natural mode and d is the distance between hulls, as depicted on Figure 4.5. From the dispersion relation one has:

$$\lambda_e = \frac{2\pi g}{\omega_e^2} \quad (4.3)$$

Combining (4.1), (4.2) and (4.3) the following expression for the frequency of encounter ω_e is obtained:

$$\omega_e = \sqrt{\frac{\pi g n \sin \beta}{d}} \quad (4.4)$$

However, ω_e may also be written in terms of β , U and ω_0 (the frequency for zero-velocity) through its definition:

¹⁶ It is important to point out that the coordinate system adopted in WAMIT is different from the Earth-fixed frame utilized in this work, as defined in section 2.2. The necessary transformations are performed before the data is used in the developed model.

$$\omega_e = \left| \omega_0 - \frac{\omega_0^2}{g} U \cos \beta \right| \quad (4.5)$$

Equating (4.4) and (4.5):

$$\left| \omega_0 - \frac{\omega_0^2}{g} U \cos \beta \right| = \sqrt{\frac{\pi g n \sin \beta}{d}} \quad (4.6)$$

So that the modal frequencies ω_n may be found according to:

$$\frac{U}{g} \cos \beta \omega_n^2 - \omega_n + \sqrt{\frac{\pi g n \sin \beta}{d}} = 0 \quad (4.7)$$

for $\omega_n > \frac{\omega_n^2}{g} U \cos \beta$, or:

$$\frac{U}{g} \cos \beta \omega_n^2 - \omega_n - \sqrt{\frac{\pi g n \sin \beta}{d}} = 0 \quad (4.8)$$

if $\omega_n < \frac{\omega_n^2}{g} U \cos \beta$ holds. Therefore, for a given distance d between ships and their nominal surge velocity U the roots of the equations above are found by varying those values of β used in WAMIT calculations and, typically, for the first two modal periods (i.e., $n = 1, 2$). If the period $T_n = 2\pi/\omega_n$ lies inside the interval specified for the calculations, it should also be considered for the correspondent separation distance and surge velocity.

4.2.2 The lid method

Attenuation of the resonant interaction effects in the gap between two ships may be done by consideration of a numerical lid over the free-surface, as depicted on Figure 4.6. This lid is an additional structure with a sufficient number of generalized modes, as to feature a hinged behavior that allows reproduction of the free-surface elevation along the gap length. By representing the free-surface with *Chebyshev polynomials*, the proper number of generalized modes may be determined as being the product of the number of Chebyshev modes in the longitudinal and lateral directions (NYX KNOWLEDGE, 2011).

The attenuation effect may be adjusted by means of the damping factor associated to the lid generalized modes. That is, the higher is the damping factor, the lower is the free-surface elevation. Conversely, a zero-damping factor corresponds to the situation without lid. Therefore, a reasonable value for this factor should be determined by e.g. comparison of the numerically calculated free-surface behavior with that one observed in experiments with scale models of the correspondent ships.

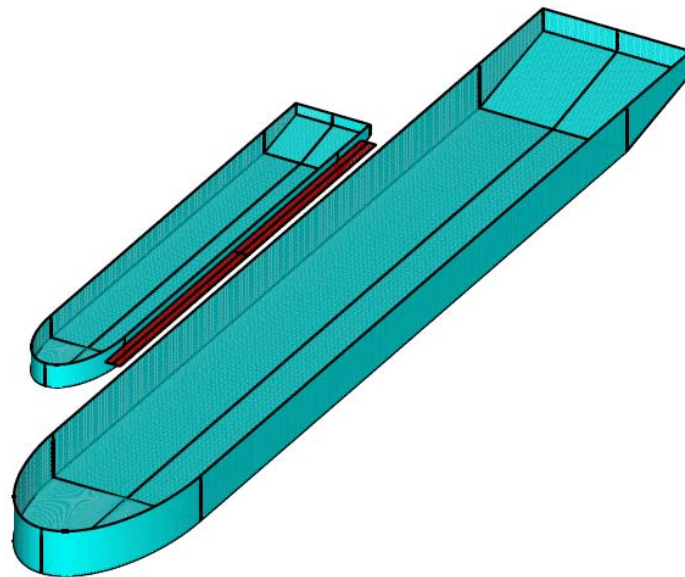


Figure 4.6 – A lid (red) is placed between hulls for attenuation of the free-surface elevation (WAMIT, 2005).

4.2.3 Loading conditions

Since the VLCC has about twice the load capacity of the shuttle tanker, the following loading conditions were considered for the hydrodynamic data calculations:

- VLCC ballasted, shuttle tanker fully loaded;
- VLCC half loaded, shuttle tanker ballasted;
- VLCC half loaded, shuttle tanker fully loaded;
- VLCC fully loaded, shuttle tanker ballasted;

The first condition refers to the case where a first shuttle tanker begins transferring its cargo to an empty VLCC. The second resembles to the end of this operation, so that a second full shuttle tanker starts to offload its cargo to the half-loaded VLCC, leading to the third situation. Finally, the last case

characterizes the situation where the VLCC is completely full, after having received all the oil from both shuttle tankers.

4.3 DYNAMICS

A dynamic model for side-by-side simulations will now be presented based on (SOUZA and MORISHITA, 2011). Once the wave interaction effects arise from the waves irradiated by both bodies, they result in coupled added mass and potential damping matrices. That is, some coefficients relate to the motions of a ship with the radiation forces exerted on the other one. This effect is considered by means of coupled equations of motions. Also, the formulation includes models for the most meaningful loads involved in the operations.

4.3.1 Equations of motions

The condition of two moored ships advancing in waves is a typical situation where the unified model for maneuvering and seakeeping presented in section 2.7.3 must be used. Therefore, equations (2.122) are adapted for the case of two ships with coupled motions. Then, let the 12-dimension state vectors be defined as:

$$\begin{aligned}\boldsymbol{\eta}_{SBS} &= [\boldsymbol{\eta}_{VLCC}^T, \boldsymbol{\eta}_{ST}^T]^T \\ \mathbf{v}_{SBS} &= [\mathbf{v}_{VLCC}^T, \mathbf{v}_{ST}^T]^T\end{aligned}\quad (4.9)$$

where each of the vectors for both the VLCC and the shuttle tanker correspond to the definitions of (2.1) and (2.2). The equations of motion are then written according to:

$$\begin{aligned}\dot{\boldsymbol{\eta}}_{VLCC} &= \mathbf{J}_b^n(\boldsymbol{\eta}_{2,VLCC})\mathbf{v}_{VLCC} \\ \dot{\boldsymbol{\eta}}_{ST} &= \mathbf{J}_b^n(\boldsymbol{\eta}_{2,ST})\mathbf{v}_{ST}\end{aligned}\quad (4.10)$$

$$[\mathbf{M}_{RB} + \mathbf{A}(\infty)]\dot{\mathbf{v}}_{sbs} + [\mathbf{C}_{RB} + \mathbf{C}_A]\mathbf{v}_{sbs} + \boldsymbol{\mu} + \mathbf{G}\boldsymbol{\eta}_{sbs} = \boldsymbol{\tau} \quad (4.11)$$

where $\boldsymbol{\eta}_{2,VLCC}$ and $\boldsymbol{\eta}_{2,ST}$ are the Euler angles vectors for the VLCC and the shuttle tanker, respectively, and the matrices and load vector on (4.11) are defined as:

$$\begin{aligned}\mathbf{M}_{RB} &= \begin{bmatrix} \mathbf{M}_{RB,VLCC} & \mathbf{0}_{6 \times 6} \\ \mathbf{0}_{6 \times 6} & \mathbf{M}_{RB,ST} \end{bmatrix} \\ \mathbf{A}(\infty) &= \begin{bmatrix} \mathbf{A}(\infty)_{VLCC} & \mathbf{A}(\infty)_{VLCC,ST} \\ \mathbf{A}(\infty)_{ST,VLCC} & \mathbf{A}(\infty)_{ST} \end{bmatrix}\end{aligned}\quad (4.12)$$

$$\mathbf{C}_{RB} = \begin{bmatrix} \mathbf{C}_{RB,ST} & \mathbf{0}_{6 \times 6} \\ \mathbf{0}_{6 \times 6} & \mathbf{C}_{RB,ST} \end{bmatrix} \quad (4.13)$$

$$\mathbf{D} = \begin{bmatrix} \mathbf{D}_{VLCC} & \mathbf{D}_{VLCC,ST} \\ \mathbf{D}_{ST,VLCC} & \mathbf{D}_{ST} \end{bmatrix} \quad (4.14)$$

$$\boldsymbol{\mu} = \int_0^t \mathbf{K}(t - \tau) \delta \mathbf{v}(\tau) d\tau \quad (4.15)$$

$$\mathbf{K}(t) = \begin{bmatrix} \mathbf{K}(t)_{VLCC} & \mathbf{K}(t)_{VLCC,ST} \\ \mathbf{K}(t)_{ST,VLCC} & \mathbf{K}(t)_{ST} \end{bmatrix}$$

$$\mathbf{G} = \begin{bmatrix} \mathbf{G}_{VLCC} & \mathbf{0}_{6 \times 6} \\ \mathbf{0}_{6 \times 6} & \mathbf{G}_{ST} \end{bmatrix} \quad (4.16)$$

$$\boldsymbol{\tau} = [\boldsymbol{\tau}_{VLCC}^T, \boldsymbol{\tau}_{ST}^T]^T \quad (4.17)$$

where the cross-terms in (4.12) and (4.14) represent the hydrodynamic coupling explained above. Each of the generalized force vectors $\boldsymbol{\tau}_{VLCC}$ and $\boldsymbol{\tau}_{ST}$ are composed by the following terms:

- Hydrodynamic suction loads
- Fenders loads
- Mooring loads
- Environmental loads

4.3.2 Hydrodynamic suction loads

The model adopted in the present work is based on the expressions developed in (DE DECKER, 2006), which are dependent on the coefficients $C_{h,X}$, $C_{h,Y}$ and $C_{h,N}$, estimated by a polynomial regression of experimental data:

$$\begin{aligned} X_{hdl,s} &= C_{h,X} \frac{1}{2} \rho_{water} B_s T_s U_{VLCC} U_{ST} \\ Y_{hdl,s} &= C_{h,Y} \frac{1}{2} \rho_{water} B_s T_s U_{VLCC} U_{ST} \\ N_{hdl,s} &= C_{h,N} \frac{1}{2} \rho_{water} B_s L_s T_s U_{VLCC} U_{ST} \end{aligned} \quad (4.18)$$

where B_s , T_s and L_s refer respectively to the beam, draft and length of ship s (that may be both VLCC or the shuttle tanker). The velocities U are taken into

account on the expressions for both ships. The hydrodynamic suction loads are then represented by the vector:

$$\boldsymbol{\tau}_{hdl,s} = [X_{hdl,s}, Y_{hdl,s}, 0, 0, 0, N_{hdl,s}]^T \quad (4.19)$$

4.3.3 Fenders loads

Fenders (Figure 4.7) must be placed between ships in order to dump collisions, avoiding steel-steel contact (SAKAKIBARA and YAMADA, 2008). When compressed, each element produces a reaction force perpendicular to its longitudinal vertical plane. Besides, there is also a frictional component parallel to the ships hulls. In this work, however, only the compression forces are considered.



Figure 4.7 – Fenders avoid steel-steel contact between ships hulls (EVERGREEN, 2011).

Each fender is considered as a point placed in the hull of one of the ships. It is admitted that the fenders are placed close enough to the horizontal plane that contains the ship center of gravity, so that their effect in roll moment may be considered as negligible. Figure 4.8 depicts an scheme of the fender model.

Fenders are modeled as non-linear springs. Data must be provided with the reaction forces in function of compression. The diameter of the fenders must also be known. Then, let the ship with fenders be defined as “fender ship”, and the other one as “shocking ship”. Given two points of the shocking ship hull, it is possible to determine the slope and y-intercept of the straight line over which the hull projection lays.

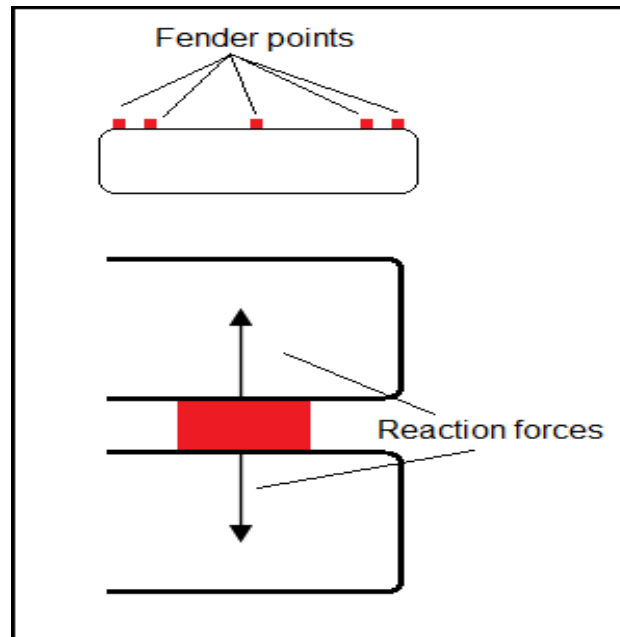


Figure 4.8 – Fender model.

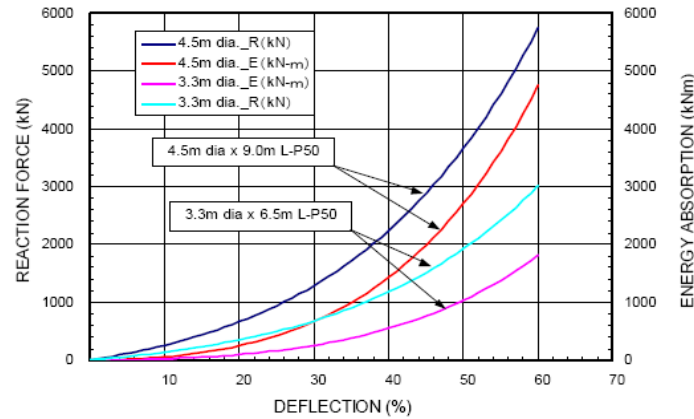
Then, from the fender ship heading it is possible to determine the slope of any straight perpendicular to its hull, which corresponds to the direction of each of the fender reaction forces. Hence, in order to determine whether a fender touches or not the shocking ship hull, it is necessary to verify:

1. if the fender force straight crosses the line segment determined by the most fore and aft points of the shocking ship hull;
2. whether the distance between the fender point and the intersection cited above is greater or smaller than the fender diameter.

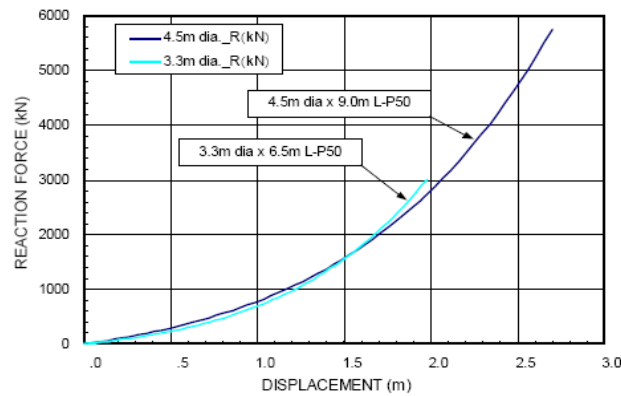
For each fender, condition 1 is verified by means of basic principles of analytic geometry. If it is found that the distance is smaller than the diameter, it means that the fenders are compressed and, thus, reaction force is present. The compression is then calculated and related to the forces from a lookup table. Properties for different types of fenders are presented in Figure 4.9.

Once calculated, fender loads are represented by the vector $\tau_{fnd,s}$

$$\tau_{fnd,s} = [X_{fnd,s}, Y_{fnd,s}, 0, 0, 0, N_{fnd,s}]^T \quad (4.20)$$



(a) Reaction Force, Energy Absorption vs. Deflection (%)



(b) Reaction Force vs. Displacement (m)

Figure 4.9 – Fenders reaction forces X deflection percentage (top) and displacement (bottom) (SAKAKIBARA and YAMADA, 2008).

4.3.4 Mooring loads

Mooring ropes are modeled as non-linear springs linking both ships, with connections in bow, midships and stern. For each line properties like length L_{rope} , diameter D_{rope} and a lookout table with stiffnesses K_{rope} in function of elongation are provided. Besides, the points of connection for each extremity are determined, and then calculation is performed so that line extension may be found. If the distance between both points is bigger than rope length, i.e., the rope is loose, then the tension is null. Conversely, if the distance exceeds the line length, the elongation is then calculated and the traction force and line tension may be determined. Hence, suppose that one extremity is connected to the VLCC at a body-fixed point $\eta_{IVLCC} = [x_{IVLCC}, y_{IVLCC}, z_{IVLCC}]_B$ and the other is connected in to the shuttle tanker at $\eta_{IST} = [x_{IST}, y_{IST}, z_{IST}]_B$. These points are given in the Earth-fixed frame according to:

$$\begin{aligned} [X_{IVLCC}, Y_{IVLCC}, Z_{IVLCC}]_E^T &= \mathbf{n}_{IVLCC} + \mathbf{J}_b^n(\mathbf{n}_{2,IVLCC})[x_{IVLCC}, y_{IVLCC}, z_{IVLCC}]_B^T \\ [X_{IST}, Y_{IST}, Z_{IST}]_E^T &= \mathbf{n}_{IST} + \mathbf{J}_b^n(\mathbf{n}_{2,IST})[x_{IST}, y_{IST}, z_{IST}]_B^T \end{aligned} \quad (4.21)$$

Then, the distance between both points may be calculated:

$$d = \sqrt{(X_{IVLCC} - X_{IST})^2 + (Y_{IVLCC} - Y_{IST})^2 + (Z_{IVLCC} - Z_{IST})^2} \quad (4.22)$$

And the unit vector pointing from the point on the shuttle tanker to the point on the VLCC is given by:

$$\mathbf{v}_{21} = \left[\frac{X_{IVLCC} - X_{IST}}{d}, \frac{Y_{IVLCC} - Y_{IST}}{d}, \frac{Z_{IVLCC} - Z_{IST}}{d} \right] \quad (4.23)$$

Then, a comparison between the distance d and the rope length L_{rope} is made. If $d > L_{rope}$, then the elongation ϵ_{rope} is computed:

$$\epsilon_{rope} = \frac{d - L_{rope}}{L_{rope}} \quad (4.24)$$

So that the traction T_{rope} is found by interpolation of ϵ_{rope} in the table with values for K_{rope} . Finally, the tension is calculated based on assumption of constant section diameter:

$$\sigma_{rope} = \frac{T_{rope}}{\pi D^2 / 4} \quad (4.25)$$

The value of σ_{rope} may be used in order to verify if limit values for the rope tension are exceeded. If, however, $d < L_{rope}$ is verified, both the traction and tension are set to zero. Once the traction on the rope is calculated, it is possible to determine the forces and moments induced on the ships. This is done by multiplying the unit vector calculated in (4.23) by T_{rope} . Attention should be paid to the vector direction:

$$\begin{aligned} \mathbf{F}_{rope,1}^E &= -T_{rope} \mathbf{v}_{21} \\ \mathbf{F}_{rope,2}^E &= T_{rope} \mathbf{v}_{12} \end{aligned} \quad (4.26)$$

These forces are then transformed to the body-fixed frame:

$$\begin{aligned}\mathbf{F}_{rope,1}^B &= \mathbf{J}_b^n(\boldsymbol{\eta}_{2,VLCC})^{-1} \mathbf{F}_{rope,1}^E \\ \mathbf{F}_{rope,2}^B &= \mathbf{J}_b^n(\boldsymbol{\eta}_{2,ST})^{-1} \mathbf{F}_{rope,2}^E\end{aligned}\quad (4.27)$$

So that the X_{rope} , Y_{rope} , and Z_{rope} , components are easily determined from $\mathbf{F}_{rope,1}^B$ and $\mathbf{F}_{rope,2}^B$. The moment \mathbf{M} of a force \mathbf{F} applied at a distance \mathbf{r} from the CG is given by:

$$\mathbf{M} = \mathbf{r} \times \mathbf{F} = \mathbf{S}(\mathbf{F})^T \mathbf{r} \quad (4.28)$$

with the skew-symmetric matrix \mathbf{S} as defined in equation (2.8). Admitting that the body-fixed frame is placed in the centers of gravity of each ship, the moment components K_{rope} , M_{rope} and N_{rope} are given by:

$$K_{rope} = Y_{l1} F_{rope}^Z - Z_{l1} F_{rope}^Y \quad (4.29)$$

$$M_{rope} = Z_{l1} F_{rope}^X - X_{l1} F_{rope}^Z \quad (4.30)$$

$$N_{rope} = X_{l1} F_{rope}^Y - Y_{l1} F_{rope}^X \quad (4.31)$$

This procedure is performed for each ship, so that the forces and moments due to mooring lines in 6 DOF are represented by the following vector:

$$\boldsymbol{\tau}_{mrn,s} = [X_{rope,s}, Y_{rope,s}, N_{rope,s}, K_{rope}, M_{rope}, N_{rope}]^T \quad (4.32)$$

4.3.5 Environmental loads

Environmental action was considered with the models presented in section 2.6. A power-spectrum for 1st-order wave loads is calculated from the FTF and the wave spectrum, and inverse Fourier transform is used for time-domain realization in 6 DOF, leading to the generalized forces X_i^{WF} ($i = 1, \dots, 6$). Also, the mean-drift F_i^{MD} loads are calculated according to equation (2.83).

Wind loads (X_{wind} , Y_{wind} , N_{wind}) are calculated for both ships using equations (2.87). Although shadow effects would be significant for the case of two parallel ships, no models were found in the literature other than CFD-based approaches, specific for their respective situations like e.g. tandem configuration.

Finally, it is worth making a brief discussion on the method adopted for evaluation of viscous effects. Fossen (2005) proposed to consider linear

components by placing the correspondent coefficients together with potential damping in the equations of motions, while non-linear terms were included in a separate vector. In this case, current loads could be taken into account by simply considering the relative fluid velocity in the viscous terms, as proposed in section 2.5.2.

This approach, however, is not adequate for the present case for two reasons. Firstly, the available hydrodynamic derivatives model (the one adopted in Chapter 5) was developed for the case of a single ship, and it is not known how satisfactory it would be to use the same coefficients for the side-by-side case. Second, it is not trivial to interpret the meaning of each term in a hydrodynamic derivatives model. That is, one may not for example infer that a term proportional to the acceleration corresponds to the added mass, since radiation loads might be “hidden” into other components. Meanwhile, the formulation presented in this section demands a clear distinction between potential and viscous effects, so that the former should rather be determined by a trustworthy method, like e.g. a potential theory based hydrodynamic solver.

Therefore, choice was made for the short-wing theory model of section (2.6.3) for representation of viscous loads. This option is not free of caveats, since such model was also developed for the single ship case. Besides, it is not adequate for small current incidence angles, so that it was decided to disregard current in the simulations. The situation of ships advancing in a straight path, however, resembles to the case of static vessels with 180° incidence angle current. The Froude number involved $F_n \cong 0.05$ is, on the other hand, low enough for adoption of this model for calculation of X_{curr} , Y_{curr} and N_{curr} .

All the above loads are combined for their respective degrees of freedom, leading to the environmental loads vector $\tau_{env,S}$.

5. CONVOY OPERATION

In convoy formation the oil is transferred while both vessels advance at a speed of approximately 5 knots. The VLCC is followed by the shuttle tanker, which aims to keep a parallel trajectory laterally displaced of d_T meters. The vessels centers of gravity are expected to maintain a longitudinal distance of d_L meters, as depicted in Figure 5.1.

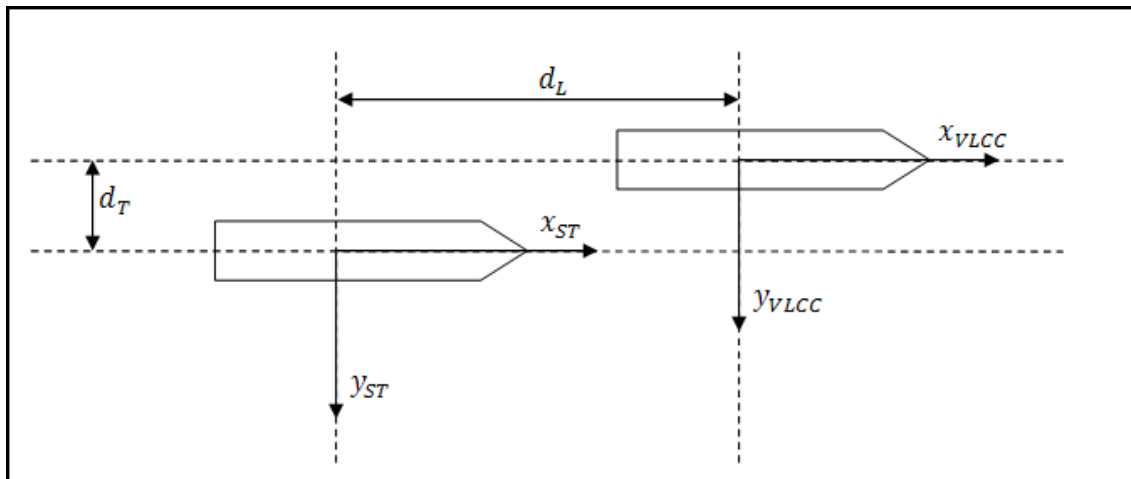


Figure 5.1 - Convoy operation.

The shuttle tanker autopilot must thus be able to maintain the ship over a path generated online according to the VLCC motion. Dynamically positioned ships may perform very low-speed path-following, since they are provided with tunnel thrusters capable of rendering forces in sway direction (SOUZA, OSHIRO and MORISHITA, 2010). However, tunnel thrusters have their capacity drastically reduced when the ship speed increases (MORATELLI JR, 2010). Thus, the problem of underactuation returns in the case of an underway DP-ship.

Such drawback is overcome by proper usage of the guidance system presented in section 3.3. First, an algorithm calculates waypoints according to the VLCC instant positions and the specified relative distances. Then, the line-of-sight strategy is used for calculation of the reference heading, so that the ship is oriented to sail over the specified trajectory. The reference surge speed is assigned according to the differences of velocities and between the desired and the current longitudinal distances between ships.

A nonlinear observer provides estimates of the shuttle tanker low-frequency position, velocities and environmental loads for the backstepping controller.

Such controller is also fed with the references generated by the guidance system, determining the surge force and yaw moments necessary to make the shuttle tanker to follow the waypoints. The resultant commanded loads are limited by models that represent the actuator dynamics. For the force surge, this is done by simply bounding the maximum and minimum thrust that a common Suezmax propeller is able to provide. For yaw moment, a rather developed formulation calculates rudder deflection departing from the commanded moment and rudder dimensions data.

Both the VLCC and the shuttle tanker dynamics are formulated according to a maneuvering model based on hydrodynamic derivatives determined in PMM tests for a tanker. Such tests were performed in the DMI towing tank, in the city of Lyngby, Denmark.

5.1 DYNAMICS

Unlike the side-by-side case, ships motions in the convoy operation may be accurately represented by the superposition of low- and wave-frequency signals provided by a maneuvering and a seakeeping model, respectively. Also, only horizontal motions are of interest for this operation, such that a formulation in 3 DOF is adequate for the purposes of this study.

Both the Earth-fixed and body-fixed coordinate systems are used to describe the equations of motions. Then, let the maneuvering model of section 2.7.1 in 3 DOF be described according to (PEREZ and BLANKE, 2008):

$$\dot{\boldsymbol{\eta}} = \mathbf{J}(\psi)\mathbf{v} \quad (5.1)$$

$$\mathbf{M}_{RB} = \boldsymbol{\tau} - \mathbf{C}_{RB}(\mathbf{v}) \quad (5.2)$$

with the state vectors $\boldsymbol{\eta} = [x, y, \psi]^T$ and $\mathbf{v} = [u, v, r]^T$ correspondent to horizontal motions, only. The Coriolis and centripetal matrix $\mathbf{C}_{RB}(\mathbf{v})$ is given by:

$$\mathbf{C}_{RB}(\mathbf{v}) = \begin{bmatrix} 0 & 0 & -m(x_g r + v) \\ 0 & 0 & mu \\ m(x_g r + v) & -mu & 0 \end{bmatrix} \quad (5.3)$$

where m is the ship mass and x_g is the distance of the center of gravity from the body-fixed coordinate system origin. The vector $\boldsymbol{\tau}$ is a sum of hydrodynamic, control and environmental loads components, that is:

$$\boldsymbol{\tau} = \boldsymbol{\tau}_{hid} + \boldsymbol{\tau}_{ctr} + \boldsymbol{\tau}_{env} \quad (5.4)$$

with $\boldsymbol{\tau}_{hid} = \boldsymbol{\tau}_{hid}(\dot{\mathbf{v}}_r, \mathbf{v}_r, \boldsymbol{\eta})$ composed by forces and moments due to potential and viscous effects, calculated by means of coefficients obtained in PMM tests (FORCE TECHNOLOGY, 2002). The $\boldsymbol{\tau}_{env}$ vector consists of loads from wind and mean drift effects from waves, calculated as presented in section 2.6.

5.2 CONTROL

The control system comprises a combination of a reference generator, a nonlinear observer and a backstepping controller designed for the autopilot case. Such subsystems are described in the following subsections.

5.2.1 References generator (shuttle tanker)

Surge velocity

Let the VLCC sail with at a speed of U_{VLCC} m/s and at a distance of d_L meters forward from the shuttle tanker (Figure 5.1). For a given desired longitudinal distance $d_{L,ref}$, the shuttle tanker reference surge speed $u_{ST,ref}$ is then calculated according to:

$$u_{ST,ref} = \frac{U_{VLCC} + k(d_L - d_{L,ref})}{\cos \psi_{rel}} \quad (5.5)$$

where k is a positive gain and ψ_{rel} is the difference between the headings of the VLCC and the shuttle tanker:

$$\psi_{ref} = \psi_{VLCC} - \psi_{ST} \quad (5.6)$$

The division by $\cos \psi_{rel}$ offsets the fact the ships trajectories are not perfectly parallel. According to the formulation above, the shuttle tanker surge velocity is assigned in order to keep the reference longitudinal distance d_L between both ships. When the error is positive, that is, ships are farther than desired, the shuttle tanker speeds up in order to approximate itself to the VLCC. Oppositely,

the reference speed decreases. The gain k should be adjusted in order to specify the speed change rate.

Waypoints generator

The line-of-sight strategy presented in section (3.3) demands waypoints in order to properly guide the ship through the desired trajectory. In the present case, such waypoints are generated according to the VLCC position and the specified lateral distance between ships trajectories. A *circle of acceptance* with center in each waypoint and a given radius r_{wp} determines the region the shuttle tanker must enter in order to the waypoint to be considered the *current waypoint*. Once it happens, the *next waypoint* is generated according to the following expression:

$$\begin{bmatrix} X_{wp,next} \\ Y_{wp,next} \end{bmatrix} = \begin{bmatrix} X_{traj} \\ Y_{traj} \end{bmatrix} + d_{wp} \begin{bmatrix} \cos \psi_{VLCC} \\ \sin \psi_{VLCC} \end{bmatrix} \quad (5.7)$$

where d_{wp} is the distance between the next waypoint position and the shuttle tanker desired position $[X_{traj}, Y_{traj}]^T$, calculated according to:

$$\begin{bmatrix} X_{traj} \\ Y_{traj} \end{bmatrix} = \begin{bmatrix} x_{vlcc} \\ y_{vlcc} \end{bmatrix} + \begin{bmatrix} \cos \psi_{VLCC} & -\sin \psi_{VLCC} \\ \sin \psi_{VLCC} & \cos \psi_{VLCC} \end{bmatrix} \begin{bmatrix} -d_{L,ref} \\ d_T \end{bmatrix} \quad (5.8)$$

with x_{vlcc} , y_{vlcc} , ψ_{vlcc} , $d_{L,ref}$ and d_T as defined in Figure 5.1. Given two consecutive waypoints and the estimated current shuttle tanker position, the desired heading $\psi_{ST,ref}$ is determined by:

$$\psi_{ST,ref} = \text{atan} \left(\frac{y_{los} - \bar{y}_{ST}}{x_{los} - \bar{x}_{ST}} \right) \quad (5.9)$$

with x_{los} and y_{los} determined according to the procedure described on section 3.3 and \bar{x}_{ST} and \bar{y}_{ST} estimated by the state observer.

5.2.2 Controllers

VLCC

The VLCC autopilot calculates the control loads according to the procedure detailed in section 3.1.1. The references for surge velocity $u_{VLCC,ref}$ and heading $\psi_{VLCC,ref}$ are manually determined, since the task for this ship is simply to

follow a straight course and occasionally perform some deviations. Then, the necessary surge force and yaw moment are determined according to equations (3.2) and (3.3).

Shuttle tanker

The controller adopted for the shuttle tanker is an adaptation of the backstepping strategy presented on section 3.1.2 for an autopilot, as proposed in (BREIVIK, 2003). The model used for the controller is the one presented on equation (3.23), reproduced here for the sake of plainness:

$$\begin{aligned} \mathbf{M}\dot{\mathbf{v}} + \mathbf{N}\mathbf{v} &= \mathbf{J}^T(\boldsymbol{\eta})\mathbf{b} + \boldsymbol{\tau}_{cont} \\ \dot{\boldsymbol{\eta}} &= \mathbf{J}(\boldsymbol{\eta})\mathbf{v} \end{aligned} \quad (5.10)$$

where $\boldsymbol{\tau}_{cont} = \boldsymbol{\tau}_{backs} - \mathbf{J}^T(\boldsymbol{\eta})\hat{\mathbf{b}}$, $\boldsymbol{\tau}_{backs}$ being the control load to be developed by the backstepping controller and $\hat{\mathbf{b}}$ the estimated vector of bias forces and moments, see section 3.2.2. Also, the substitution $\boldsymbol{\tau}_{env} = \mathbf{J}^T(\boldsymbol{\eta})\mathbf{b}$ has already been performed. Then, defining the *projection vector* \mathbf{h} :

$$\mathbf{h} = [0 \quad 0 \quad 1]^T \quad (5.11)$$

Also, let the *error variables* $z_1 \in \mathbb{R}$ and $\mathbf{z}_2 \in \mathbb{R}^3$ be defined as following:

$$z_1 = \psi - \psi_{ST,ref} = \mathbf{h}^T \boldsymbol{\eta} - \psi_{ST,ref} \quad (5.12)$$

$$\mathbf{z}_2 = [z_{2,1} \quad z_{2,2} \quad z_{2,3}]^T = \mathbf{v} - \boldsymbol{\alpha} \quad (5.13)$$

where $\boldsymbol{\alpha} = [\alpha_1 \quad \alpha_2 \quad \alpha_3]^T$ is a *vector of stabilizing functions*, to be defined below. Then, let the first *Control Lyapunov Function* (CLF) V_1 be expressed as:

$$V_1 = \frac{1}{2} z_1^2 \quad (5.14)$$

Time-differentiation of V_1 leads to:

$$\dot{V}_1 = z_1 \dot{z}_1 = z_1 (\mathbf{h}^T \dot{\boldsymbol{\eta}} - \dot{\psi}_{ST,ref}) = z_1 (\mathbf{h}^T \mathbf{v} - \dot{\psi}_{ST,ref}) \quad (5.15)$$

Combining (5.13) and (5.15):

$$\begin{aligned} \dot{V}_1 &= z_1 \mathbf{h}^T [(\mathbf{z}_2 + \boldsymbol{\alpha}) - \dot{\psi}_{ST,ref}] = z_1 \mathbf{h}^T \mathbf{z}_2 + z_1 (\mathbf{h}^T \boldsymbol{\alpha} - \dot{\psi}_{ST,ref}) \\ &= z_1 \mathbf{h}^T \mathbf{z}_2 + z_1 (\alpha_3 - \dot{\psi}_{ST,ref}) \end{aligned} \quad (5.16)$$

Choosing α_3 according to:

$$\alpha_3 = -cz_1 + \dot{\psi}_{ST,ref} \quad (5.17)$$

with $c > 0$ and replacing in (5.16), one finally gets:

$$\dot{V}_1 = -cz_1^2 + z_1 \mathbf{h}^T \mathbf{z}_2 \quad (5.18)$$

Now, let the second CLF V_2 be defined according to:

$$V_2 = V_1 + \frac{1}{2} \mathbf{z}_2^T \mathbf{M} \mathbf{z}_2 \quad (5.19)$$

Repeating the procedure used for V_1 , time-differentiation of V_2 results in:

$$\dot{V}_2 = -cz_1^2 + z_1 \mathbf{h}^T \mathbf{z}_2 + \frac{1}{2} \mathbf{z}_2^T \dot{\mathbf{M}} \mathbf{z}_2 + \mathbf{z}_2^T \mathbf{M} \dot{\mathbf{z}}_2 \quad (5.20)$$

The last term in equation (5.20) may be explored in terms of the following development:

$$\mathbf{M} \dot{\mathbf{z}}_2 = \mathbf{M}(\dot{\mathbf{v}} - \dot{\boldsymbol{\alpha}}) = -\mathbf{N}\mathbf{v} + \mathbf{J}^T(\boldsymbol{\eta})\mathbf{b} + \boldsymbol{\tau}_{cont} - \mathbf{M}\dot{\boldsymbol{\alpha}} \quad (5.21)$$

Such that (5.20) may be rewritten:

$$\dot{V}_2 = -cz_1^2 + \frac{1}{2} \mathbf{z}_2^T \dot{\mathbf{M}} \mathbf{z}_2 + \mathbf{z}_2^T (\mathbf{h} \mathbf{z}_1 + \mathbf{J}^T(\boldsymbol{\eta})\mathbf{b} + \boldsymbol{\tau}_{cont} - \mathbf{N}\mathbf{v} - \mathbf{M}\dot{\boldsymbol{\alpha}}) \quad (5.22)$$

Now, defining $\bar{\mathbf{b}} = \hat{\mathbf{b}} - \mathbf{b}$ and remembering that $\boldsymbol{\tau}_{cont}$ includes the bias estimation as feedforward action, (5.22) becomes:

$$\dot{V}_2 = -cz_1^2 + \frac{1}{2} \mathbf{z}_2^T \dot{\mathbf{M}} \mathbf{z}_2 + \mathbf{z}_2^T (\mathbf{h} \mathbf{z}_1 - \mathbf{J}^T(\boldsymbol{\eta})\bar{\mathbf{b}} + \boldsymbol{\tau}_{backs} - \mathbf{C}\mathbf{v} - \mathbf{D}\mathbf{v} - \mathbf{M}\dot{\boldsymbol{\alpha}}) \quad (5.23)$$

where \mathbf{N} was expanded in its components \mathbf{C} and \mathbf{D} . Now, noticing that the matrix $(\dot{\mathbf{M}} - 2\mathbf{C})$ is skew-symmetric, the terms in equation (5.23) may be regrouped, so that:

$$\begin{aligned} \dot{V}_2 = & -cz_1^2 + \frac{1}{2} \mathbf{z}_2^T (\dot{\mathbf{M}} - 2\mathbf{C}) \mathbf{z}_2 - \mathbf{z}_2^T \mathbf{D} \mathbf{z}_2 \\ & + \mathbf{z}_2^T [\mathbf{h} \mathbf{z}_1 - \mathbf{J}^T(\boldsymbol{\eta})\bar{\mathbf{b}} + \boldsymbol{\tau}_{backs} - \mathbf{C}\boldsymbol{\alpha} - \mathbf{D}\boldsymbol{\alpha} - \mathbf{M}\dot{\boldsymbol{\alpha}}] \end{aligned} \quad (5.24)$$

where $\frac{1}{2}\mathbf{z}_2^T(\dot{\mathbf{M}} - 2\mathbf{C})\mathbf{z}_2 = 0$. Besides, considering that the observer gains are chosen with observance to the relations exposed on section 3.2.1, it is admitted that the vector of estimates of the bias loads $\hat{\mathbf{b}}$ converges to the correspondent real values \mathbf{b} , that is:

$$\hat{\mathbf{b}} \rightarrow \mathbf{b} \Rightarrow \bar{\mathbf{b}} \rightarrow \mathbf{0} \quad (5.25)$$

The assumption (5.25) may not always hold, but is considered in this work since the vector of bias loads \mathbf{b} has very slow dynamics. Then, choosing $\boldsymbol{\tau}_{backs}$ according to:

$$\boldsymbol{\tau}_{backs} = \mathbf{M}\dot{\boldsymbol{\alpha}} + \mathbf{C}\boldsymbol{\alpha} + \mathbf{D}\boldsymbol{\alpha} - \mathbf{h}z_1 - \mathbf{K}z_2 \quad (5.26)$$

where \mathbf{K} is a controller gain matrix, the following expression for \dot{V}_2 may be finally obtained:

$$\dot{V}_2 = -cz_1^2 - \mathbf{z}_2^T(\mathbf{D} + \mathbf{K})\mathbf{z}_2 \quad (5.27)$$

Since both V_2 and $-\dot{V}_2$ are positive-definite, the origin $[z_1, z_2]$ is Globally Asymptotically Stable in the origin, according to Lyapunov's Direct Method (Appendix A).

An expression for $\boldsymbol{\tau}_{cont}$ must take into account the necessary dynamics for stabilization of the underactuated state, as proposed in (BREIVIK, 2003). Let $\boldsymbol{\tau}_{cont}$ be given according to:

$$\boldsymbol{\tau}_{cont} = [\tau_1, \tau_2, \tau_3]^T = [\tau_1, \tau_3/l_\delta, \tau_3]^T \quad (5.28)$$

where $l_\delta < 0$ is the moment arm from the controlled point (considered as being the center of gravity) to the rudder center of pressure. By comparison with equation (5.26) one finds that:

$$\tau_1 = m_{11}\dot{\alpha}_1 + d_{11}\alpha_1 - k_{11}z_{2,1} - (\hat{b}_1 \cos \psi - \hat{b}_2 \sin \psi) \quad (5.29)$$

$$\tau_3 = m_{32}\dot{\alpha}_2 + m_{33}\dot{\alpha}_3 + c_{32}\alpha_2 + d_{32}\alpha_2 + d_{33}\alpha_3 - z_1 - k_{3,3}z_{2,3} - \hat{b}_3 \quad (5.30)$$

where m_{ij} , c_{ij} , d_{ij} and k_{ij} are terms from the matrices \mathbf{M} , \mathbf{C} , \mathbf{D} and \mathbf{K} , respectively. For the sway mode a relation involving the dynamics of α_2 is derived from (5.26), (5.28) and (5.30):

$$\chi_1 \dot{\alpha}_2 = -\chi_2 \alpha_2 + \beta(z_1, \mathbf{z}_2, \hat{\mathbf{b}}, \alpha_3, \dot{\alpha}_3, \psi) \quad (5.31)$$

where:

$$\chi_1 = m_{32} - l_\delta m_{22} \quad (5.32)$$

$$\chi_2 = l_\delta d_{22} - c_{32} - d_{32} \quad (5.33)$$

$$\begin{aligned} \beta = & z_1 - k_{22} z_{2,2} + k_{33} z_{2,3} \\ & - \hat{b}_1 \cos \psi - \hat{b}_2 \sin \psi + \hat{b}_3 + (c_{23} + d_{23} - d_{33}) \alpha_3 \\ & - m_{33} \dot{\alpha}_3 \end{aligned} \quad (5.34)$$

The equations above suffice to describe the backstepping controller dynamics. Calculation of z_1 , α and $\dot{\alpha}$ demands smooth values for the references $\psi_{ST,ref}$, $\dot{\psi}_{ST,ref}$, $\ddot{\psi}_{ST,ref}$, $u_{ST,ref}$, $\dot{u}_{ST,ref}$. These values are obtained from 3rd and 2nd order systems, respectively, as proposed in (FOSSEN, 2002).

5.3 ACTUATORS DYNAMICS

When a ship maneuvering capability is evaluated, consideration of actuator dynamics and limitations is desirable as to render a rather realistic character to the results. Once the controller may command excessive values for both surge force and yaw moment, characteristics of usual main propeller and rudder are taken into account as to avoid unrealistic accelerations in the system. Also, the commanded yaw moment provided by the controller has to be “translated” in terms of rudder deflection δ_r , since the hydrodynamic derivatives model adopted considers this value as an input in its intern calculations.

Main propeller

The main propeller time constant is considered not to be significant for the ship dynamics, since both vessels are large tankers with slow responses. Therefore, only the higher $T_{max} > 0$ and lower $T_{min} < 0$ thrusts were considered in the dynamics. That is, for a given commanded thrust $\tau_{c,1}$ the effective thrust $\tau_{e,1}$ is determined according to:

$$\tau_{e,1} = \begin{cases} \min\{\tau_{c,1}, T_{max}\}, & \text{for } \tau_{c,1} > 0 \\ \max\{\tau_{c,1}, T_{min}\}, & \text{for } \tau_{c,1} < 0 \end{cases} \quad (5.35)$$

Rudder

From the commanded yaw moment $\tau_{c,3}$ determined by the controller, the lift force on the rudder is found according to:

$$L_{rdd} = \tau_{c,3}/l_{\delta} \quad (5.36)$$

Defining the lift coefficient C_L (SKEJIC, 2008):

$$C_L(\delta_r) = 2\pi \frac{\Lambda(\Lambda + 0.7)}{(\Lambda + 1.7)^2} \sin(\delta_r) + C_Q \sin(\delta_r) |\sin(\delta_r)| \cos(\delta_r) \quad (5.37)$$

where $C_Q \approx 1$ is the *resistance coefficient*, the lift force be modeled according to:

$$L_{rdd} = \frac{\rho_w}{2} A_r^e C_L(\delta_r) u_{rdd} |u_{rdd}| \quad (5.38)$$

where ρ_w is the water density and the effective rudder area A_r^e is calculated by means of the propeller diameter D_p and mean chord c_m :

$$A_r^e \approx D_p c_m \quad (5.39)$$

and the rudder flow velocity calculated by means of the following expression:

$$u_{rdd} = u_r + k_u \left(\sqrt{\frac{8}{\pi \rho_w D_p^2} T_h + u_r^2} - u_r \right) \quad (5.40)$$

where T_h is the value of the thrust developed by the propeller and $k_u \approx 0.5$ is an *induced velocity coefficient*. For a practical range of values for δ_r it may be admitted that expression (5.37) may be approximated by a linear relation:

$$C_L \approx c_1 \delta_r \quad (5.41)$$

Finally, grouping constant terms of (5.37) in a new coefficient L_{δ} :

$$L_{\delta} = \frac{\rho_w}{2} A_r^e c_1 \quad (5.42)$$

The rudder deflection angle may then be related to the lift force, for a given value of u_{rdd} , according to:

$$\delta_r = \frac{L_{rdd}}{L_{\delta} u_{rdd} |u_{rdd}|} \quad (5.43)$$

6. SIMULATIONS AND RESULTS

Departing from the models developed on Chapters 4 and 5, two dynamic simulators were implemented in MATLAB® environment for both the side-by-side and convoy operations. Simulations were then executed for several combinations of loading and environmental conditions, those considered relevant for each operation. Different combinations of sea states and wind velocity were based on values typically observed in Brazilian oil fields.

The VLCC is a 320 m length tanker, while the shuttle tanker has the dimensions of a typical Suezmax class ship. Their main dimensions are presented on Tables 6.1 and 6.2, respectively (see the List of Symbols for definition of the elements bellow).

Table 6.1 – VLCC main dimensions.

	Ballasted	Half loaded	Fully loaded
L_{oa} (m)	332.0	332.0	332.0
L_{pp} (m)	310.0	305.0	320.0
B_s (m)	58.0	58.0	58.0
T_s (m)	7.0	14.0	21.0
D_s (m)	37.2	37.2	37.2
Δ (t)	104,368	216,924	334,661
∇ (m ³)	101,823	211,633	326,498
I_z (kg.m ²)	7.2x10 ⁸	1.4x10 ⁹	1.9x10 ⁹
C_b	0.77	0.79	0.79
S_s (m ²)	18,644	23,663	28,842
A_t (m ²)	3,348	2,567	1,786
A_l (m ²)	12,088	9,267	6,447
A_{wp} (m ²)	15,372	16,027	16,805
KM_t (m)	37.9	24.8	22.8
KM_l (m)	1013.9	547.3	414.4

Table 6.2 – Shuttle tanker main dimensions.

	Ballasted	Fully loaded
L_{oa} (m)	272.8	272.8
L_{pp} (m)	258.0	258.0
B_s (m)	46.0	46.0
T_s (m)	8.0	17.5
D_s (m)	24.4	24.4
Δ (t)	82,055	188,001
∇ (m ³)	80,054	183,416
I_z (kg.m ²)	4.9x10 ⁸	1.1x10 ⁹
C_b	0.81	0.82
S_s (m ²)	13,725	19,488
A_t (m ²)	2,101	884
A_l (m ²)	7,587	3,192
A_{wp} (m ²)	10,566	11,346
KM_t (m)	24.0	18.3
KM_l (m)	634.8	350.5

The difference between freeboards is an important point in the side-by-side case, due to the loads on the mooring ropes. For the convoy case, on the other hand, the ships drafts and freeboards $f = D - T$ have crucial influence on the vessels response to environmental action, with important implications on their controllability.

Once the VLCC has double of the shuttle tanker load capacity, two of the latter are necessary to fully load the former. Therefore, as presented in section 4.2, four loading conditions are considered, viz.:

- Condition 1: a fully loaded shuttle tanker starts the transfer of oil to a completely empty (ballasted) VLCC. In this case, the VLCC and shuttle tanker freeboards are respectively the highest and lowest possible, leading to a difference of 23.3 m.
- Condition 2: in this case, the oil transfer from the first shuttle tanker is already finished, so that the ship is ballasted. Since the VLCC has about

twice the shuttle tanker load capacity, it gets therefore with half of its nominal payload. The difference between freeboard decreases to 6.8 m.

- Condition 3: a second fully loaded shuttle tanker begins its transfer process to the half loaded VLCC. The freeboards difference is again increased, reaching 16.3 m.
- Condition 4: finally, the VLCC gets completely loaded, after having received the total cargo of the shuttle tanker. In this case, the ships freeboards are almost the same, with a difference of just 0.2 m.

Additional information on hydrodynamic data, environmental conditions and more details particularly relevant for each operation are presented in their correspondent following sections.

6.1 SIDE-BY-SIDE

For the side-by-side case, it was considered that ships should follow a straight trajectory at 5 knots, under influence of waves and wind. The shuttle tanker was always equipped with five fenders equally distributed along the hull, since it is the smaller ship. Three different mooring system arrangements were tested, and a total of 18 combinations of incidence angles, wave heights and periods were considered. The objective was to monitor whether the loads on mooring ropes crossed or not the acceptable values.

6.1.1 Fenders properties

Each fender was considered to have 3.3 m in diameter, and their compression properties are displayed on Table 6.3. The value for 100% of compression is clearly unreal, and was assigned in order to avoid “overlaps” between ships. It was admitted that no friction took place between fenders and the ships, so that only loads perpendicular to the hulls were considered.

6.1.2 Mooring system

According to OCIMF’s guidelines for ship-to-ship operations (OCIMF, 2005), typical mooring arrangements consist of 6 to 8 ropes tying ships bows, 4 to 6 ropes linking the sterns and two pairs of mooring bites fore and aft the manifolds (Figure 6.1). It is admitted that each group of mooring lines are connected to a same point in each ship. Therefore, the considered mooring

arrangements were 8-4-6 (i.e., 8 lines in bows, 4 in midships and 6 in sterns), 8-4-4 and 6-4-4.

Mooring lines were considered to have 42 mm in diameter, minimum braking load (MBL) of 1230 kN and service working load (SWL) of 738 kN, correspondent to 60% of the MBL. The relation between elongation and traction is displayed on Table 6.4. Even though values are attributed for elongations correspondent to loads above the MBL, once broken a line does not induce any load on neither of the ships until the simulation is finished.

For all of the mooring arrangements, a pre-tension of 50 kN was assigned for the ropes.

Table 6.3 –Compression X induced force relation for fenders.

Compression (%)	Induced force (kN)
0	0
10	200
20	400
30	600
40	1200
50	1900
60	3000
70	5000
80	10000
90	100000
100	1×10^7

6.1.3 Hydrodynamic data

Selection of the lid damping factor

When applying the lid method presented on section 4.2.2, a damping factor is assigned to the lid generalized modes in order to adjust the resultant free surface behavior between hulls. A proper choice of an adequate value for this damping factor should be done with basis on experiments results, where the free surface elevation could be observed as a function of wave incidence angle, clearance and freeboards difference.

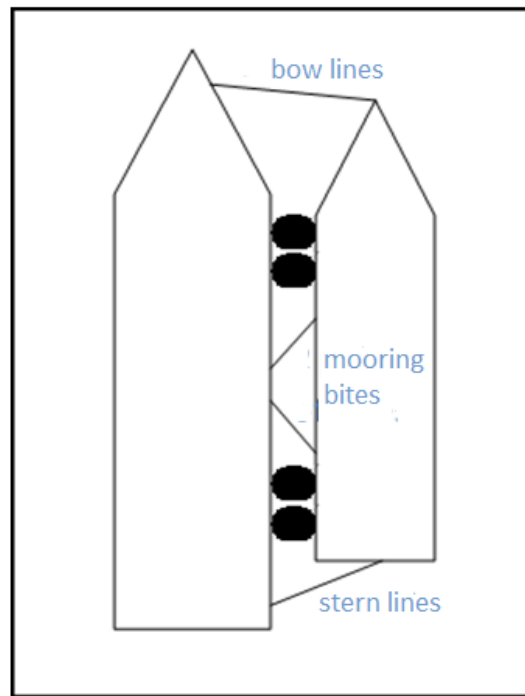


Figure 6.1 – Mooring scheme.

Table 6.4 – Mooring lines properties.

Elongation (%)	Traction (kN)		
	Bow	Midships	Stern
0	0	0	0
2	70	40	20
4	340	240	120
6	960	640	360
8	1240	1180	880
10	1280	1260	1200
12	1300	1300	1240

Such experiments, however, were not in the scope of this work. Besides, for the knowledge of the author there are no results for similar situations on the literature. Therefore, an arbitrary value of 3-4 times the amplitude of the incident wave was adopted for the expected amplitude of the free surface elevation, as a criterion to be followed for the damping factor choice.

As an example, Figure 6.2 shows the free surface elevation for seven different values for the damping factor under the loading condition 1. Since the orange curve has a peak value between 3 and 4 times the incident wave amplitude, the

correspondent value of 3×10^5 kg/s was adopted. Therefore, all hydrodynamic data used for condition 1 simulations are those obtained with this value for the damping factor of the lid generalized modes. A similar procedure was applied for the other loading conditions.

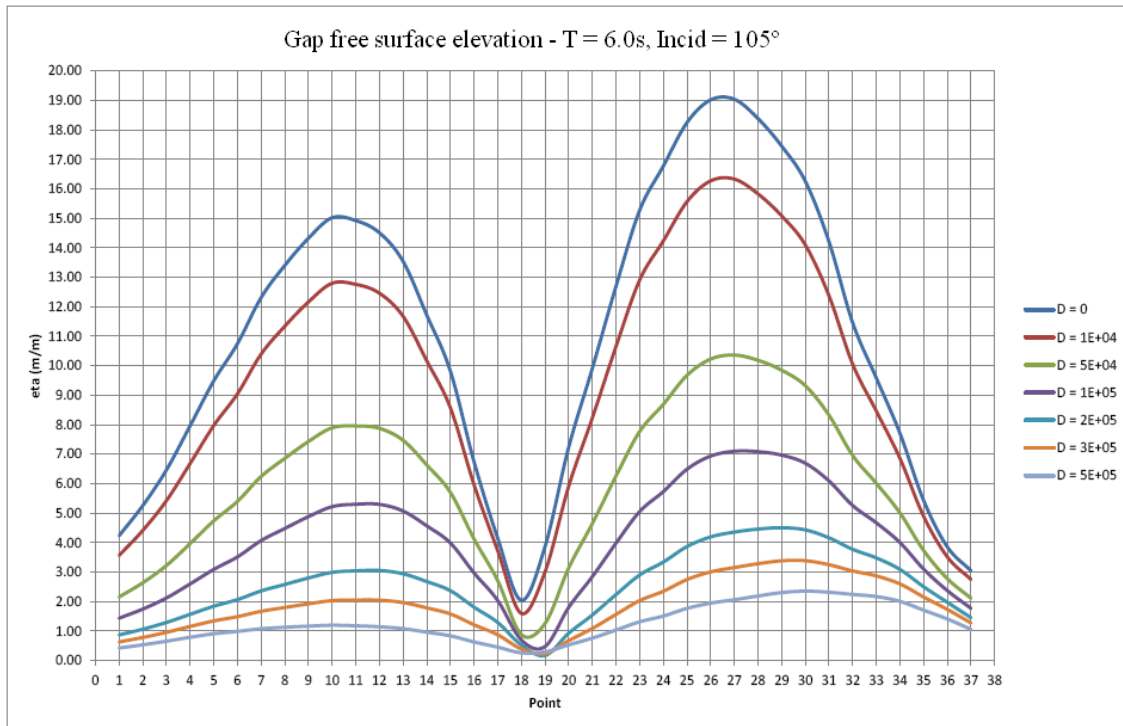


Figure 6.2 – Damped free surface elevation – for a unitary incident wave amplitude – for loading condition 1. The x-axis corresponds to points distributed along the lid length, with 0 and 38 corresponding to the aft- and fore-most extremities, respectively (NYX KNOWLEDGE, 2011).

Memory functions

As discussed on Chapters 2 and 4, in side-by-side operations the mooring system induces wave-frequency loads shared between both ships. The implication of this phenomenon is that it becomes necessary to consider the 1st order wave loads in the equations of motions, demanding a unified model for maneuvering and seakeeping.

Since ships are excited, both added mass and potential damping must be considered as frequency-dependent coefficients. However, this would lead to time- and frequency-dependent equations of motions, a drawback that may be overcome through substitution of frequency-dependent coefficients by convolutions of memory functions in time domain.

This solution, however, would be much time-consuming, so that the state-space approximation of equations (2.123) and (2.124) becomes convenient:

$$\boldsymbol{\mu} = \int_0^t \mathbf{K}(t-t') \dot{\boldsymbol{\xi}}(t') dt' \approx \begin{matrix} \dot{\mathbf{x}} = \widehat{\mathbf{A}}\mathbf{x} + \widehat{\mathbf{B}}\dot{\boldsymbol{\xi}} \\ \widehat{\boldsymbol{\mu}} = \widehat{\mathbf{C}}\mathbf{x} \end{matrix} \quad (6.1)$$

The state-space matrices $\widehat{\mathbf{A}}_r$, $\widehat{\mathbf{B}}_r$ and $\widehat{\mathbf{C}}_r$ may be obtained by means of a parametric approximation of the frequency-domain memory functions $\mathbf{K}(\omega)$. From Fourier transform of 2.113 and 2.117 one gets:

$$\mathbf{K}(j\omega) = \mathbf{B}(\omega) + j\omega[\mathbf{A}(\omega) - \mathbf{A}(\infty)] \quad (6.2)$$

The method proposed in (PEREZ and FOSSEN, 2009) consists in approximating $\mathbf{K}(j\omega)$ according to:

$$\mathbf{K}(j\omega) \approx \widehat{\mathbf{K}}(j\omega) = \widehat{\mathbf{C}}_r(j\omega\mathbf{I} - \widehat{\mathbf{A}}_r)^{-1}\widehat{\mathbf{B}}_r \quad (6.3)$$

where $\widehat{\mathbf{K}}(s)$ is a matrix whose elements are rational transfer functions $\widehat{K}_{ik}(s)$:

$$\widehat{K}_{ik}(s) = \frac{P_{ik}(s)}{Q_{ik}(s)} = \frac{p_r s^r + p_{r-1} s^{r-1} + \dots + p_0}{s^n + q_{n-1} s^{n-1} + \dots + q_0} \quad (6.4)$$

The coefficients p_0, p_1, \dots, p_r and q_0, q_1, \dots, q_r are obtained through identification methods, e.g. Least Square fitting. A discussion on different approaches for the identification process is presented on (TAGHIPUR, PEREZ and MOAN, 2008). In this work, the Matlab [®] toolbox *Marine Systems Simulator* (MSS, 2010) was used for the identification process and generation of the state-space matrices. Figure 6.3 depicts an example of the identification results.

Departing from the hydrodynamic data generated for two interacting parallel ships, the state-space matrices of (6.1) were then obtained. In the context of the unified model for maneuvering and seakeeping, the input for the system is the oscillation of the ship velocities in the body-fixed frame around a vector of mean velocities $\bar{\mathbf{v}}$, that is:

$$\delta\mathbf{v} = \mathbf{v} - \bar{\mathbf{v}} \quad (6.5)$$

Therefore, the memory effects system is linked to the ships equations of motions according to the scheme on Figure 6.4. In the side-by-side case, which comprises two coupled vessels, the vector $\boldsymbol{\mu}$ for each ship is the sum of the outputs of two states-spaces systems: one related to the ship own motions, and

another correspondent to the memory effects due to the motions induced by the other ship.

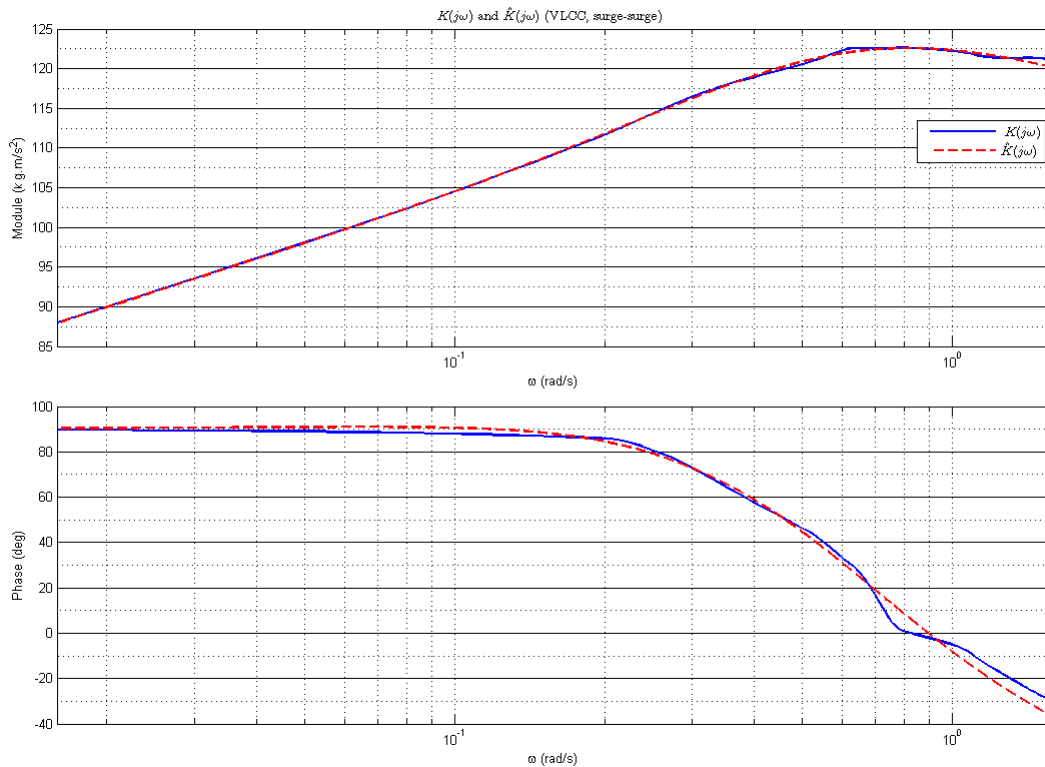


Figure 6.3 – Parametric approximation for the retardation function (VLCC – surge-surge).

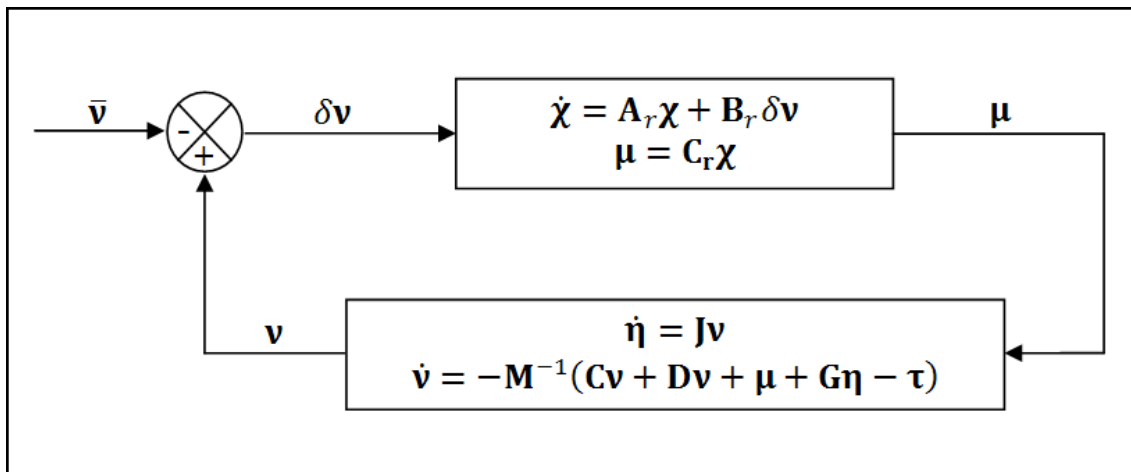


Figure 6.4 – Connection between the equations of motions and the state-space system for approximation of the memory functions vector μ .

After implemented and extensively tested, however, the system showed to be unstable when data for coupled ships were used as input for calculation of the memory function state-space matrices. The memory effects vector presented unrealistically increasing values after few seconds of simulation, rapidly

destabilizing the equations of motions and leading to crashes in the program execution. Investigations were performed as to diagnose whether the problem was on the hydrodynamic data, on the identification process or in the implemented code.

As already mentioned, WAMIT does not perform calculations for underway ships. However, this fact may not be claimed to be the reason for the instabilities, since the same problem occurred for simulations executed without surge speed. Another source of problem could be the behavior of the calculated hydrodynamic coefficients. In Figure 6.5 both added mass and potential damping referent to sway-sway for both the VLCC and the shuttle tanker, together with the respective coupling effects, are depicted. The negative values for added masses at frequencies between 1.0 rad/s and 1.5 rad/s are noteworthy, since for a single ship the diagonal elements of the added mass matrix are usually positive. In fact, Figure 6.6 shows the sway-sway added masses calculated for both interacted and isolated ships, and the odd behavior of the former becomes clear. However, it would be untimely to state that there is some kind of error in the data for interacting ships, since studies on the problem of parallel ships at such a low separation distance are relatively incipient.

Perez and Fossen (2009) remarked that the identification process does not assure stability, since there is not any constraint enforcing the roots of $Q_{ik}(s)$ to have all negative real parts. Therefore, the authors propose to reflect the positive poles about the imaginary axis, followed by recalculation of the polynomial and of the state-space system.

This procedure, however, assigns stability only for the open-loop system of (6.1), but does not ensure stability to the complete nonlinear system depicted on Figure 6.4. In fact, the instabilities persisted after the mentioned “correction” was performed. Finally, the implement code should not be put out of suspicion, even though the extensive series of tests suggests that the problem is too complex to be caused by a mistake in the programming logic.

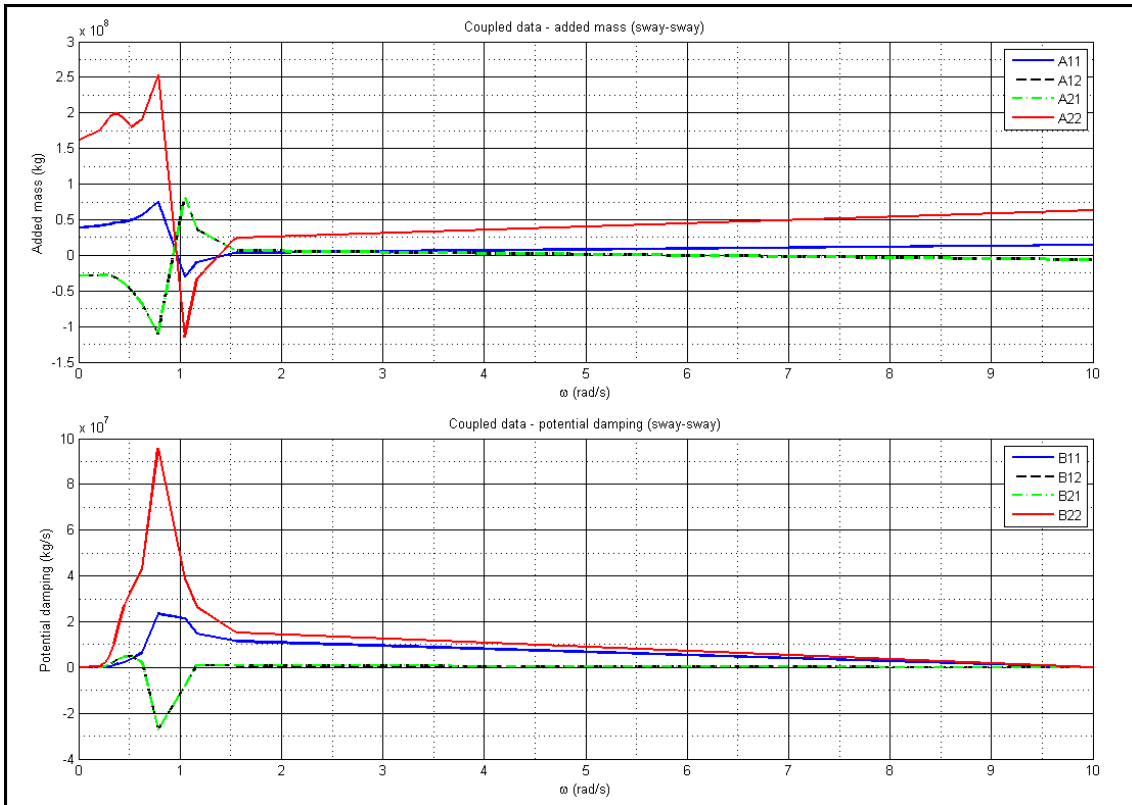


Figure 6.5 – Sway-sway hydrodynamic coefficients referent to the VLCC (A11, B11), to the coupled effects on the VLCC due to the shuttle tanker motions (A12, B12), to the coupled effects on the shuttle tanker due to the VLCC motions (A21, B21) and to the shuttle tanker (A22, B22).

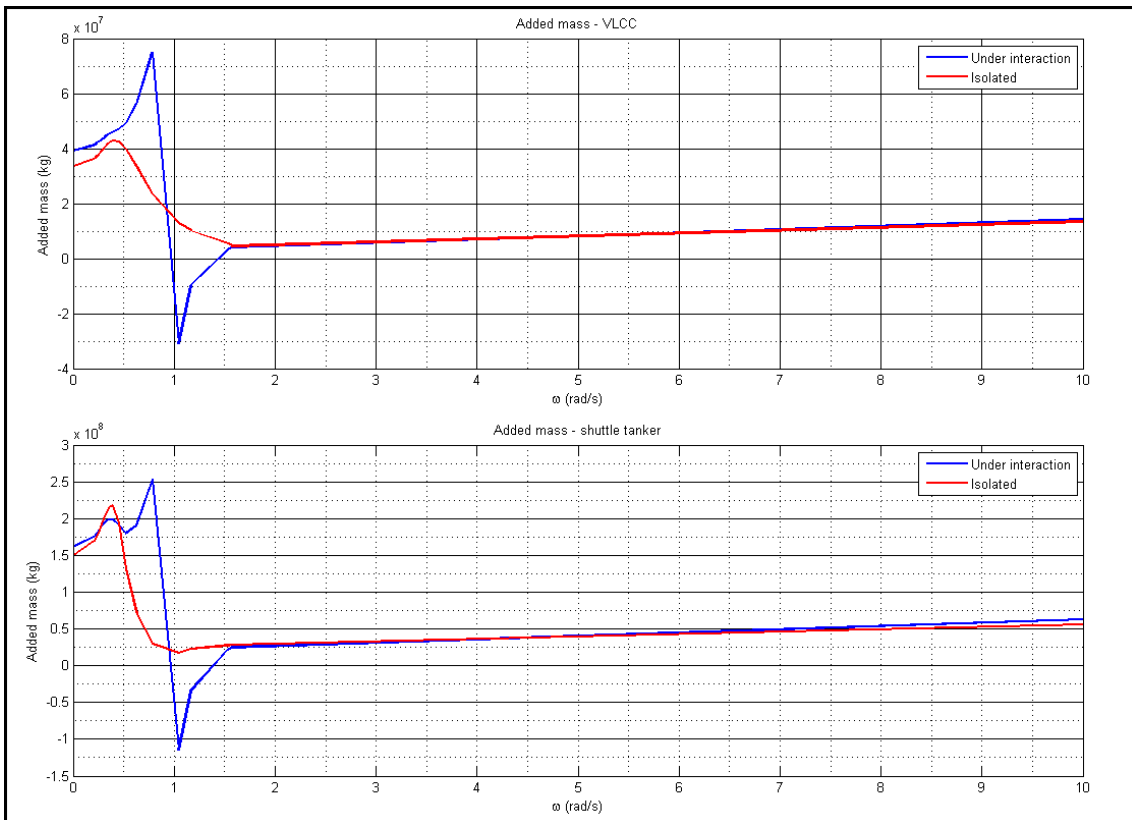


Figure 6.6 – Sway-sway added masses calculated for both isolated and interacting ships.

Since the problem showed to comprise a topic of research broader than the scope of this work, it was decided to adopt an approximation for the unified model for maneuvering and seakeeping by considering added mass and potential damping coefficients relative to the wave peak frequency ω_p . Therefore, equation (4.11) becomes:

$$\begin{aligned} [\mathbf{M}_{RB} + \mathbf{A}(\omega_p)]\dot{\mathbf{v}}_{sbs} + \mathbf{B}(\omega_p)(\mathbf{v}_{sbs} - \bar{\mathbf{v}}_{sbs}) + [\mathbf{C}_{RB} + \mathbf{C}_A(\omega_p)]\mathbf{v}_{sbs} \\ + \mathbf{G}\boldsymbol{\eta}_{sbs} = \boldsymbol{\tau} \end{aligned} \quad (6.6)$$

where $\bar{\mathbf{v}}_{sbs} = [U_s, 0, 0, 0, 0]^T$, $U_s = 5$ knots being the service speed.

The approximation of equation (6.6) may be consistent for representing the radiation loads originated from oscillations due to wave, since most of the spectrum energy is concentrated around ω_p . The same, however, cannot be said about those loads induced by the mooring system, whose frequency depends rather on the ropes stiffness and ships inertias than on the wave peak frequency. Therefore, the exact consequences of considering $\mathbf{A}(\omega_p)$ and $\mathbf{B}(\omega_p)$ for calculating radiation loads may not be foreseen, but it is hoped that at least those relative to the response to waves are closely represented.

6.1.4 Environmental action

The environmental conditions considered in the simulations aimed to resemble typical values observed in Brazilian relevant oil reserves. Pre-salt fields in Campos basin present an average of 2.1 m of significant wave height, with a wind speed of 7.7 m/s. Therefore, it was decided to consider a range of values for H_s that contains the mentioned average. Although higher wave heights correspond to harsher wind conditions, only the mentioned value for wind velocity was regarded in all of the simulations, with incidence direction always the same as the waves.

A large-spaced range for wave periods was considered, since the wave length is determinant in the amplitude of a ship response and, consequently, on the mooring system loads. Besides, two different incidence angles were tested, corresponding to ahead and astern waves. The 18 combinations of wave conditions tested in the simulations are presented on Table 6.5. The JONSWAP

wave spectrum was considered (equation 2.76), with the shape parameter γ set to 1.1.

Table 6.5 – Waves parameters for the side-by-side simulations.

Parameter	Values
Significant height – H_s	1.5 m / 2.5 m / 3.5 m
Peak period – T_p	8.0 s / 11.5 s / 15.0 s
Incidence – β_{waves}	195° / 315°

6.1.5 Simulations results

Simulations were performed for the 18 environmental conditions of Table 6.5, combined with the 3 different mooring arrangements and the 4 loading conditions mentioned above, leading to a total of 216 executions. Each simulation considered 3600 s of operation, during which the VLCC kept constant heading, towing the shuttle tanker together. Figures 6.7 to 6.10 show some results for a simulation of loading condition 1, under waves with significant height of 3.5 meters, peak period of 15.0 seconds and incidence of 195°. The mooring arrangement is 8-4-6.

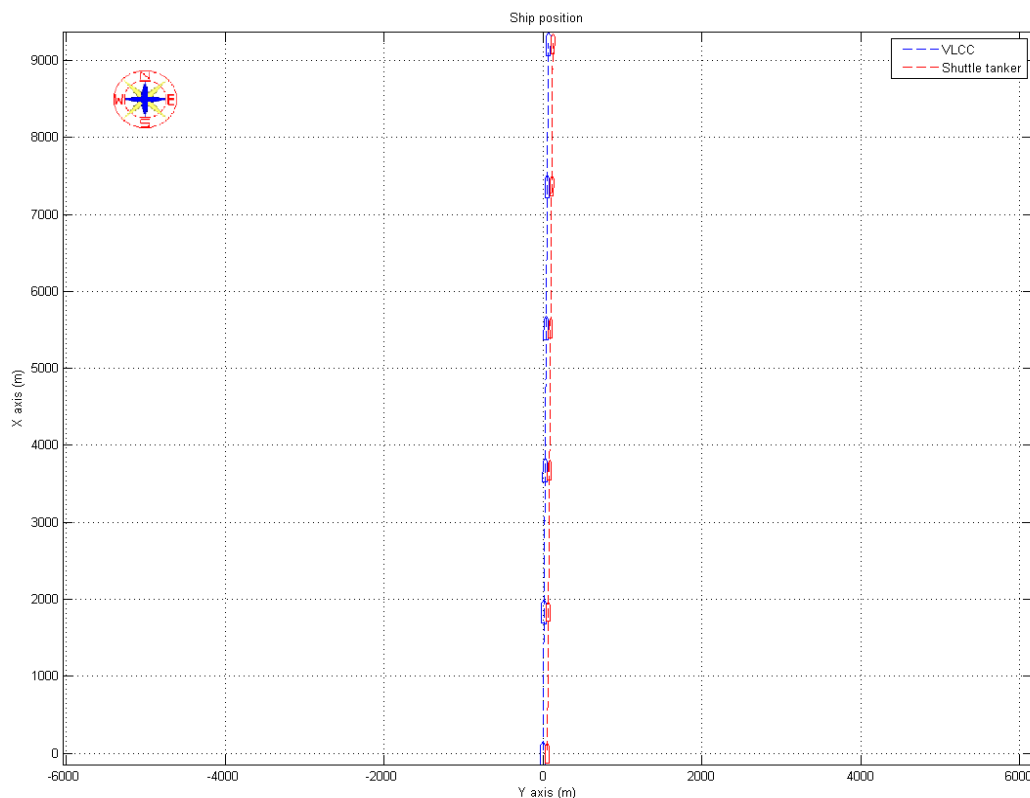


Figure 6.7 – XY positions for side-by-side operation under loading condition 1, $H_s = 3.5$ m, $T_p = 15.0$ s, wave incidence of 195° and mooring arrangement 8-4-6.

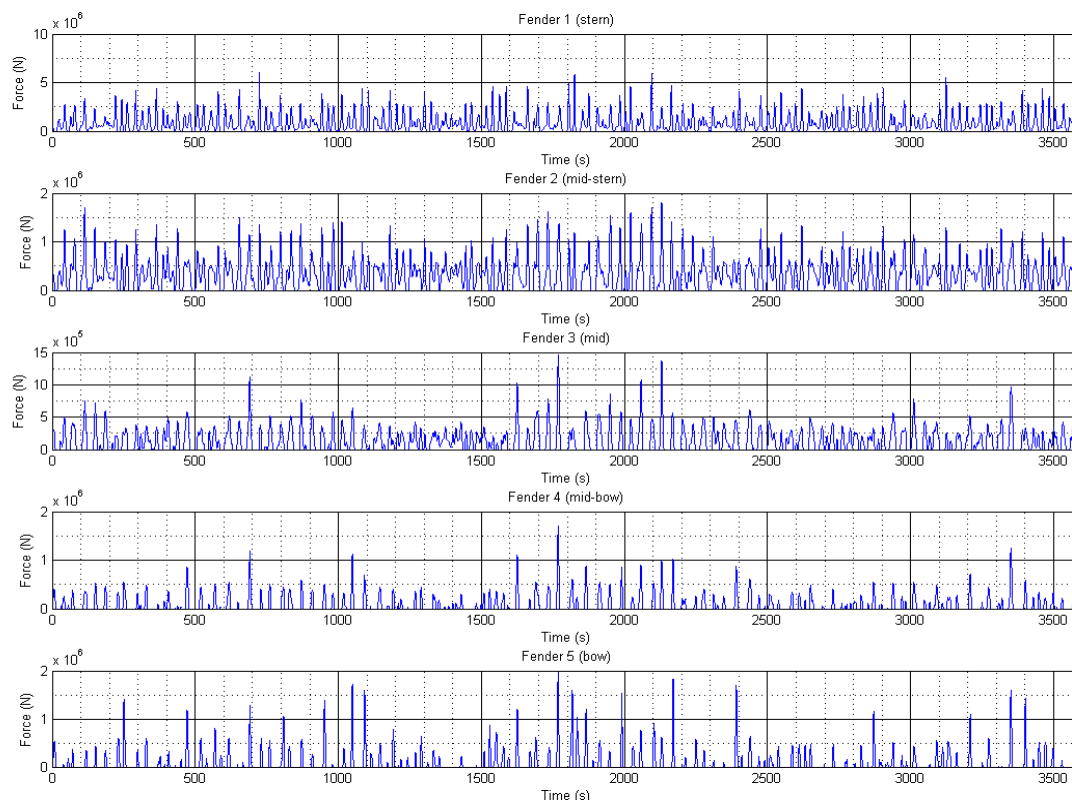


Figure 6.8 – Fender loads for side-by-side operation under loading condition 1, $H_s = 3.5$ m, $T_p = 15.0$ s, wave incidence of 195° and mooring arrangement 8-4-6.

In Figure 6.7 the XY positions of both the VLCC and the shuttle tanker are presented. It may be noticed that the trajectories are not parallel to the X-axis, but instead slightly deviated to East due to the wind and mean drift loads affecting the ships from Northwest. Figure 6.8 shows the loads in the fenders elements. It is clear that the astern elements are the most solicited, meaning that shocks are mostly present in this portion of both ships. The bow elements, in the other hand, are sometimes even not compressed.

Figure 6.9 depicts the mooring traction loads on the four groups of lines, viz., bow, fore manifold, aft manifold and stern. It may be observed that the service working load is exceeded in bow lines, which means that other mooring arrangement should be adopted under the simulated environmental and loading conditions. Loads in mooring ropes are highly influenced by the ships relative roll and pitch motions. Figure 6.10 shows the angular motions for both vessels. For roll (ϕ) motions it is interesting to point out the difference in periods for the ballasted VLCC and the full loaded shuttle tanker.

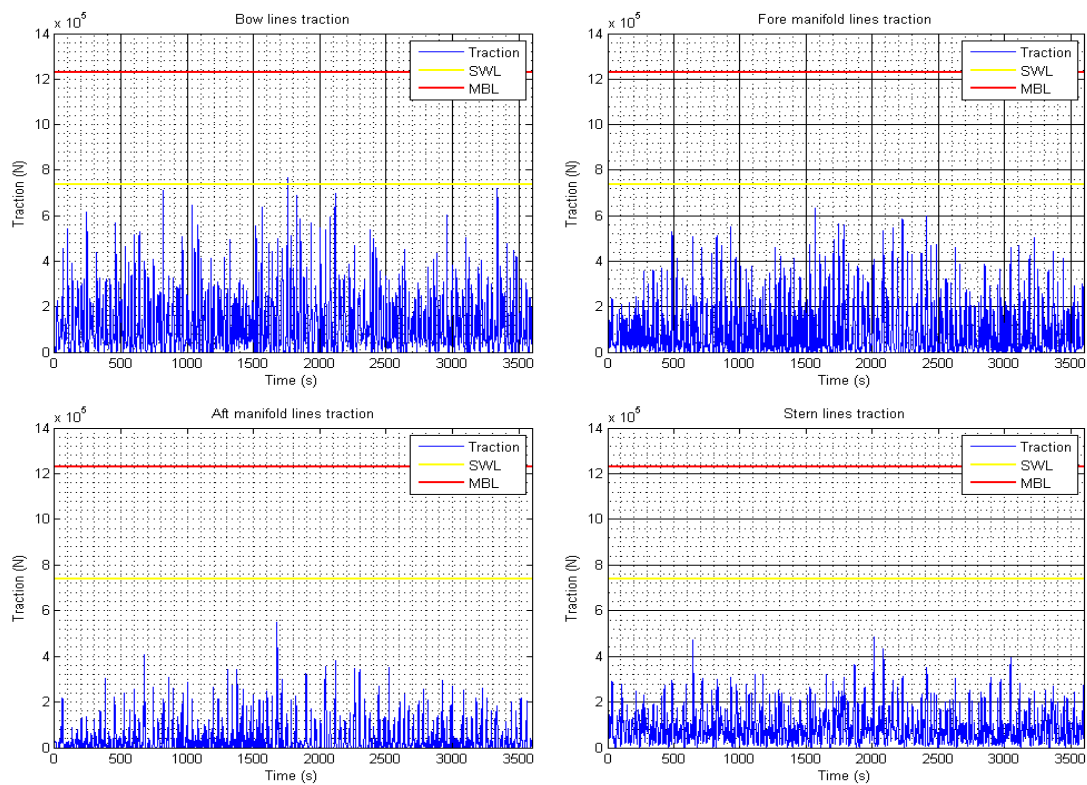


Figure 6.9 – Traction in mooring lines for side-by-side operation under loading condition 1, $H_s = 3.5$ m, $T_p = 15.0$ s, wave incidence of 195° and mooring arrangement 8-4-6.

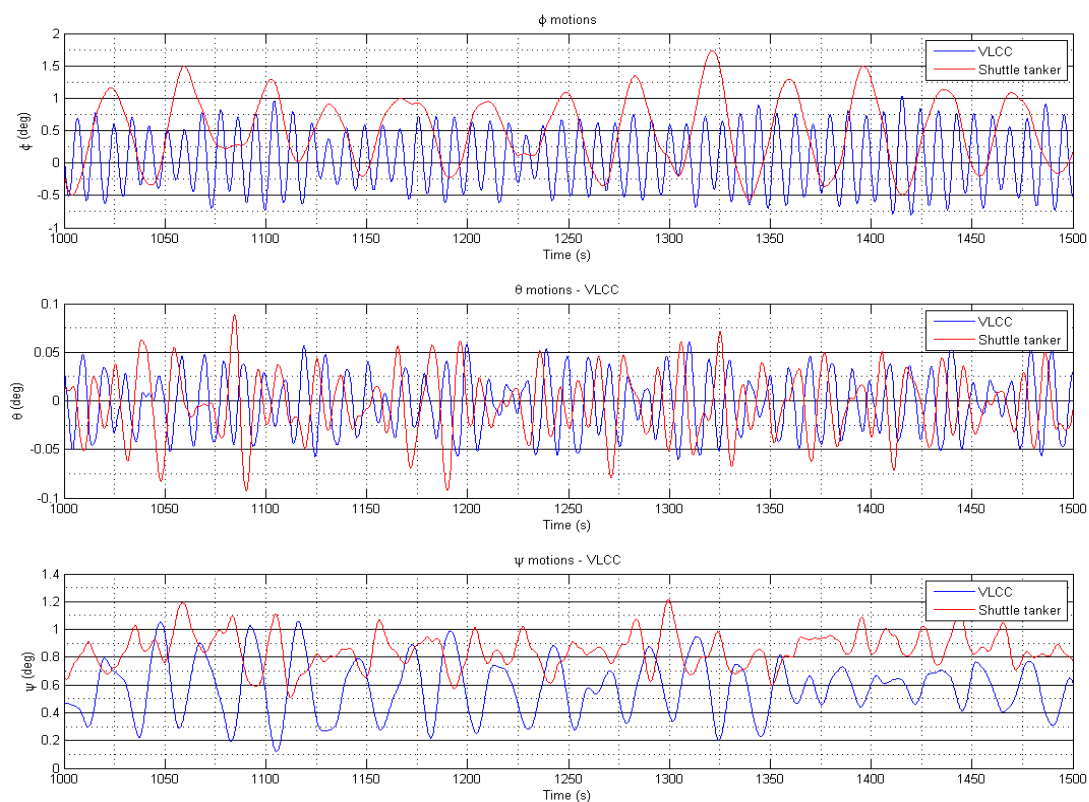


Figure 6.10 – Roll, pitch and yaw motions for side-by-side operation under loading condition 1, $H_s = 3.5$ m, $T_p = 15.0$ s, wave incidence of 195° and mooring arrangement 8-4-6.

The main objective of the simulations is to monitor the traction in lines and verify if they exceed the assigned values for the SWL and the MBL. Therefore, diagrams inspired in (OCIMF, 2005) were created for each 3 X 3 set of wave heights and peak periods, corresponding to a given loading condition, mooring arrangement and wave incidence direction. In these graphs, a green rectangle means that the operation occurred without problems in mooring lines, that is, none of the lines exceeded the SWL. A yellow rectangle indicates that at least one line exceeded the SWL but not the MBL, so that it did not break. If the rectangle is red, however, it means that at least one mooring rope broke during the operation. Finally, a black rectangle means that an instability problem stopped the simulation.

Figures 6.11 and 6.12 refer to loading condition 1, with mooring arrangement 8-4-6 and wave incidence of 195° and 315° , respectively. According to the diagrams, waves affecting ships in the bow led the traction to exceed the SWL under waves of significant height of 3.5 m and peak period of 15.0 s, while those affecting from sterns caused rupture in the lines with the same values for H_s and T_p . The results were similar under the same loading and environmental conditions, but with mooring arrangement 8-4-4, except for the fact that at 195° the SWL was not crossed (Figures 6.13 and 6.14). It may seem weird that an arrangement with fewer ropes yields a more safe behavior, but this may be explained in terms of changes on the resultant stiffness of the mass-spring-damper system composed by the ships, mooring ropes and potential damping. In fact, by comparison between Figures 6.10 and 6.15 it may be noticed that in the former case the shuttle tanker roll amplitude is higher, an indication that the system behavior visibly changes according to the adopted mooring arrangement. This fact, however, did not prevent mooring lines to disrupt under 315° incident waves.

		Cond. 1 - Incid. = 195° - Moor. 8-4-6		
Hs (m)	1.5			
	2.5			
	3.5			
		8.0	11.5	15.0
		Tp (s)		

Figure 6.11 – Mooring system conditions for side-by-side operation under loading condition 1, wave incidence of 195° and mooring arrangement 8-4-6.

		Cond. 1 - Incid. = 315° - Moor. 8-4-6		
Hs (m)	1.5			
	2.5			
	3.5			
		8.0	11.5	15.0
		Tp (s)		

Figure 6.12 – Mooring system conditions for side-by-side operation under loading condition 1, wave incidence of 315° and mooring arrangement 8-4-6.

		Cond. 1 - Incid. = 195° - Moor. 8-4-4		
Hs (m)	1.5			
	2.5			
	3.5			
		8.0	11.5	15.0
		Tp (s)		

Figure 6.13 – Mooring system conditions for side-by-side operation under loading condition 1, wave incidence of 195° and mooring arrangement 8-4-4.

		Cond. 1 - Incid. = 315° - Moor. 8-4-4		
Hs (m)	1.5			
	2.5			
	3.5			
		8.0	11.5	15.0
		Tp (s)		

Figure 6.14 – Mooring system conditions for side-by-side operation under loading condition 1, wave incidence of 315° and mooring arrangement 8-4-4.

In the 6-4-4 arrangement, however, even with 315° (Figure 6.17) waves the mooring system did not break, but just crossed the SWL. Besides, as in the 8-4-4 case, operations at 195° incident waves (Figure 6.16) did not face any problem for neither of the wave height – peak period combinations.

Under loading condition 2, mooring arrangement 8-4-6 did not present incidents in mooring lines under 195° waves (Figure 6.18) and all the considered combinations of wave height and peak period. However, with ships subjected to 315° incident waves (Figure 6.19) ropes rupture occurred for both 2.5 m and 3.5 m significant wave heights, combined with 15.0 s wave periods.

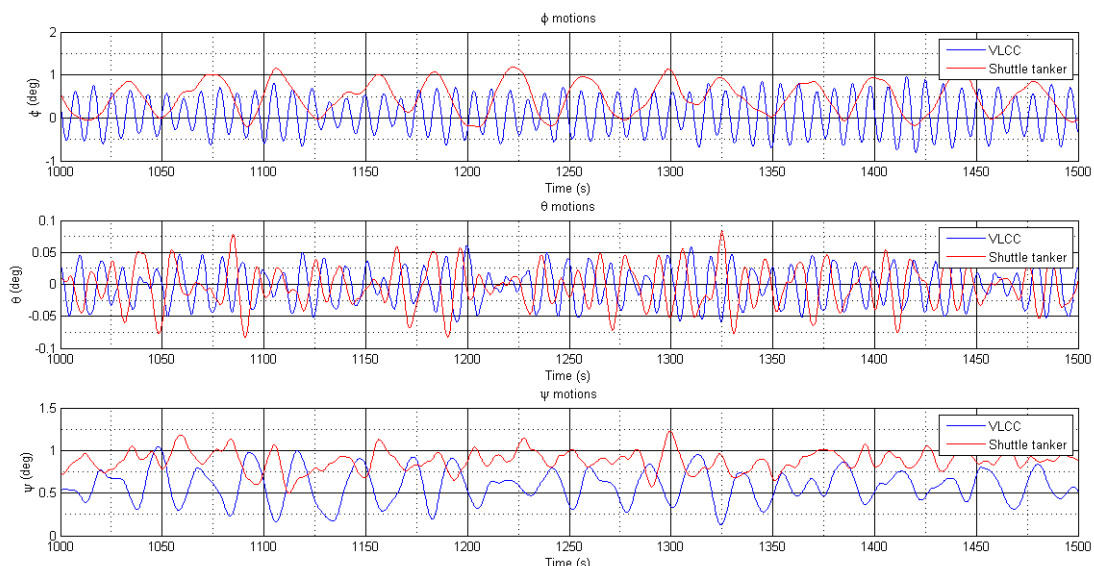


Figure 6.15 – Roll, pitch and yaw motions for side-by-side operation under loading condition 1, Hs = 3.5 m, Tp = 15.0s, wave incidence of 195° and mooring arrangement 8-4-4.

		Cond. 1 - Incid. = 195° - Moor. 6-4-4		
Hs (m)	1.5			
	2.5			
	3.5			
		8.0	11.5	15.0
		Tp (s)		

Figure 6.16 – Mooring system conditions for side-by-side operation under loading condition 1, wave incidence of 195° and mooring arrangement 6-4-4.

		Cond. 1 - Incid. = 315° - Moor. 6-4-4		
Hs (m)	1.5			
	2.5			
	3.5			
		8.0	11.5	15.0
		Tp (s)		

Figure 6.17 – Mooring system conditions for side-by-side operation under loading condition 1, wave incidence of 315° and mooring arrangement 6-4-4.

		Cond. 2 - Incid. = 195° - Moor. 8-4-6		
Hs (m)	1.5			
	2.5			
	3.5			
		8.0	11.5	15.0
		Tp (s)		

Figure 6.18 – Mooring system conditions for side-by-side operation under loading condition 2, wave incidence of 195° and mooring arrangement 8-4-6.

		Cond. 2 - Incid. = 315° - Moor. 8-4-6		
Hs (m)	1.5			
	2.5			
	3.5			
		8.0	11.5	15.0
		Tp (s)		

Figure 6.19 – Mooring system conditions for side-by-side operation under loading condition 2, wave incidence of 315° and mooring arrangement 8-4-6.

A similar behavior was observed for mooring arrangement 8-4-4, as indicated in Figures 6.20 and 6.21. When the 6-4-4 lines combination was adopted, however, the behavior for 195° waves (Figure 6.22) was still the same, but under 315° waves (Figure 6.23) lines did not disrupt for $H_s = 2.5$ m and $T_p = 15.0$ s.

		Cond. 2 - Incid. = 195° - Moor. 8-4-4		
Hs (m)	1.5			
	2.5			
	3.5			
		8.0	11.5	15.0
		Tp (s)		

Figure 6.20 – Mooring system conditions for side-by-side operation under loading condition 2, wave incidence of 195° and mooring arrangement 8-4-4.

		Cond. 2 - Incid. = 315° - Moor. 8-4-4		
Hs (m)	1.5			
	2.5			
	3.5			
		8.0	11.5	15.0
		Tp (s)		

Figure 6.21 – Mooring system conditions for side-by-side operation under loading condition 2, wave incidence of 315° and mooring arrangement 8-4-4.

		Cond. 2 - Incid. = 195° - Moor. 6-4-4		
Hs (m)	1.5			
	2.5			
	3.5			
		8.0	11.5	15.0
		Tp (s)		

Figure 6.22 – Mooring system conditions for side-by-side operation under loading condition 2, wave incidence of 195° and mooring arrangement 6-4-4.

		Cond. 2 - Incid. = 315° - Moor. 6-4-4		
Hs (m)	1.5			
	2.5			
	3.5			
		8.0	11.5	15.0
		Tp (s)		

Figure 6.23 – Mooring system conditions for side-by-side operation under loading condition 2, wave incidence of 195° and mooring arrangement 6-4-4.

For loading condition 3, all simulations involving 8.0 s period waves failed in producing results. For other periods, however, simulations resulted similar for all mooring arrangements, with variations only in terms of wave incidence direction. In fact, for 195° incidence the SWL was only exceeded for the extreme combination of 3.5 m wave height and 15.0 s peak period, while for 315° waves the SWL and MBL limits were surpassed for $H_s = 2.5$ m and $H_s = 3.5$ m, respectively, under $T_p = 15.0$ s. The results are in Figures 6.24 to 6.29.

		Cond. 3 - Incid. = 195° - Moor. 8-4-6		
Hs (m)	1.5			
	2.5			
	3.5			
		8.0	11.5	15.0
		Tp (s)		

Figure 6.24 – Mooring system conditions for side-by-side operation under loading condition 3, wave incidence of 195° and mooring arrangement 8-4-6.

		Cond. 3 - Incid. = 315° - Moor. 8-4-6		
Hs (m)	1.5			
	2.5			
	3.5			
		8.0	11.5	15.0
		Tp (s)		

Figure 6.25 – Mooring system for side-by-side operation under loading condition 3, wave incidence of 315° and mooring arrangement 8-4-6.

		Cond. 3 - Incid. = 195° - Moor. 8-4-4		
Hs (m)	1.5			
	2.5			
	3.5			
		8.0	11.5	15.0
		Tp (s)		

Figure 6.26 – Mooring system conditions for side-by-side operation under loading condition 3, wave incidence of 195° and mooring arrangement 8-4-4.

		Cond. 3 - Incid. = 315° - Moor. 8-4-4		
Hs (m)	1.5	8.0	11.5	15.0
	2.5			
	3.5			
		8.0	11.5	15.0
		Tp (s)		

Figure 6.27 – Mooring system conditions for side-by-side operation under loading condition 3, wave incidence of 315° and mooring arrangement 8-4-4.

		Cond. 3 - Incid. = 195° - Moor. 6-4-4		
Hs (m)	1.5	8.0	11.5	15.0
	2.5			
	3.5			
		8.0	11.5	15.0
		Tp (s)		

Figure 6.28 – Mooring system conditions for side-by-side operation under loading condition 3, wave incidence of 195° and mooring arrangement 6-4-4.

		Cond. 3 - Incid. = 315° - Moor. 6-4-4		
Hs (m)	1.5	8.0	11.5	15.0
	2.5			
	3.5			
		8.0	11.5	15.0
		Tp (s)		

Figure 6.29 – Mooring system conditions for side-by-side operation under loading condition 3, wave incidence of 195° and mooring arrangement 6-4-4.

Simulations were also executed for loading condition 4, but crashes occurred for all combinations of wave parameters and mooring arrangements. In fact, it was not possible to obtain reasonable hydrodynamic data for ships under interaction in the referent combination of drafts, leading to unreal values for added mass and potential damping. Therefore, conclusions about the mooring system integrity could not be drawn for the fourth loading condition.

6.2 CONVOY

Each convoy simulation lasted 3600 s, during which the VLCC had to follow a straight trajectory for 1500s, perform a 10° curve to starboard and stabilize again in the new heading. Meanwhile, the shuttle tanker had to keep its bow aligned with the VLCC midship – in order to keep manifolds in the same line –, with a lateral separation of 70 m. The main objective was to observe the ability of the shuttle tanker to keep the specified relative position to the VLCC and

perform the curve – under different combinations of environmental and loading conditions – without hose disconnection. The VLCC nominal velocity was set to 5 knots.

6.2.1 Shuttle tanker actuators properties

In opposition to the side-by-side case, feasibility of convoy operations is highly influenced by the shuttle tanker actuators dynamics and constraints. Therefore, adoption of realistic values in the simulator is an important step towards reproducing the actual adversities faced by the ship to follow the VLCC under a given combination of loading and environmental conditions.

Since rudder deflection δ_r is considered as an input in the adopted model of hydrodynamic derivatives, it is necessary to employ the relations developed in section 5.3 in order to connect the yaw moment demanded by the controller to the commanded rudder angle. The rudder main properties are listed on Table 6.6.

Table 6.6 – Main properties of the shuttle tanker rudder.

Parameter	Value
Height – h_r	11.1 m
Area – A_r	42.2 m ²
Mean chord – c_m	3.8 m
Geometric aspect ratio – Λ_g	2.9
Effective aspect ratio – Λ	3.8
Deflection range	-35°/+35°
Maximum deflection rate – $\dot{\delta}_{max}$	2.3°/s

Substituting the given value for Λ in equation (5.37):

$$C_L(\delta_r) = 3.55 \sin(\delta_r) + \sin(\delta_r) |\sin(\delta_r)| \cos(\delta_r) \quad (6.7)$$

Making the linear approximation of (5.41):

$$C_L(\delta_r) \approx 3.82\delta_r \quad (6.8)$$

The original and approximated curves for $C_L(\delta_r)$ are plotted in Figure 6.29. Considering a propeller diameter D_p of 7.7 m and the rudder properties value

given in Table 6.6, the commanded rudder deflection δ_c may be calculated departing from equations (5.40) and (5.43). The deflection rate is then calculated according to:

$$\dot{\delta}_r = \frac{\delta_c - \delta_r}{\Delta t} \quad (6.9)$$

where Δt is the time step adopted for the simulation. Finally, $\dot{\delta}_r$ is limited by the rudder maximum deflection rate:

$$\dot{\delta}_r = \begin{cases} \min(\dot{\delta}_r, \dot{\delta}_{max}), & \text{for } \dot{\delta}_r > 0 \\ \max(\dot{\delta}_r, -\dot{\delta}_{max}), & \text{for } \dot{\delta}_r < 0 \end{cases} \quad (6.10)$$

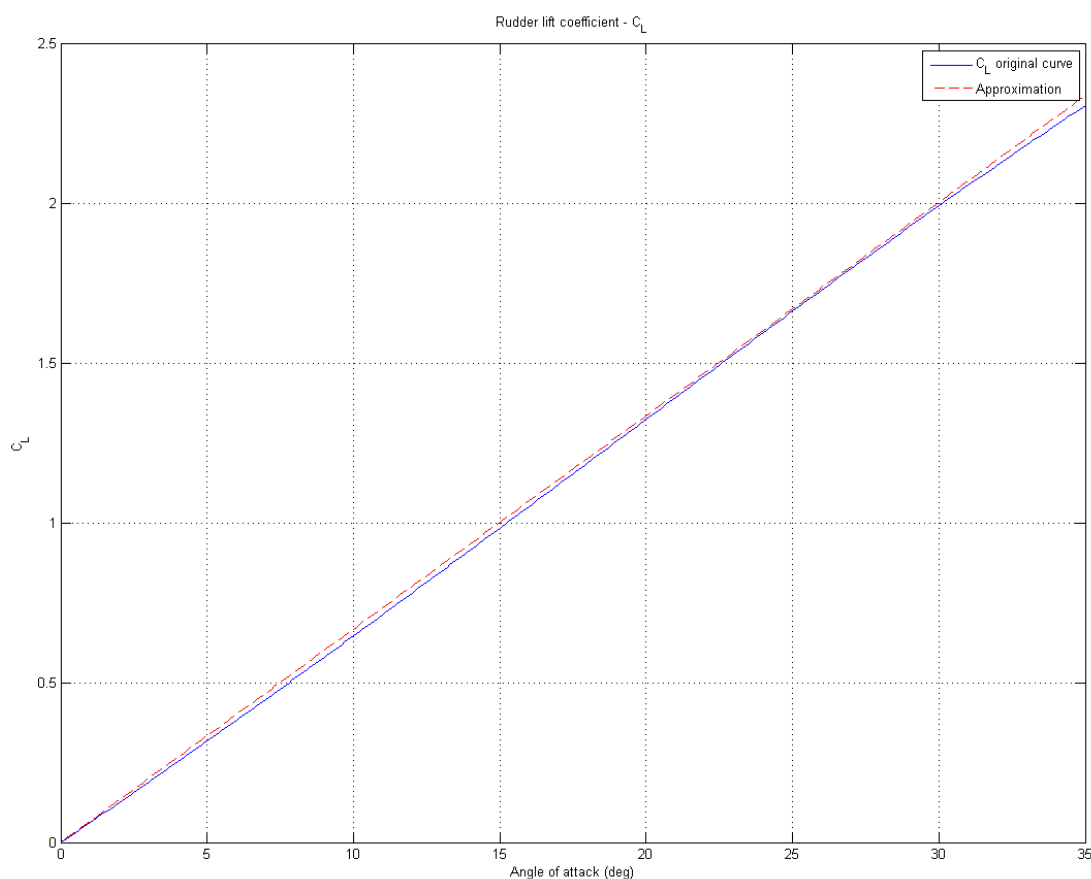


Figure 6.30 – Rudder lift coefficient for the shuttle tanker.

As also mentioned in section 5.3, the only concern related to the thruster dynamics was to limit the maximum and minimum deliverable thrusts, as stated on equation (5.35). For a tanker with the dimensions presented on Table 6.2, typical values for T_{max} and T_{min} are 1207 kN and -540 kN, respectively (MORATELLI JR., 2010).

6.2.2 Environmental action

The environmental conditions considered for the side-by-side simulations are not necessarily the most relevant for the convoy operations. While in the former case wave length has a critical connection to the mooring system response, in the latter the concern is mostly directed for loads that may hamper the shuttle tanker ability to follow the VLCC. In this sense, stern waves were not considered, while the ships responses to a larger incidence angle were tested.

The wave parameters of Table 6.7 were adopted for the convoy operation simulations. Wave motions were considered by superposition of low- and wave-frequency motions, according to the procedure on Figure 2.9. Wind velocity was set to 7.7 m/s and the direction was always coincident to waves, but simulations without wind were also executed in order to evaluate the influence of this load on the shuttle tanker controllability for the different ships loading conditions. As in the side-by-side case, it was decided not to consider ocean current in the simulations.

Table 6.7 – Waves parameters for the convoy simulations.

Parameter	Values
Significant height – H_s	1.5 m / 3.5 m
Peak period – T_p	8.0 s / 11.5 s
Incidence – β_{waves}	120° / 195°

6.2.3 Simulations results

All combinations of environmental and loading conditions were simulated, leading to a total of 48 executions. The criteria established to evaluate the operation safety under a given condition were hose disconnection – that may be caused if the shuttle tanker loses its ability to follow the VLCC – and risk of collision.

Figure 6.31 illustrates the definitions of the distance between manifolds D_{mf} and of the separation distance y_{sep} . For a given hose length l_h , it was considered that a disconnection occurred if $D_{mf} > l_h$ for any instant of the operation. Besides, a collision was detected always that $y_{sep} \leq y_{min}$ was verified, for a given value of the minimum safe distance y_{min} .

Since the nominal separation distance y_{sep} was assigned to 70 m and the shuttle tanker beam measures 46 m, the desired value for D_{mf} was $70 + 46/2 = 93$ m. Then, a 200 m hose length l_h was considered, leading to a clearance of 107 m. The choice for y_{min} should take into account the possibility of suction interaction loads as those presented on section 4.1.1. Again, the lack of a reliable model for the correspondent configuration prevents a rational definition of a value for y_{min} , so that an arbitrary $y_{min} = \frac{y_{sep}}{2} = 35$ m was assigned for analyses of the simulations results.

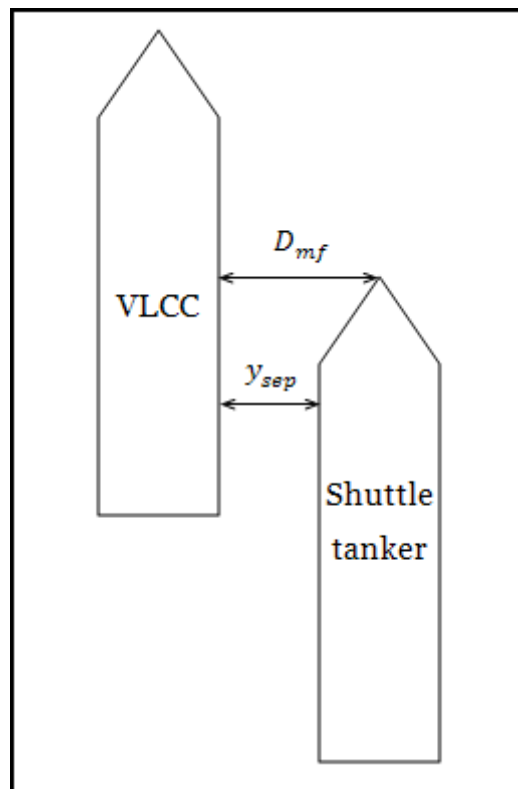


Figure 6.31 – Distance between manifolds D_{mf} .

Figure 6.32 shows the XY positions of both ships during a simulation under loading condition 1 and absence of wind loads. Wave significant height is set to 1.5 meters, peak period to 8.0 seconds and incidence to 195° . The relatively calm weather conditions allow the operation to be carried out without difficulties, as it may be noticed by analysis of Figure 6.33, which depicts the distance between manifolds, its longitudinal component and the separation y_{sep} . The highest value reached by D_{mf} was 135 m, while y_{sep} was always above 64 m. Then, neither hose disconnection nor collision were observed.

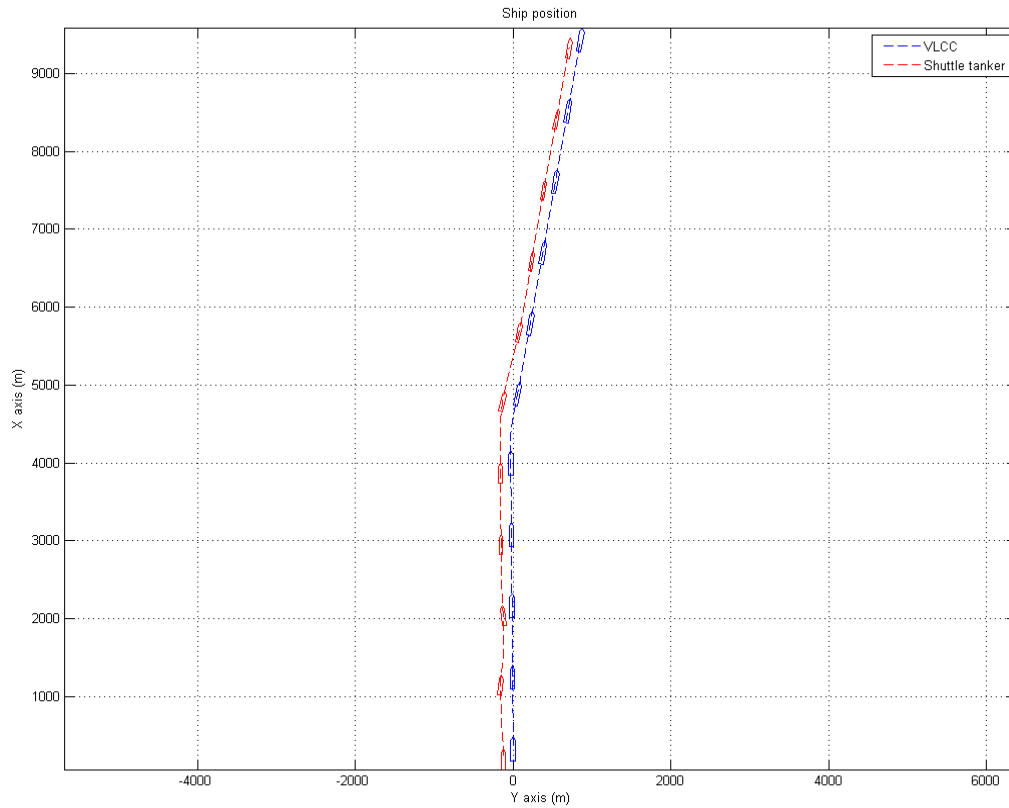


Figure 6.32 – XY positions for convoy operation under loading condition 1, $H_s = 1.5\text{m}$, $T_p = 8.0\text{s}$, wave incidence 195° and no wind loads.

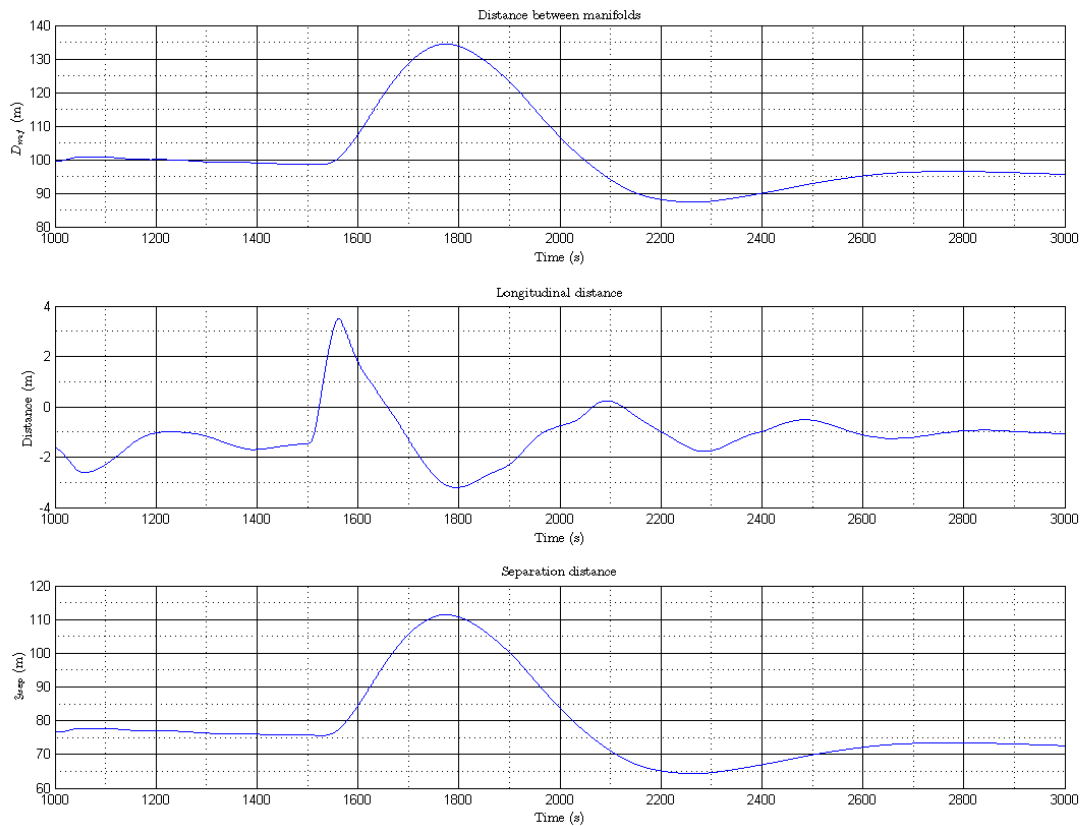


Figure 6.33 – Distance between manifolds for convoy operation under loading condition 1, $H_s = 1.5\text{m}$, $T_p = 8.0\text{s}$, wave incidence 195° and no wind loads.

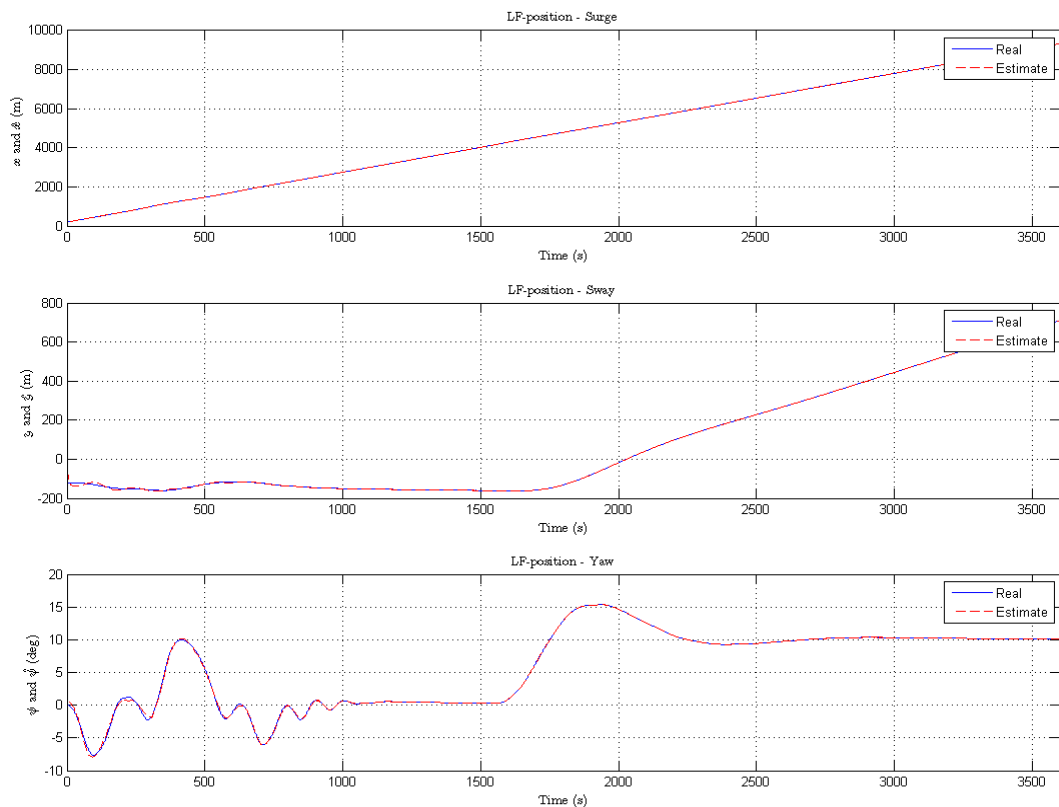


Figure 6.34 – Low-frequency estimates for convoy operation under loading condition 1, $H_s = 1.5\text{m}$, $T_p = 8.0\text{s}$, wave incidence 195° and no wind loads.

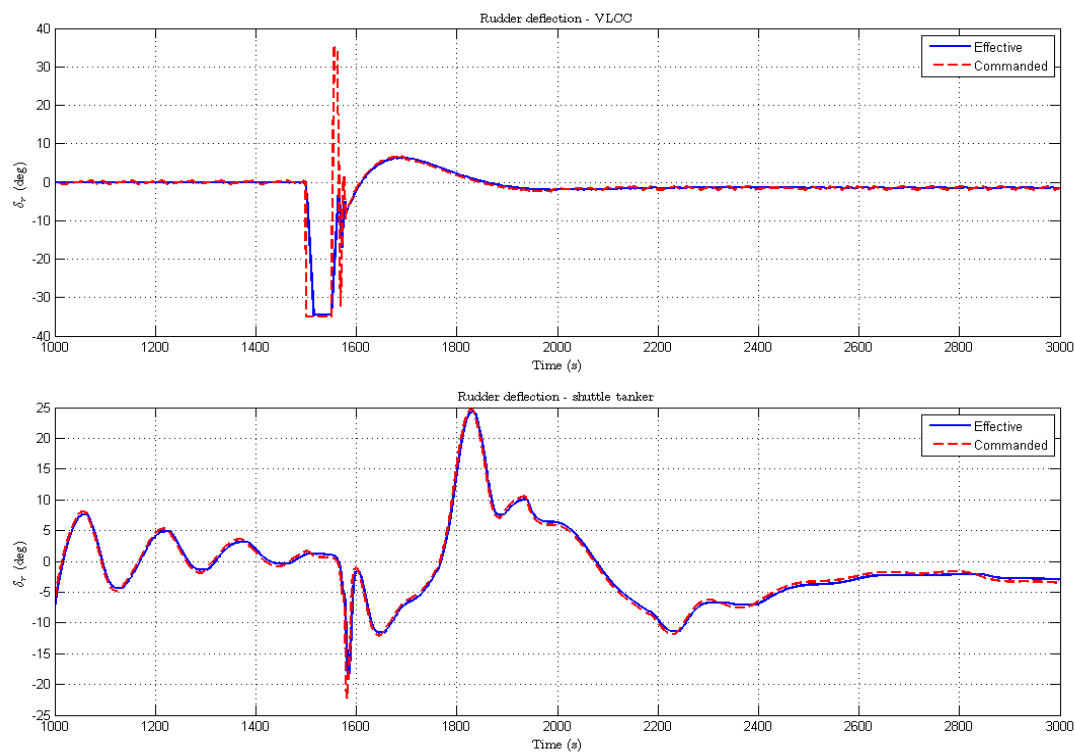


Figure 6.35 - Rudder commanded and effective deflection for convoy operation under loading condition 1, $H_s = 1.5\text{m}$, $T_p = 8.0\text{s}$, wave incidence 195° and no wind loads.

In Figure 6.34 both the real and estimated shuttle tanker low-frequency motions are depicted. It may be noticed that the observer could cope well in following the real ship movement, which is important in sense of feeding the controller with a proper signal. In Figure 6.35 the rudder commanded and effective deflections are plotted. Analysis of the curve correspondent to the VLCC shows that the rudder dynamics prevent the deflection to follow excessive modulation induced by the controller. For the shuttle tanker, in the other hand, it may be noticed that the controller is more sensitive to the ship dynamics, since the rudder is not saturated at any moment.

Diagrams similar to those presented in the side-by-side case are shown illustrating whether the convoy operations were or not safe, following the mentioned criteria of hose disconnection (yellow rectangle) and collision risk (red rectangle). Again, a green rectangle means that the operation was carried out without problems. From Figure 6.36, for example, it may be noticed that in presence of wind and under incidence direction of 120° , with ships loaded according to condition 1, hose disconnection was noticed for higher waves. The same, however, did not occur in absence of wind, which led to safe operations irrespective of wave height, as indicated in Figure 6.37.

Hs (m)		Cond. 1 - Incid. = 120° - Wind = 1	
		1.5	
3.5			
		8.0	11.5
		Tp (s)	

Figure 6.36 – Results for convoy operation under loading condition 1, wave incidence of 120° and in presence of wind.

Hs (m)		Cond. 1 - Incid. = 120° - Wind = 0	
		1.5	
3.5			
		8.0	11.5
		Tp (s)	

Figure 6.37 – Results for convoy operation under loading condition 1, wave incidence of 120° and in absence of wind.

The controllability is improved under less oblique waves and wind, as indicated in Figures 6.38 and 6.39. In fact, it may be noticed that operations were successful for every combination of wave height and period, with or without wind.

		Cond. 1 - Incid. = 195° - Wind = 1	
Hs (m)	1.5		
	3.5		
		8.0	11.5
		Tp (s)	

Figure 6. 38 – Results for convoy operation under loading condition 1, wave incidence of 195° and in presence of wind.

		Cond. 1 - Incid. = 195° - Wind = 0	
Hs (m)	1.5		
	3.5		
		8.0	11.5
		Tp (s)	

Figure 6.39 – Results for convoy operation under loading condition 1, wave incidence of 195° and in absence of wind.

For loading condition 2, however, the risk of a collision considerably increases, as it may be noticed through analysis of Figures 6.40 and 6.41. The increase in the shuttle tanker freeboard elevates the amplitude of wind loads, hampering the ship ability of following the VLCC. Besides, the lighter ship becomes more vulnerable to the action of mean drift loads, such that even in absence of wind the risk of a collision is highly increased for wave incidence of 120°. For incidence direction of 195°, however, the risks are decreased. In fact, in presence of wind collision risk was observed only in combination with 3.5 m waves, while in simulations without wind action the operation did not present difficulties for neither of the environmental combinations (Figures 6.42 and 6.43).

		Cond. 2 - Incid. = 120° - Wind = 1	
Hs (m)	1.5		
	3.5		
		8.0	11.5
		Tp (s)	

Figure 6.40 – Results for convoy operation under loading condition 2, wave incidence of 120° and in presence of wind.

		Cond. 2 - Incid. = 120° - Wind = 0	
Hs (m)	1.5		
	3.5		
		8.0	11.5
		Tp (s)	

Figure 6.41 – Results for convoy operation under loading condition 2, wave incidence of 120° and in absence of wind.

		Cond. 2 - Incid. = 195° - Wind = 1	
Hs (m)	1.5		
	3.5		
		8.0	11.5
		Tp (s)	

Figure 6.42 – Results for convoy operation under loading condition 2, wave incidence of 195° and in presence of wind.

		Cond. 2 - Incid. = 195° - Wind = 0	
Hs (m)	1.5		
	3.5		
		8.0	11.5
		Tp (s)	

Figure 6.43 – Results for convoy operation under loading condition 2, wave incidence of 195° and in absence of wind.

Loading conditions 3 and 4 are the same as 1 and 2 for the shuttle tanker, but different for the VLCC. The difference in freeboard increases the response of the VLCC to both wind and waves, influencing in its ability of course keeping. – and, consequently, in the shuttle tanker behavior. Figures 6.44 and 6.45 present the results for loading condition 3 and incidence direction of 120°. Comparing with condition 1 one may notice that the risk of hose disconnection gives place to danger of collision. It is interesting to notice that this danger increases when wind is disregarded. This is not surprising, since the VLCC at ballast condition presents a very large freeboard and, therefore, is subjected to higher influence of wind than that experimented by the shuttle tanker. Since the wind reaches ships from the shuttle tanker side,

prevent collisions by repulsing one ship from another. The same effect, however, is not so significant at a lower incidence angle, as one may observe in Figures 6.46 and 6.47.

		Cond. 3 - Incid. = 120° - Wind = 1	
Hs (m)	1.5		
	3.5		
		8.0	11.5
		Tp (s)	

Figure 6.44 – Results for convoy operation under loading condition 3, wave incidence of 120° and in presence of wind.

		Cond. 3 - Incid. = 120° - Wind = 0	
Hs (m)	1.5		
	3.5		
		8.0	11.5
		Tp (s)	

Figure 6.45 – Results for convoy operation under loading condition 3, wave incidence of 120° and in absence of wind.

		Cond. 3 - Incid. = 195° - Wind = 1	
Hs (m)	1.5		
	3.5		
		8.0	11.5
		Tp (s)	

Figure 6.46 – Results for convoy operation under loading condition 3, wave incidence of 195° and in presence of wind.

		Cond. 3 - Incid. = 195° - Wind = 0	
Hs (m)	1.5		
	3.5		
		8.0	11.5
		Tp (s)	

Figure 6.47 – Results for convoy operation under loading condition 3, wave incidence of 195° and in absence of wind.

Finally, under loading condition 4 the operation showed to be unviable for all combinations of wave heights and periods under incidence of 120°, whether in presence or absence of wind (Figures 6.48 and 6.49). Under incidence direction of 195°, in the other hand, operation could be carried out without hose disconnection or collision, irrespective of the waves parameters and wind action, as it may be noticed in Figures 6.50 and 6.51.

		Cond.4 - Incid. = 120° - Wind = 1	
Hs (m)	1.5		
	3.5		
		8.0	11.5
		Tp (s)	

Figure 6.48 – Results for convoy operation under loading condition 4, wave incidence of 120° and in presence of wind.

		Cond. 4 - Incid. = 120° - Wind = 0	
Hs (m)	1.5		
	3.5		
		8.0	11.5
		Tp (s)	

Figure 6.49 – Results for convoy operation under loading condition 4, wave incidence of 120° and in absence of wind.

		Cond. 4 - Incid. = 195° - Wind = 1	
Hs (m)	1.5		
	3.5		
		8.0	11.5
		Tp (s)	

Figure 6.50 – Results for convoy operation under loading condition 4, wave incidence of 195° and in presence of wind.

		Cond. 4 - Incid. = 195° - Wind = 0	
Hs (m)	1.5		
	3.5		
		8.0	11.5
		Tp (s)	

Figure 6.51 – Results for convoy operation under loading condition 4, wave incidence of 195° and in absence of wind.

7. CONCLUSIONS

Although both operations have the same goal – transfer of oil between two underway ships in open sea –, the theoretical aspects behind their models are considerably different, so that two very distinct problems were approached in this work. In the side-by-side operation the problem was rather focused on the dynamics of coupled floating bodies, while in the convoy case attention was devoted for the development of a refined control approach composed by a nonlinear set of controller and observer, together with a guidance system.

7.1 SIDE-BY-SIDE

The problem of underway coupled ships subjected to waves demands application of the unified model for maneuvering and seakeeping presented on section (2.7.3), which is based on convolution integrals of retardation functions – representing the fluid memory effects – in order to make possible the consideration of non-zero frequency loads in the equations of motions. In this sense, one of the contributions of this work is the application of this approach to the modeling of underway side-by-side operations, together with models for other relevant loads like those induced by fenders and mooring system.

It was frustrating that stability problems faced during the simulations prevented the achievement of outcomes correspondent to the derived model, so that the results presented on Chapter 6 are actually based on an approximation of this model. However, the process of understanding the necessary theoretical background and applying it in a practical problem were indeed the highest profit along the development of this work.

In fact, the notion of considering fluid memory effects in the equations of motions for a floating body is extensible for a broad range of practical applications where two or more bodies share common loads. Besides, it provides a rather physical comprehension of the response of a ship to waves than the traditional practice of superposing low- and wave-frequency motions derived from separate models. The difference becomes clear if one considers, for example, a ship oscillating in pitch. If the ship is asymmetric in the yz -plane, the waves radiated by the bow are different from those produced by the stern motions, so that the resultant in the x direction is not zero, leading to a

displacement in surge. This effect is not preserved by the superposition method, since the radiation loads for non-zero frequency motions are not considered in the body dynamics.

Analysis of the side-by-side simulations outputs allows some general conclusions to be drawn. Firstly, irrespective of the loading case the values for the SWL and the MBL assigned for mooring lines were only exceeded for the 15.0s peak period waves. This means that longer waves have more influence on ships motions and, consequently, on the mooring system loads. Wave incidence direction also showed to be determinant for the integrity of the mooring ropes. The effects presented to be more intense for waves reaching the ships from stern than those from bow.

An interesting conclusion relates to the different mooring arrangements tested in the simulations. In spite of presenting a lower number of lines, the 6-4-4 arrangement showed to be safer than the 8-4-6 and 8-4-4 arrangements. This may be explained in terms of the resultant stiffness of the mooring system, which has influence on the natural frequency of oscillation of the coupled ships.

7.2 CONVOY

Modeling of convoy operation was based on a less sophisticated approach for expressing the ships dynamics. The autopilot, however, was based on modern nonlinear solutions for the observer and controller, together with a guidance system particularly designed for the task.

The line-of-sight approach was adopted for generation of heading references for the controller, while a strategy for waypoints generation was developed as to make the shuttle tanker to keep a given distance to the VLCC. The surge velocity reference was determined with basis on comparison between the actual and desired longitudinal distances, resembling solutions of cooperative control. The resultant guidance system could be adapted for a more ample class of problems involving control of unmanned vehicles.

Simulations showed a strong dependence of the loading conditions on the occurrence of hose disconnections and risk of collisions. The freeboard highly influenced the controllability of the shuttle tanker, mainly under action of oblique waves and, mostly important, wind. In fact, the ship under ballast

condition presents a higher area above water level, so that wind loads become more pronounced. Besides, the lower ship displacement makes the vessel more susceptible to the action of both wave mean drift and wind loads, increasing the necessary control loads to properly follow the VLCC.

In this sense, it was observed that under loading conditions 2 and 4 – those correspondent to the ballasted shuttle tanker – the operation became unviable for 120° waves and wind. Since these conditions refer to the end of those operations initiated at conditions 1 and 3, respectively, the conclusion is that the *whole* transfer processes are unpractical for the mentioned angle of incidence. By diminishing the incidence direction, however, the risk of disconnections and collisions significantly decreases. In this case, lack of safety was only observed for condition 2 under 3.5 m significant height waves, irrespective of the peak period.

7.3 FINAL CONSIDERATIONS AND RECOMMENDATIONS FOR FUTURE WORK

As already mentioned, this work approached two problems linked by a common final objective, but of very distinct nature in theoretical terms. It is true that it could be more fruitful to focus in one of the operations and develop a deeper and more specific study on its peculiarities. However, the decision to deepen in different issues becomes more understandable if one considers that the primary aim of the research was to propose models for two alternatives for oil transfer between underway tankers.

Also, by introducing a wide range of topics this work proposes a variety of further research themes. Certainly, investigations on the instabilities verified on the side-by-side case would yield helpful advances on the matter of using the state-space approximation of the convolution terms in the equations of motions. Besides, a theoretical understanding on the wave hydrodynamic interactions is essential to explain the fluid behavior between hulls, while experiments with scale models are mandatory for a rational adjustment of the lid method presented on Chapter 4.

For the convoy case, it would be interesting to test different control strategies than those approached on this work. Besides, adoption of the so-called high-lift

rudders could improve the shuttle tanker maneuvering skills, leading to more safe operations. Controllability could also be enhanced by usage of the shuttle tanker azimuthal thruster, if available. Improvement of the proposed guidance system could also render more satisfactory results than those obtained in this work. It could be profitable, for example, to determine different criteria for way-points generation in terms of the environmental conditions. Finally, studies on the possible suction effects, in the sense of assigning a rational criterion for collision risk, would aggregate a rather scientific character to the analysis.

REFERENCES

- ABKOWITZ, M. A. **Lectures on ship hydrodynamics - steering and maneuverability.** Hydro- and Aerodynamics Laboratory. Lyngby, Denmark, 1964.
- ARANHA, J. A. P. **Second order horizontal steady forces and moment on a floating body with small forward speed.** Journal of Fluid Mechanics, 313, 1996.
- ÅSTRÖM, K. J.; HÄGGLUND, T. **PID Controllers: Theory, Design, and Tuning.** 2. ed. Durham, USA: ISA, 1995.
- BAILEY, P. A.; PRICE, W. G.; TEMAREL, P. **A unified mathematical model describing the maneuvering of a ship travelling in a seaway.** Transactions of the Royal Institution of Naval Architects, 140, pp. 131-139, 1997.
- BERG, T. E.; BAKKE, J. **Ship-to-ship LNG transfer in arctic waters.** Proc. of the ASME 27th International Conference on Offshore Mechanics and Arctic Engineering (OMAE 2008). Estoril, Portugal, 2008.
- BERTRAM, V. **Practical ship hydrodynamics.** Woburn, USA: Butterworth Heinemann, 2000.
- BREIVIK, M. **Nonlinear maneuvering control of underactuated ships.** M.Sc. thesis. Norwegian University of Science and Technology. Trondheim, Norway, 2003.
- BREIVIK, M. **Topics in guided motion control of marine vehicles.** Ph.D. thesis. Norwegian University of Science and Technology. Trondheim, Norway, 2010.
- BREIVIK, M.; HOVSTEIN, V. E.; FOSSEN, T. I. **Straight-line target tracking for unmaned surface vehicles.** Modeling, Identification and Control, 29, n. 4, pp. 131-149, 2008.
- BUCHNER, B.; BUNNIK, T. **Wind shielding investigations for FPSO tandem offloading.** Proc. of The 12th International Offshore and Polar Engineering Conference (ISOPE 2002). Kitakyushu, Japan, 2002.
- BUCHNER, B.; VAN DIJK, A.; DE WILDE, J. **Numerical multiple-body simulations of side-by-side mooring to an FPSO.** Proc. of the 11th International Offshore and Polar Engineering Conference (OMAE 2001). Stavanger, Norway, 2001.
- CHEN, G. R.; FANG, M. C. **Hydrodynamic interactions between two ships advancing in waves.** Ocean Engineering, 28, pp. 1053-1078, 2001.

CUMMINS, W. E. **The impulse response function and ship motions.** David Taylor Model Basin, USA, 1962.

DE DECKER, B. **Ship-ship interaction during lightering operations.** M.Sc. thesis. Gent University, Gent, Belgium, 2006.

DORF, R. C.; BISHOP, R. H. **Modern control systems.** New Jersey, USA: Prentice-Hall, 2001.

EVERGREEN. **Evergreen-marine fenders, pneumatic fenders, airbags, 2011.** Available at: <<http://www.qingdaoyongtai.com/en/>>. Accessed August 6th, 2011.

FALTINSEN, O. M. **Sea loads on ships and offshore structures.** Cambridge, UK: Cambridge University Press, 1990.

FORCE TECHNOLOGY. **Manoeuvring tests with a model of a 258m Suezmax tanker in loaded condition: DMI 2002189.** DMI. Lingby, Denmark, 2002.

FOSSSEN, T. I. **Nonlinear modeling of and control of underwater vehicles.** Ph.D. thesis. Norwegian University of Science and Technology. Trondheim, Norway, 1991.

FOSSSEN, T. I. **Guidance and control of ocean vehicles.** Chichester, England: John Wiley & Sons, 1994.

FOSSSEN, T. I. **Marine Control Systems: Guidance, Navigation and Control of Ships, Rigs and Underwater Vehicles.** Trondheim, Norway: Marine Cybernetics AS, 2002.

FOSSSEN, T. I. **A nonlinear unified state-space model for ship maneuvering and control in a seaway.** International Journal of Bifurcation and Chaos, 15, n. 9, 2005.

FOSSSEN, T. I.; BREIVIK, M.; SKJETNE, R. **Line-of-sight path following of underactuated marine craft.** Proc. of the 6th Conference on Manoeuvring and Control of Marine Crafts (MCMC2003). Girona, Spain, 2003.

FOSSSEN, T. I.; STRAND, J. P. **Passive nonlinear observer design for ships using Lyapunov methods: full-scale experiments with a supply vessel.** Automatica, 35, pp. 3-16, 1999.

FOSSSEN, T.; STRAND, J. P. **Nonlinear ship control.** IFAC Conference on Control Applications in Marine Systems (CAMS'98). Fukuoka, Japan, 1998.

GOLDING, B. K. **Industrial systems for guidance and control of marine surface vessels.** Project assignment performed at the Norwegian University of Science and Technology. Trondheim, Norway, 2004.

HJUSTAD, Å.; KRISTIANSEN, E.; EGELAND, O. **State-space representation of frequency dependent hydrodynamic coefficients.** IFAC Conference on Control Applications in Marine Systems (CAMS 2004). Ancona, Italy, 2004.

HUIJSMANS, R. H.; PINKSTER, J. A.; DE WILDE, J. J. **Diffraction and radiation of waves around side-by-side moored vessels.** Proc. of the 11th International Offshore and Polar Engineering Conference (ISOPE 2001). Stavanger, Norway, 2001.

IEA. **World Energy Outlook 2008.** Paris, France: International Energy Agency, 2008.

INOUE, S.; HIRANO, M.; KIJIMA, K. **Hydrodynamics derivatives on ship maneuvering motion.** Int. Shipbuilding Progress, 28, n. 325, pp. 112-125, 1981.

KAASEN, K. E.; MO, K. **Efficient time-domain model for frequency-dependent added mass and damping.** Proc. of the 23rd Conference on Offshore Mechanics and Arctic Engineering (OMAE2005). Vancouver, Canada, 2005.

KHALIL, H. K. **Nonlinear systems.** Upper Saddle River, USA: Prentice Hall, 2001.

KRISTIANSEN, E.; EGELAND, O. **Frequency-dependent added mass in models for controller design.** IFAC Conf. Maneuvering and Control of Marine Systems (MCMC2003). Girona, Spain, 2003.

KRSTIC, M.; KANELAKOPOULOS, I.; KOKOTOVIC, P. **Nonlinear and Adaptive Control Design.** New York, USA: John Wiley and Sons, 1995.

LEITE, A. J. P. et al. **Current Forces in Tankers and Bifurcation of Equilibrium of Systems: Hydrodynamic Model and Experiments.** Applied Ocean Research, 20, pp. 145-156, 1998.

LEWIS, E. V. **Principles of Naval Architecture: Motions in Waves and Controllability.** Jersey City, USA: Society of Naval Architects & Marine Engineers, 1998.

MÁRQUEZ, H. **Nonlinear control systems: analysis and design.** Hoboken, USA: Wiley-Interscience, 2003.

MCTAGGART, K. et al. **Seakeeping of two ships in close proximity.** Ocean Engineering, 30, pp. 1051-1063, 2003.

MEIROVITCH, L. **Methods of Analytical Dynamics.** New York, USA: McGraw-Hill, 1970.

MORATELLI JR., L. **Principais fatores do projeto de navios aliviadores com sistema de posicionamento dinâmico.** M.Sc. dissertation (in Portuguese). University of São Paulo, São Paulo, Brazil, 2010.

MSS. **Marine Systems Simulator.** Matlab toolbox, 2010. Available at: <<http://www.marinecontrol.org>>. Accessed: May 30th, 2012.

NEWMAN, J. N. **Marine Hydrodynamics.** Cambridge, USA: The MIT Press, 1977.

NORRBIN, N. H. **Theory and observation on the use of a mathematical model for ship manoeuvring in deep and confined waters.** Proc. of the 8th Symposium on Naval Hydrodynamics. Pasadena, USA, 1970.

NYX KNOWLEDGE. **Estudo de desenvolvimento da aplicação de graus generalizados para a simulação de interações hidrodinâmicas entre corpos sujeitos à ação de ondas.** Technical report (in Portuguese). São Paulo, Brazil. 2011.

OCIMF. **Prediction of wind and current loads on VLCCs.** Oil Companies International Marine Forum. London, UK, 1977.

OCIMF. **Ship to ship transfer guide (petroleum).** London, UK: Oil Companies International Marine Forum, 2005.

OGILVIE, T. F. **Recent progress towards the understanding of ship motions.** Proc. of the 5th Symposium on Naval Hydrodynamics, p. 3-79. Bergen, Norway, 1964.

PEREZ, T.; BLANKE, M. **Mathematical ship modeling for control applications.** Technical report. Danish Technical University. Copenhagen, Denmark. 2008.

PEREZ, T.; FOSSEN, T. I. **Kinematic models for manoeuvring and seakeeping of marine vessels.** Modeling, Identification and Control, v. 28, n. 1, pp. 19-30, 2007.

PEREZ, T.; FOSSEN, T. I. **A Matlab toolbox for parametric identification of radiation-force models of ships and offshore structures.** Modeling, Identification and Control, 30, pp. 1-15, 2009.

PEREZ, T.; FOSSEN, T. I.; SØRENSEN, A. **A discussion about seakeeping and manoeuvring models for surface vessels.** Technical report. Norwegian University of Science and Technology. Trondheim, Norway, 2004.

PETROBRAS. **A New Frontier - Petrobras Pre-salt.** Available at: <<http://www.petrobras.com.br/minisite/presal/en/a-new-frontier/>>. Accessed March, 20th, 2012.

QUADVLIEG, F. H. H. A. et al. **Using dynamic positioning for side-by-side cargo transfer operations.** Proc. of the 2nd International Conference on Ship Manoeuvring in Shallow and Confined Water: Ship to Ship Interaction. Trondheim, Norway, 2011.

SAKAKIBARA, S.; YAMADA, S. **Fender selection for reverse lightering operations of ship-to-ship transfer operations.** Proc. of the 27th International Conference on Offshore Mechanics and Arctic Engineering (OMAE 2008). Estoril, Portugal, 2008.

SIMOS, A. N.; TANNURI, E. A.; ARANHA, J. A. P. **A quasi-explicit hydrodynamic model for the dynamic analysis of a moored FPSO under current action.** Journal of Ship Research, 45, n. 4, pp. 289-301, 2001.

SKEJIC, R. **Maneuvering and seakeeping of a single ship and of two ships in interaction.** Ph.D. thesis. Norwegian University of Science and Technology. Trondheim, Norway, 2008.

SKEJIC, R.; FALTINSEN, O. M. **A unified seakeeping and maneuvering analysis of ships in regular waves.** Journal of Marine Science and Technology, 13, pp. 371-394, 2008.

SKJETNE, R. **The Maneuvering Problem.** Ph.D. thesis, Norwegian University of Science and Technology. Trondheim, Norway, 2005.

SKJETNE, R.; SMOGELI, Ø. N.; FOSSEN, T. I. **A nonlinear ship manoeuvring model: identification and adaptive control with experiments for a model ship.** Modeling, Identification and Control, 25, n. 1, pp. 3-27, 2004.

SNAME. **Nomenclature for treating the motion of a submerged body through a fluid.** Technical Report Bulletin 1-5. The Society of Naval Architects and Ocean Engineers, New York, USA, 1950.

SØRENSEN, A. **Marine cybernetics: modelling and control.** Lecture notes. Norwegian University of Science and Technology. Trondheim, Norway, 2005.

SOUZA JR., J. R.; MORISHITA, H. M.; RAGAZZO, C. G. **Hydrodynamic interaction of two ships in tandem under current**. Proc. of the 16th International Offshore and Polar Engineering Conference (ISOPE 2006). San Francisco, USA, 2006.

SOUZA, C. E. S.; MORISHITA, H. M. **Dynamic modeling of underway ship-to-ship operations**. Proc. of the 30th International Conference on Ocean, Offshore and Arctic Engineering (OMAEO2011). Rotterdam, The Netherlands, 2011.

SOUZA, C. E. S.; OSHIRO, A. T.; MORISHITA, H. M. **Cooperative control applied to coordinated operations of ships with dynamic positioning system**. 23^o Congresso Nacional de Transporte Aquaviário, Construção Naval e Offshore (SOBENA 2010). Rio de Janeiro, Brazil, 2010.

TAGHIPUR, R.; PEREZ, T.; MOAN, T. **Hybrid frequency-time domain models for dynamic response analysis of marine structures**. Ocean Engineering, 35, pp. 685-705, 2008.

TANNURI, E. A. **Desenvolvimento de metodologia de projeto de sistema de posicionamento dinâmico aplicado a operações em alto-mar**. Ph.D. thesis (in Portuguese). University of São Paulo, São Paulo, Brazil, 2002.

TANNURI, E. A. et al. **Wind shielding effects on DP system of a shuttle tanker**. Proc. of the 29th International Conference on Ocean, Offshore and Arctic Engineering (OMAEO2010). Shanghai, China, 2010.

VAN BERLEKOM, W. B.; GODDARD, T. A. **Maneuvering of large tankers**. Trans. of the Society of Naval Architects and Marine Engineers, 80, pp. 264-298, 1972.

VANTORRE, M.; VERZHBITSKAYA, E.; LAFORCE, E. **Model test Based Formulations of ship-ship interaction forces**. Ship Technology Research, pp. 124-141, 2002.

VARYANI, K. S.; THAVALINGAM, A.; KRISHNANKUTTY, P. **New generic mathematical model to predict hydrodynamic interaction effects for overtaking maneuvers in simulators**. Journal of Marine Science and Technology, 9, pp. 24-31, 2004.

WAMIT. **2005 Annual WAMIT consortium meeting**. Massachusetts, USA, 2005.

WAMIT. **WAMIT user manual**. Chestnut Hill, USA: WAMIT, Inc., 2006.

WANG, Q. X. **An analytical solution for two slender bodies of revolution translating in very close proximity.** Journal of Fluid Mechanics, 582, pp. 223-251, 2007.

XIANG, X.; FALTINSEN, O. M. **Hydrodynamic interaction loads between two ships during lightering operation in calm water.** Proc. of the 2nd International Conference on Ship Manoeuvring in Shallow and Confined Water: Ship to Ship Interaction. Trondheim, Norway, 2011.

ZAKARTCHOUK JR, A. **Projeto de um observador passivo não-linear e de um controlador backstepping para navios de superfície.** M.Sc. dissertation, University of São Paulo, São Paulo, Brazil, 2010.

APPENDIX A – The Lyapunov Direct Method

A.1 DEFINITION OF STABILITY ACCORDING TO LYAPUNOV

Many definitions for stability are available in the literature. The so-called *Lyapunov stability* is the most adequate for the present case. Let an autonomous nonlinear system be defined by:

$$\dot{\mathbf{x}} = \mathbf{f}(\mathbf{x}), \quad \mathbf{x}(0) = \mathbf{x}_0 \quad (\text{A.1})$$

with $\mathbf{x} \in \mathbb{R}^n$. If \mathbf{x}_e is an equilibrium point of the above system, (i.e., $\mathbf{f}(\mathbf{x}_e) = \mathbf{0}$), a solution $\mathbf{x}(t)$ for (A.1) is said to be *Lyapunov stable* if, for a given $\epsilon > 0$, there exists $\delta > 0$ such that:

$$\|\mathbf{x}(0)\| < \delta \Rightarrow \|\mathbf{x}(t)\| < \epsilon, \quad \forall t \geq 0 \quad (\text{A.2})$$

Additionally, the system is said to be *attractive* if, for a given $r > 0$ and $\epsilon > 0$, there exists T satisfying:

$$\|\mathbf{x}(0)\| \leq r \Rightarrow \|\mathbf{x}(t)\| \leq \epsilon, \quad \forall t \geq T \quad (\text{A.3})$$

Implying that the system is convergent, i.e., $\lim_{t \rightarrow \infty} \|\mathbf{x}(t)\| = \mathbf{0}$. If an equilibrium point \mathbf{x}_e is both stable and attractive, it is said to be *asymptotically stable* (AS). If, in addition, the stability holds for all $\mathbf{x}(0)$, \mathbf{x}_e is said to be *globally asymptotically stable* (GAS). Finally, if there exists α, λ and $r > 0$ such that:

$$\|\mathbf{x}(0)\| < r \Rightarrow \|\mathbf{x}(t)\| < \alpha \exp(-\lambda t) \|\mathbf{x}(0)\|, \quad \forall t \geq 0 \quad (\text{A.4})$$

the system is said to be *globally exponentially stable* (GES).

A.2 LYAPUNOV'S DIRECT METHOD

Theorem A.1

Let \mathbf{x}_e be an equilibrium point of the autonomous system (A.1). Also, consider $\mathbf{f}(\mathbf{x})$ to be locally Lipschitz in \mathbf{x} , i.e., that for $L > 0$:

$$\|\mathbf{f}(\mathbf{x}) - \mathbf{f}(\mathbf{y})\| \leq L\|\mathbf{x} - \mathbf{y}\|, \quad \forall \mathbf{x}, \mathbf{y} \in \mathbb{R}^n \quad (\text{A.5})$$

If there exists a continuously differentiable function $V: \mathbb{R}^n \rightarrow \mathbb{R}_+$ satisfying:

- $V(\mathbf{x}) > 0$, for $\mathbf{x} \neq \mathbf{0}$ and $V(\mathbf{0}) = 0$
- $\dot{V}(\mathbf{x}) \leq -W(\mathbf{x}) \leq 0$
- $\|\mathbf{x}\| \rightarrow \infty \Rightarrow V(\mathbf{x}) \rightarrow \infty$

Then, if W is positive semi-definite ($W(\mathbf{x}) \geq 0$, $\mathbf{x} \neq \mathbf{0}$), the equilibrium point \mathbf{x}_e is stable. If W is positive definite ($W(\mathbf{x}) > 0$, $\mathbf{x} \neq \mathbf{0}$), then \mathbf{x}_e is GAS (KHALIL, 2002).